PolyPublie
Polytechnique Montréal

POLYTECHNIQUE MONTRÉAL
UNIVERSITÉ D'INGÉNIERIE

Titre: Title:	Elastic Reconfiguration of Bending and Twisting Rods in Air Flow
Auteur: Author:	Masoud Hassani
Date:	2016
Type:	Mémoire ou thèse / Dissertation or Thesis
Référence: Citation:	Hassani, M. (2016). Elastic Reconfiguration of Bending and Twisting Rods in Air Flow [Thèse de doctorat, École Polytechnique de Montréal]. PolyPublie. https://publications.polymtl.ca/2467/

Document en libre accès dans PolyPublie
Open Access document in PolyPublie

URL de PolyPublie: PolyPublie URL:	https://publications.polymtl.ca/2467/
Directeurs de recherche: Advisors:	Frederick Gosselin, & Njuki W. Mureithi
Programme: Program:	Génie mécanique

Ce fichier a été téléchargé à partir de PolyPublie, le dépôt institutionnel de Polytechnique Montréal
This file has been downloaded from PolyPublie, the institutional repository of Polytechnique Montréal

https://publications.polymtl.ca

UNIVERSITÉ DE MONTRÉAL

ELASTIC RECONFIGURATION OF BENDING AND TWISTING RODS IN AIR FLOW

MASOUD HASSANI
DÉPARTEMENT DE GÉNIE MÉCANIQUE
ÉCOLE POLYTECHNIQUE DE MONTRÉAL

THÈSE PRÉSENTÉE EN VUE DE L'OBTENTION
DU DIPLÔME DE PHILOSOPHIÆ DOCTOR
(GÉNIE MÉCANIQUE)
DÉCEMBRE 2016

© Masoud Hassani, 2016.

UNIVERSITÉ DE MONTRÉAL

ÉCOLE POLYTECHNIQUE DE MONTRÉAL

Cette thèse intitulée :

ELASTIC RECONFIGURATION OF BENDING AND TWISTING RODS IN AIR FLOW

présentée par : HASSANI Masoud
en vue de l'obtention du diplôme de : Philosophiæ Doctor
a été dûment acceptée par le jury d'examen constitué de :

Mme ROSS Annie, Ph. D., présidente
M. GOSSELIN Frédérick, Doctorat, membre et directeur de recherche
M. MUREITHI Njuki William, Ph. D., membre et codirecteur de recherche
M. ÉTIENNE Stéphane, Doctorat, membre
M. PASINI Damiano, Ph. D., membre externe

DEDICATION

To my loved ones,
To my parents who always support me,
To my wife, I could not have done it without her.

ACKNOWLEDGMENT

I am truly thankful of my supervisor Frédérick Gosselin and my co-supervisor Njuki Mureithi, for their incredible support, patience and immense knowledge. During these years, I learned a lot from them and I will appreciate it forever. I deeply believe that they had and they still have a big impact on my life. I could improve many aspects of my thinking and judgment, whether scientific or non-scientific, by learning from them.

I am grateful to bachelor interns, Michael Plante, Diego Altamirano, Pablo Maceira-Elvira, Anthony Salze and Simon Molgat Laurin, whose work helped me during my research. I am also thankful to Benedict Besner, Nour Aimene, Isabelle Nowlan and Martin Cardonne for their technical support. I thank all the professors and students of the Laboratory for Multiscale Mechanics for providing such a scientific, dynamic and friendly atmosphere.

I owe my lovely family for every single accomplishment in my life especially my parents Dr. Mohammad Hassani and Akram Ozaee who have dedicated their lives for their children. They are the most important reason behind my success because of their unconditional support and love. They mean the world to me.

I have had an amazing support from my love, Elham Kheradmand Nezhad. During my doctoral studies, we had and we continue to have a great and adventurous life together. This always gives me a great motivation and energy to work harder. I am deeply grateful for her support and kindness.

RÉSUMÉ

Les plantes sont généralement flexibles et se déforment significativement lorsqu'elles sont soumises à un écoulement aérodynamique. Ce changement de forme, qui généralement réduit la traînée, est appelée reconfiguration. Plusieurs études dans la littérature ont apporté une compréhension fondamentale de la reconfiguration des plantes en la modélisant comme une poutre en flexion. Bien que cette approche permette de capturer l'essence de la flèche bidimensionnelle des plantes, leur flèche tridimensionnelle est ignorée. En effet, en raison de leur structure fibreuse, les plantes se tordent significativement sous un écoulement, montrant une reconfiguration tridimensionnelle. De plus, de nombreuses plantes ont une morphologie chirale, ce qui induit une flèche très complexe. Le présent travail de recherche vise à étudier l'effet de la torsion et de la chiralité dans la reconfiguration des plantes en combinant expérimentation et modélisation pour comprendre comment une tige élastique se plie et se tord avec grande amplitude sous le vent. Pour l'étude expérimentale, des tiges composites sont fabriquées en mousse de polyuréthane et renforcées à l'aide de fibres de nylon qui apportent un couplage de torsion-flexion à la structure finale. Pour reproduire une structure chirale, les fibres suivent un patron hélicoïdal le long dans la tige. Afin d'enrichir l'étude expérimentale, des rubans chiraux en plastique ABS sont aussi conçues. Tous les spécimens sont testés dans une soufflerie sous différentes conditions d'écoulement. Pour l'étude numérique, la reconfiguration tridimensionnelle des tiges et des rubans sera simulée utilisant la théorie de tiges de Kirchhoff couplée avec une formulation semi-empirique pour introduire les forces aérodynamiques. Les résultats de ces études montrent que ces structures, fortement anisotropes, se tordent pour ensuite fléchir selon la direction de moindre rigidité en flexion. De plus, la reconfiguration tridimensionnelle d'une tige peut être caractérisée par une flexion bidimensionnelle en choisissant le bon ensemble de paramètres adimensionnelles. Il est aussi constaté que les rubans chiraux font face à un compromis, en fonction la configuration géométrique, entre la résistance au flambage plus élevé mais aussi le moment de flexion plus élevé à la base. Finalement, la chiralité rend la flèche de ces structures moins dépendante de la direction de chargement.

ABSTRACT

Plants are generally flexible and deform significantly when subjected to flow. This deformation which generally leads to a drag reduction is termed reconfiguration. Fundamental understanding of this phenomenon has been sought by modeling them as bending beams. Although bending beams capture the essence of the two-dimensional deformation of plants, their three-dimensional deformation is ignored. Because of their fibrous structure, plants twist significantly under fluid loading showing a three-dimensional reconfiguration. Moreover, many plants are found with a chiral morphology which undergo a complex deformation under loading. The present research aims to model the reconfiguration of plants with an elastic rod undergoing a large deformation, to study the effect of torsion and chirality in reconfiguration. In the experimental investigation, composite rods are made of polyurethane foam and reinforced using nylon fibers which have a bending-torsion coupling. To simulate a chiral structure, the reinforcing fibers are twisted along the length of the rod. Moreover, chiral ribbons are made using ABS plastic. All the specimens are tested in a wind tunnel for a variety of flow and structural properties. The three-dimensional reconfiguration of rods and ribbons is also modeled numerically using the Kirchhoff theory of rods coupled with a semi-empirical drag formulation and the blade element theory. It is shown that a rod with structural anisotropy twists in such a way to bend in its less rigid direction. Moreover, the three dimensional reconfiguration of a rod can be characterized as a two dimensional bending by choosing the right set of dimensionless parameters. It is found that chiral ribbons face a trade-off between higher self-buckling strength but also higher root bending moment. Moreover, chirality renders the deformation of rods and ribbons less dependent to the loading direction.

TABLE OF CONTENTS

DEDICATION iii

ACKNOWLEDGMENT iv

RÉSUMÉ v

ABSTRACT vi

TABLE OF CONTENTS vii

LIST OF TABLES ix

LIST OF FIGURES x

LIST OF APPENDICES xv

CHAPTER 1 INTRODUCTION 1
1.1 Motivation 1

CHAPTER 2 LITERATURE REVIEW 6
2.1 Reconfiguration 6
2.2 Drag Scaling of Natural Structures 7
2.3 Fundamental Investigations on Reconfiguration 9
2.3.1 Dimensionless Parameters in Reconfiguration 9
2.3.2 Two-Dimensional Reconfiguration 11
2.3.3 Three-Dimensional Reconfiguration 13
2.3.4 Similarity in Reconfiguration 14
2.4 Chirality in Natural Structures 16
2.5 Theoretical Framework for Modeling Plants 19
2.6 Biomimetics : Aeroelastic Tailoring 23
2.7 Problem Identification 24

CHAPTER 3 ARTICLE 1 : LARGE COUPLED BENDING AND TORSIONAL DEFORMATION OF AN ELASTIC ROD SUBJECTED TO FLUID FLOW 26
3.1 Introduction 26
3.2 Methodology 29

3.2.1 Experimental Procedure and Materials 29
3.2.2 Theoretical Model 33
3.3 Results and Discussion 38
3.3.1 Dimensionless Representation 43
3.3.2 Equivalent Bending Rigidity 46
3.4 Conclusion 51

CHAPTER 4 ARTICLE 2 : BENDING AND TORSIONAL RECONFIGURATION OF CHIRAL RODS UNDER WIND AND GRAVITY 53
4.1 Introduction 53
4.2 Methodology 54
4.2.1 Experimental Procedure and Materials 54
4.2.2 Theoretical Model 56
4.3 Results and Discussion 61
4.3.1 Mathematical Model Verification 61
4.3.2 Buckling 62
4.3.3 Drag and Lift Coefficients 62
4.3.4 Drag of Flexible Specimens 63
4.3.5 Curvature and Bending Moment 65
4.4 Concluding Remarks 69

CHAPTER 5 DETAILS OF EXPERIMENTS 72
5.1 Specimen Fabrication 72
5.2 Bending and Torsional Rigidity 73
5.3 Drag of Rigid Specimens 75
5.4 Details of Wind Tunnel Tests 75
5.5 Static Bending Test 79
5.6 Details of Measurements on Cattail Leaves 79

CHAPTER 6 GENERAL DISCUSSION 81

CHAPTER 7 CONCLUSION 83
7.1 Contribution 83
7.2 Limitations and Future Work 85

REFERENCES 87

APPENDICES 95

LIST OF TABLES

Table 2.1	The average of twist-to-bend ratio for some natural structures	15
Table 2.2	The Vogel exponent for some flexible structures, aquatic and terrestrial organisms	16
Table 2.3	A comparison between advantages and disadvantages of three different representations of the material frame	21
Table 3.1	The average of twist-to-bend ratio for some natural and engineering structures	28
Table 3.2	Physical properties of tested specimen	31
Table 3.3	The Vogel exponent for a range of angle of incidence calculated from the experimental data points and the mathematical simulation of R3	45
Table 4.1	Physical properties of tested specimens	56
Table 4.2	Physical properties of study cases	68

LIST OF FIGURES

Figure 1.1 The effect of wind on plants. (a) Lodging of crops caused by severe storm (Thomison, 2011). (b) Permanent change in the shape of a tree due to the wind and gravity as known as "flag tree" (Geoff, 2009) . . . 3

Figure 1.2 Demonstration of the effect of mechanical perturbation on the trunk of loblolly pine. Transverse section of trunk (a) under controlled conditions and (b) under mechanical stress (Telewski and Jaffe, 1981) 4

Figure 2.1 Main mechanisms of drag reduction and reconfiguration. a) An undeformed tulip tree leaf and b) the leaf reconfiguring in wind by reduction of the frontal area and the drag coefficient. b) Measurements on the crown of black cottonwood which show the reduction of the frontal area and the drag coefficient due to reconfiguration (Vollsinger *et al.*, 2005). The image of the leaf is adapted from Vogel (1989). 8

Figure 2.2 Comparison between the drag scaling of a flexible plant (giant reed) with its equivalent rigid body. Data is obtained from Speck (2003). . . 8

Figure 2.3 A schematic of giant kelp showing its stipe, clumped blades and the holdfast. The figure is reproduced from Johnson and Koehl (1994). . . 9

Figure 2.4 Different modes of reconfiguration of the London plane tree leaf in different wind speeds to reduce the drag force and to make it more stable. The unit of velocity is ms^{-1}. Images are obtained from Shao *et al.* (2012). 10

Figure 2.5 The variation of the reconfiguration number with the Cauchy number for different natural species (de Langre, 2008) compared with a fiber bending in flow (Alben *et al.*, 2002). 12

Figure 2.6 Comparison between the drag coefficient of a Daffodil flower facing downwind and upwind. Data has been extracted from Etnier and Vogel (2000). 14

Figure 2.7 Similarity of simple mechanical structures with natural ones by comparing a) a palm tree with b) a poroelastic ball, and c) a tulip tree leaf with d) an elastic circular sheet which rolls up. The image of the palm tree is taken by Verdier (2003). The image of the poroelastic ball is extracted from Gosselin and de Langre (2011) and the others are reproduced from Schouveiler and Boudaoud (2006); Vogel (1989). . . . 16

Figure 2.8 Similar trend of experimental results of different specimens subjected to flow and characterized by the reconfiguration number and the scaled Cauchy number for cut disks △ and a bending rectangular plate ○ (Gosselin *et al.*, 2010), poroelastic ball × (Gosselin and de Langre, 2011), circular flexible plate which rolls up in flow ◇ (Schouveiler and Boudaoud, 2006) and bending fibers □ (Alben *et al.*, 2004). The line represents the mathematical model for the two-dimensional reconfiguration of a plate in flow (Gosselin *et al.*, 2010). Images are extracted from the mentioned references. 17

Figure 2.9 a) a carbon nanotube rope with a chiral morphology (Zhao *et al.*, 2014) and b) a chiral cattail leaf 18

Figure 2.10 A rod connected to a fixed coordinate system with moving material frames connected to its centerline. 20

Figure 3.1 Schematics of a banana leaf (a) U-shape cross section of its petiole with a large twist-to-bend ratio; (b) upright banana leaf; and (c) leaf twisting to bend downwind. Inspired by Ennos *et al.* (2000). 29

Figure 3.2 Schematic of the test setup installed on top of the wind tunnel. The setup consists of a servo (1), gearbox (2), force balance (3), aluminum frame (4), wooden panel (5) and a rod specimen (6). 30

Figure 3.3 Photograph of a flexible rod's section made of polyurethane foam and reinforced with nylon fibers which have an angle of incidence ψ with the flow. The angle of incidence at the clamped end is defined by ψ_0. . 32

Figure 3.4 Schematic of a rod connected to a fixed coordinate system with moving material frames attached to its centerline. 34

Figure 3.5 Photographs of deformed shapes of the specimen R3. Thin lines represent the deformation of an equivalent rod predicted by the mathematical model. The velocity unit is ms^{-1}. 40

Figure 3.6 Mathematical evaluation of the in-plane and out-of-plane deformation of specimen R3 for three angles of incidence by showing a) the variation of the tip's X-component, b) the tip's Y-component and c) the tip's Z-component with flow velocity. Some experimental data points are provided for reference as markers. Error bars represent the standard deviation of the time fluctuations of the tip position. 42

Figure 3.7 Time-averaged drag of the specimen R3 for a range of ψ_0 from 0° to 90°. Drag loading on an equivalent rigid rod is provided as a line for reference. Error bars represent the standard deviation of the time fluctuations for series ψ_0 = 45°. Time fluctuations are similar for other series. 43

Figure 3.8 Twisting moment at the root of the specimen R3 varying by the flow velocity and angle of incidence. The mathematical evaluation of the root's twisting moment is provided as lines for reference. 44

Figure 3.9 Experimental drag scaling of the specimen R3 represented by the Cauchy number and the reconfiguration number. The equivalent mathematical model for $\psi_0 = 0°$, 45° and 90° is provided as lines. 45

Figure 3.10 The reconfiguration number of the three specimens (table 3.2) for a range of ψ between 0° and 90° plotted versus a) the Cauchy number and b) the equivalent Cauchy number to find a generic representation of the drag scaling. The Mathematical models for $\psi_0 = 0°$ and $\psi_0 = 90°$ are presented as lines. 48

Figure 3.11 Mathematical demonstration of torsion of R3 along its length by plotting the variation of $\bar{\tau}$ with $\bar{s}$, C_Y^* and ψ_0. 50

Figure 3.12 Experimental evaluation of the torsion length of specimen R3 varying with the equivalent Cauchy number. The mathematical model is provided as lines for comparison. 51

Figure 4.1 a) Schematics of chiral rods with an intrinsic twist angle varying from 0° to 360° as well as a real rod specimen. b) Schematics of chiral ribbons with an intrinsic twist angle varying from 0° to 360° a well as a real twisted ribbon. c) Section of a chiral rod and d) section of a chiral ribbon both with an incidence angle of ψ. e) Schematic of a chiral ribbon deformed in the flow with a moving material frame attached to its centerline. 56

Figure 4.2 a) Static bending test for chiral circular rods. The rods are fixed horizontally from one end and their maximum vertical deflection is plotted vs. the angle of incidence at the fixed end. Markers represent the experimental results. b) The effect of chirality and the bending rigidity ratio of rods on their critical buckling length. 63

Figure 4.3 Rose plot of drag as a function of the intrinsic twist angle, τ_0 and the incidence angle, ψ for a) chiral circular rods with U = 13 ms^{-1} and b) chiral ribbons with U = 15 ms^{-1}. c) Maximum and minimum relative drag of chiral circular rods at U = 13 ms^{-1} and d) chiral ribbons at U = 15 ms^{-1} among a range of incidence angles. Markers represent the experimental data and lines show the mathematical prediction. The maximum and minimum drag of equivalent rigid rods and ribbons are also provided for reference. 66

Figure 4.4 Theoretical evaluation of the deformed shape of weightless ribbons under a terminal moment with a)τ_0 = 0° and b)τ_0 = 360°. Deformed shape of upright ribbons under the wind loading with c)τ_0 = 0° and d)τ_0 = 360°. Contour of the total curvature κ_t for e) weightless chiral ribbons under a terminal moment and f) upright ribbons in the flow. The terminal moment is $\bar{M}_Y$ = 1.2, the Cauchy number is C_Y = 30 and ψ_0 is null for all cases. Small arrows show the curvature nodes on the deformed ribbons. 67

Figure 4.5 Maximum dimensionless bending moment at root of five study cases at C_Y = 30. Plots are predicted using the mathematical model. The shaded area represent the range of the most probable intrinsic twist angle of the cattail specimens collected for this study. The small histogram plot shows the distribution of the collected specimens in terms of the intrinsic twist angle. 70

Figure 5.1 Photograph of the mold used to fabricate circular rods. 72

Figure 5.2 Schematic of the test setup used to measure the torsional rigidity of a rod. In this test setup, the rod (1) is attached to the center of a rectangular aluminum plate (2) which can rotate around a pin (3) freely. The pin limits the movement of the aluminum plate to rotation around its center. 74

Figure 5.3 Wind tunnel measurements of the lift and drag coefficients of a metallic ribbon equivalent to flexible ABS ribbons averaged over Re = 10000 and Re = 20000. Markers represent experimental values and lines are fitted trigonometric functions (Eq. (4.36) and Eq. (4.37)). 76

Figure 5.4 Variation of a) the lift and b) the drag coefficients for a rigid chiral ribbon with $\tau_0 = 90°$ as a function of the incidence angle ψ_0. The length and width of the ribbon are 400 mm and 25.4 mm respectively. Lines represent the mathematical model for two different thicknesses. Symbols represent the experimental results for two different Reynolds numbers. 77

Figure 5.5 a) Photograph of the mast used for testing circular rods. It consists of a circular adapter for connection to the force transducer (1a), an acrylic rod (2a), a sleeve (3a) and a threaded hole to hold the M4 screw of circular rods (4a). b) Photograph of the mast used for testing ABS ribbons. It consists of a circular adapter for connection to the force transducer (1b), an acrylic rod (2b), a slot (3b) and a threaded hole to keep ribbons in place (4b). Small ellipses at the end of masts represent the reference point schematically. 78

Figure 5.6 Test setup for the static bending test showing a cantilever rod (2) deforming under its own weight. The rod is attached to a disk (1) which can be rotated around its center to impose different incidence angles. The definition of the incidence angle is shown at the lower left of the figure. 79

Figure 5.7 Photograph of cattail leaves at the the Voyageur Provincial Park in Ontario, Canada. 80

LIST OF APPENDICES

Appendix A DIRECTION COSINES 95

CHAPTER 1 INTRODUCTION

Mechanical engineering structures are typically rigid and do not deform significantly under loading. In contrast, plants are flexible and deform with large amplitude when subjected to fluid flow and gravity. The deformation of plants under fluid loading can be very large leading to structural failure. This phenomenon is generally known as "wind damage" which has adverse effects on human life. Moreover, mechanical stresses exerted by fluid loading can permanently alter the structure of plants and change their geometry and growth rate. These phenomena have motivated numerous studied on the deformation of plants in nature. Many types of plants have been tested to study their interaction with fluid flow. Furthermore, fundamental understanding of the deformation of plants in flow has been undertaken by modeling them as simple structures such as bending beams and plates. This has led to better understanding the underlying mechanisms of deformation and the drag reduction of plants in nature.

While simple bending structures cover the essence of the deformation of plants, their twisting mechanism is ignored. Moreover, many plants have geometrical complexities which cannot be studied using a simple bending beam. In this research, we simulate the arbitrary large deformation of plants using an elastic rod model. A rod is a slender beam capable of having a torsional deformation in addition to the bending deformation. Our goal is to understand the deformation mechanisms of plants in the presence of torsion. We evaluate the effect of torsion in the drag scaling of plants as flexible structures. To do this, a mathematical model for an arbitrary deformation of rods is developed and wind tunnel tests are performed. In the next section, the motivation behind this study is discussed. This is followed by an exploration of the existing knowledge in the field. The main questions of the present research are then precisely defined.

1.1 Motivation

The destructive effects of wind and water flow on plants including windthrow, uprooting and lodging (see Fig. 1.1a) are a big concern around the world since they have many adverse effects on human life. Wind damage to trees causes severe environmental changes in forests and affects the regeneration of trees (Ulanova, 2000). In addition, human injuries, road blockage, power outage and the reduction of construction materials are examples of problems linked with windthrow. Lodging can cause an 80 percent reduction in the crop production in addition to making harvesting more difficult and decreasing the quality of the products (Berry *et al.*,

2004).

In recent decades, many approaches have been developed to predict the response of individual plants or plants in a canopy to flow. In order to evaluate the drag force and the uprooting strength, it is necessary to consider several parameters such as the plant's height, diameter and stiffness as well as soil strength. There exist software packages such as HWIND (Peltola *et al.*, 1999) and ForestGALES (Gardiner *et al.*, 2000) which can calculate the critical wind speed or snow loading needed to damage or uproot some types of trees like pine and spruce. These packages take the geometry of trees in a canopy, spacing between them, wind speed and material properties to calculate the risk of wind damage and the critical wind speed. They use a simple mathematical model considering an average wind speed and drag coefficient, to evaluate the root moment without considering the deformation of trees. Researchers have also developed mathematical models to predict the risk of lodging of cereals using the aforementioned parameters (Baker *et al.*, 1998; Berry *et al.*, 2003, 2006). In addition, theories and mathematical models have been established to study the strategy of plants to withstand large deformations with an optimized structural mass (Pasini and Mirjalili, 2006; Brulé *et al.*, 2016) and increase their buckling stability (Speck *et al.*, 1990; Spatz *et al.*, 1990; Burgess and Pasini, 2004).

The prediction and control of wind damage has made it possible to decrease the occurrence of tree failure and crop lodging in recent decades by applying proper field management and genetic or chemical manipulation. For instance, between the 1960s and 1970s, many efforts were made to alter crops to generate smaller varieties known as dwarf or semi-dwarf which were more resistant to lodging. As a result, cereal yields have been increased by 0.5 to 1 ton per hectare each decade in many countries in Asia, Europe and North America. These methods are now used around the world. For example, in France, the United Kingdom and Germany which are among the top grains producers in the world, these manipulations are applied to more than 70 percent of the wheat fields (Berry *et al.*, 2004).

Wind damage is intrinsically a fluid-structure interaction problem. The main fluid force acting on plants is the drag force. In the aforementioned failure risk evaluation models, a constant drag coefficient is considered to calculate the wind loading on plants. In general, these models use an empirical value for the drag coefficient which is obtained experimentally. They mainly focus on limited types of trees and crops and cannot be generalized to all types of plants. In general, plants have long slender structures e.g. trunks, petioles and stems. In engineering, beams are long and slender structures therefore we can model plants as elastic beams deforming in flow. This approach is advantageous over testing each species of plants separately because it is simple and reproducible. Using a beam model, we can fundamentally investigate

(a) (b)

Figure 1.1 The effect of wind on plants. (a) Lodging of crops caused by severe storm (Thomison, 2011). (b) Permanent change in the shape of a tree due to the wind and gravity as known as "flag tree" (Geoff, 2009)

the deformation of plants under fluid loading.

Wind can cause permanent changes in the plant shape."Flag tree" is a graphic example as shown in Fig. 1.1b. Wind also affects plant growth through what is known as "Thigmomorphogenesis" (Niklas, 1998). Environmental conditions such as fluid loading, sunlight direction or external mechanical stresses such as gravity, lead to the production of chemicals in plants which alter their growth rate and stiffness. For example, sugar maple trees from open and windy sites have smaller and more flexible leaves than those from wind protected sites (Niklas, 1996). The change in the growth rate under the mechanical perturbation is illustrated in Fig. 1.2 which shows that radial growth rate increases in the direction of the applied perturbation. This means that plants adapt themselves to external loading and their growth rate increases where the load is applied (Mattheck and Bethge, 1998; Mattheck *et al.*, 2003; Mattheck, 2006). As another example, Telewski and Jaffe (1986a,b) report an increase in radial growth rate and a decrease in the flexibility of loblolly pine and fraser fir induced by mechanical perturbation. This is also observed in aquatic plants. For instance, the rigidity and consequently the canopy height of eelgrass is strongly affected by the magnitude of water flow (Abdelrhman, 2007). Moreover, experiments on giant kelp show that species which live in fast moving water flows have narrower blades with lower drag, preventing structural failure (Koehl and Alberte, 1988; Johnson and Koehl, 1994).

The interaction between plants and fluid flow is inspiring in engineering. Plants are able to passively extend their stability envelope and decrease the mechanical loading on their

structure by being flexible. This can be used to address several problems in mechanical and aerospace engineering where the interaction between fluid and structure is important. For instance, to improve the mission adaptability and stability of micro aerial vehicles (MAVs), extremely flexible rotor blades are considered which undergo a large amplitude of deformation (Sicard and Sirohi, 2012, 2014, 2016). A wind turbine can be designed to cone passively in high winds to cope with the excessive wind loading. This means that the turbine blades can bend downwind around a hinge to create a cone-shaped swept area. This concept was originally developed to deal with the bending moment caused by the weight of heavy steel blades. However, modern blades are made of light composites and the concept of coning can be used to increase their operational wind speed range. Wind turbines are commonly designed for wind speeds up to 15 ms^{-1} (Jamieson, 2011). By implementing the passive coning mechanism, fluid loading on the blades can be reduced in high winds to avoid structural failure (Curran and Platts, 2006).

Passive adaptive wind turbine blades based on the concept of aeroelastic tailoring are also an example of adaptation to the flow. These blades are used to bypass extreme loading (Lago *et al.*, 2013). Aeroelastic tailoring can also be used to build adaptive rear wings for Formula 1 cars. This type of rear wing is able to create high downward forces at low speeds and low drag force at high speeds (Thuwis *et al.*, 2009). Moreover, it can be applied to flexible wings to create high lift-to-drag ratio and increased stability (Stanford *et al.*, 2008; Ifju *et al.*, 2002) and flexible marine propellers for improved performance (Liu and Young, 2009).

The aforementioned applications can be modeled as flexible structures interacting with the flow. Understanding the underlying mechanisms of deformation of these structures by means of mathematical modeling can therefore reduce the production cost and increase the reliability

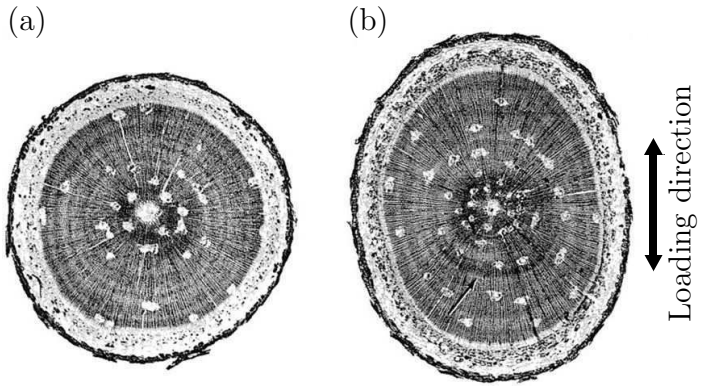

Figure 1.2 Demonstration of the effect of mechanical perturbation on the trunk of loblolly pine. Transverse section of trunk (a) under controlled conditions and (b) under mechanical stress (Telewski and Jaffe, 1981)

of design (Lago *et al.*, 2013). The mathematical modeling can also be applied to engineering applications dealing with slender structures bending and twisting under a loading other than a fluid force. An example of this case is a soft actuator made of a shape memory alloy which twists and bends by applying an electric current (Shim *et al.*, 2015). Many of these engineering components can be modeled as flexible beams and rods deforming under external forces and torques. Therefore, in this research we aim to develop a generic mathematical framework capable of modeling the complex deformation of plants and slender structures under external loading.

CHAPTER 2 LITERATURE REVIEW

In this section we review the existing knowledge on the experimental and theoretical modeling of plants and slender structures interacting with the flow.

2.1 Reconfiguration

In contrast to mechanical structures, plants are flexible and deform significantly under fluid loading. This deformation which usually leads to a drag reduction is termed "reconfiguration" in the literature (Vogel, 1984, 1989). The drag force D of a rigid bluff body is proportional to U^2 where U is the flow velocity. However, plants are subjected to a drag which is not proportional to the square of the flow velocity. As suggested by Vogel (1984), the reconfiguration of different natural species may be compared by studying their divergence from the drag scaling of rigid bluff bodies. To do this, he introduces the Vogel exponent ϑ as the slope of the logarithmic plot of D/U^2 or "speed specific drag" versus the flow velocity. The drag force on flexible structures is proportional to $U^{2+\vartheta}$:

$$D \propto U^{2+\vartheta} \ . \tag{2.1}$$

The Vogel exponent ϑ quantifies the effect of reconfiguration in the drag velocity relation. For rigid bluff bodies, ϑ is null since they do not reconfigure. Conversely, for flexible structures, ϑ is generally negative. The more negative ϑ is the more the drag reduces due to the reconfiguration.

There are two main mechanisms of reconfiguration although the deformation of natural flexible structures in the flow is complex. In general, the drag force is proportional to the drag coefficient and the frontal area therefore decreasing these two parameters, reduces the drag force. For instance, Fig. 2.1a shows an undeformed tulip tree leaf and Fig. 2.1b shows the leaf reconfiguring in wind by rolling around itself. This reduces the wind loading by decreasing the frontal area and by streamlining which is equivalent to the drag coefficient reduction. Flexible plants use these two mechanisms to reduce the pressure drag, but the effect of each method on the reduced drag is different depending on the plant. For example, Fig. 2.1c shows measurements of the drag coefficient and the frontal area for the unpruned crown of black cottonwood. It illustrates how the drag coefficient and the frontal area decrease with increasing wind speed or increasing magnitude of deformation. In this plot, the drag coefficient is calculated using the still-air frontal area, therefore it only represents the effect of streamlining

(Vollsinger *et al.*, 2005).

2.2 Drag Scaling of Natural Structures

Researchers in the fields of biology, botany and forestry, have worked on the deformation and the drag scaling of plants, terrestrial and aquatic vegetation. They have studied passive methods which plants employ to cope with the wind and water loading. Observing flexible structures in nature, they came up with the following question : what is the effect of fluid flow on plants ? To answer the question, many types of plants, crops, algae, leaves and trees were tested individually or in communities in wind tunnels, water canals or their natural habitats to obtain the drag scaling. The results show that the drag scaling of natural flexible structures is different from the drag scaling of rigid bodies (Vogel, 1984). For instance, Fig. 2.2 shows the drag scaling of a giant reed, a flexible slender and upright plant, measured by Speck (2003). Comparison is made with the drag of an equivalent rigid bluff body which follows the curve of U^2. In the figure, the drag force on the flexible giant reed follows the drag force of the rigid body at low wind speeds but starts to diverge from this scaling on increasing the flow velocity.

Many types of aquatic plants and algae have flexible structures and reconfigure in water flow. Giant kelp or mermaid's bladder as an example, is a kind of kelp which grows in the cold waters of the American Pacific coast. It has a long stipe which is attached to a float and blades. Also, a holdfast keeps this plant attached to the substrate as shown in Fig. 2.3. Observations show that the giant kelp bends in water flow and also clumps its blades. This reduces its frontal area and makes it more streamlined which decreases the drag force on its structure (Koehl and Alberte, 1988; Johnson and Koehl, 1994). Because of the gas filled float in the plant, a buoyancy force acts in addition to inertial and hydrodynamic forces (Koehl, 1977).

In addition to aquatic plants, researchers have studied many types of terrestrial species such as crops, trees and leaves in wind tunnels or in open sites to obtain their drag scaling and observe their reconfiguration. In this context, studies have been done on tree crowns (Rudnicki *et al.*, 2004; Vollsinger *et al.*, 2005), crops (Sterling *et al.*, 2003) and leaves (Vogel, 1989) in wind tunnels or their natural setting to understand the effect of the streamlining and the frontal area reduction on their drag scaling. Researchers have also investigated the dynamical behavior of plants experimentally for terrestrial (Rodriguez *et al.*, 2012) and aquatic plants (Abdelrhman, 2007) or theoretically for trees (Saunderson *et al.*, 1999; Spatz *et al.*, 2007) and grasses (Brüchert *et al.*, 2003; Speck and Spatz, 2004), studying for instance the damped oscillations of plants. Reconfiguration is found to be a method to make plants stable and to

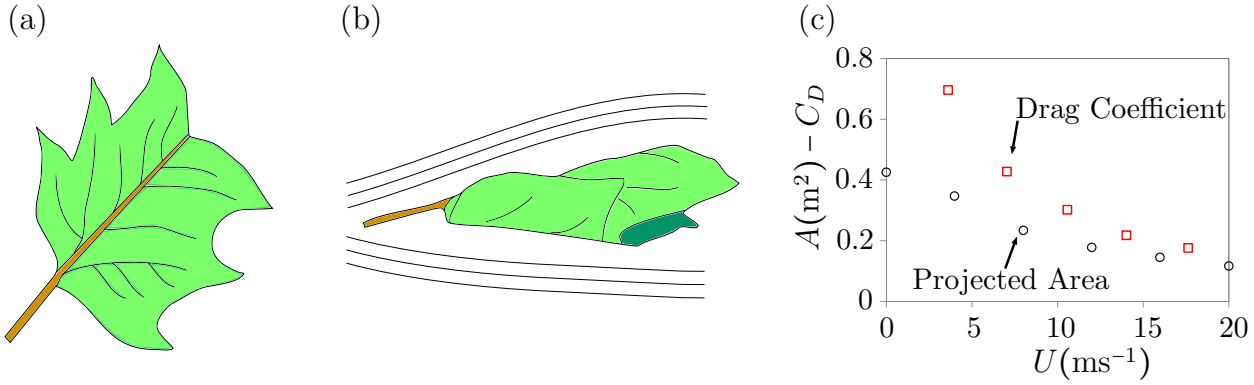

Figure 2.1 Main mechanisms of drag reduction and reconfiguration. a) An undeformed tulip tree leaf and b) the leaf reconfiguring in wind by reduction of the frontal area and the drag coefficient. b) Measurements on the crown of black cottonwood which show the reduction of the frontal area and the drag coefficient due to reconfiguration (Vollsinger *et al.*, 2005). The image of the leaf is adapted from Vogel (1989).

reduce the chance of structural failure due to flutter. For example, edges of the London planetree leaf curl to form a structure similar to a delta wing which can reduce the wind-induced vibrations and stabilize the leaf. With increasing wind speed, the leaf rolls up and becomes more stable in different modes of reconfiguration. Figure 2.4 shows the reconfiguration of a London planetree leaf in the wind tunnel for different wind speeds. In this experiment, the Reynolds number is in the range of 10^4 to 10^5 (Shao *et al.*, 2012).

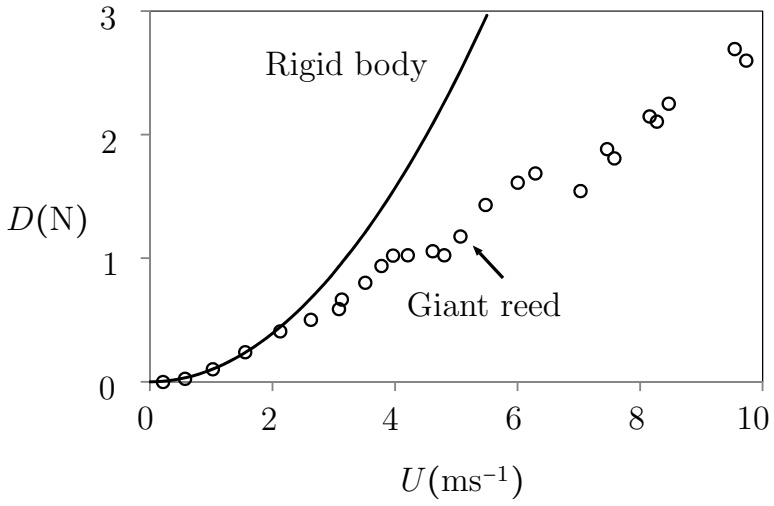

Figure 2.2 Comparison between the drag scaling of a flexible plant (giant reed) with its equivalent rigid body. Data is obtained from Speck (2003).

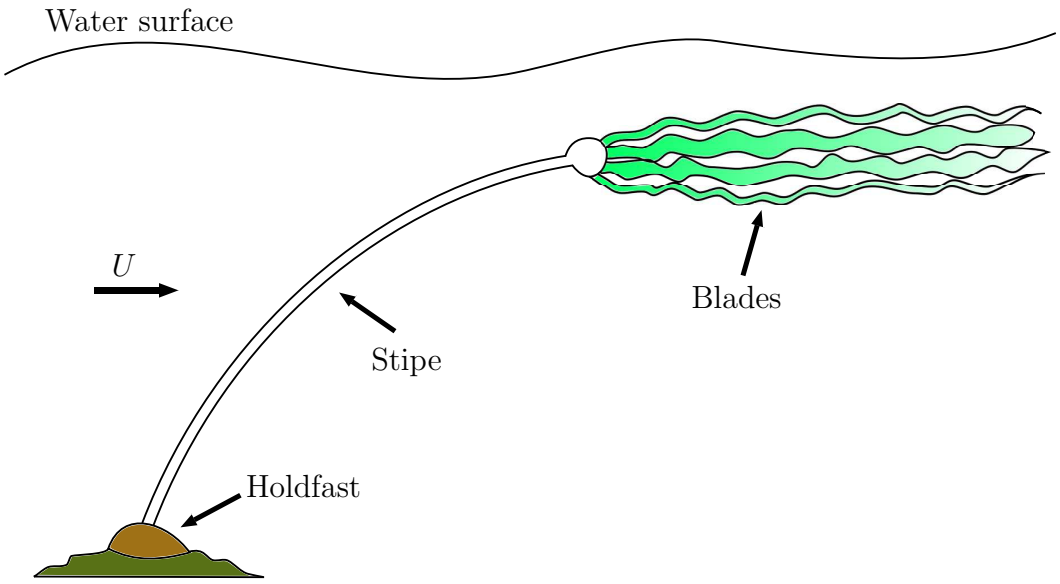

Figure 2.3 A schematic of giant kelp showing its stipe, clumped blades and the holdfast. The figure is reproduced from Johnson and Koehl (1994).

2.3 Fundamental Investigations on Reconfiguration

In the preceding sections, studies on the reconfiguration of plants whether aquatic or terrestrial were reviewed. These studies mainly deal with trees, algae, leaves and flowers. In general, plants have greater material and structural complexity in comparison with engineering structures. They have complex geometries, they are not identical and they are made of anisotropic materials. Their material properties are also not constant and change with different parameters such as moisture content and weather humidity (Glass and Zelinka, 1999). It is therefore difficult to gain a fundamental understanding of the underlying mechanisms of their reconfiguration. To gain this understanding, it is necessary to idealize plants with a simpler structure ignoring geometrical and material complexities and provide a general model which can be applied to different species of plants while giving reproducible results. So far we have seen that plants usually have flexible and slender structures and reconfigure when subjected to flow. One approach to model this phenomenon is to study simple mechanical structures with similar behavior to plants such as flexible beams and plates.

2.3.1 Dimensionless Parameters in Reconfiguration

Due to the diversity of specimens and flow conditions, it is essential to use dimensionless parameters to define the state of the system. The Cauchy number C_Y is a dimensionless parameter which is useful in fluid-structure interaction modeling. The Cauchy number repre-

Figure 2.4 Different modes of reconfiguration of the London plane tree leaf in different wind speeds to reduce the drag force and to make it more stable. The unit of velocity is ms^{-1}. Images are obtained from Shao *et al.* (2012).

sents the ratio of the fluid force to the bending rigidity of the flexible body (Chakrabarti, 2002; de Langre, 2008; Gosselin *et al.*, 2010; Gosselin and de Langre, 2011). The Cauchy number is also called "dimensionless velocity" (Alben *et al.*, 2002, 2004) or "elastohydrodynamical number" (Schouveiler and Boudaoud, 2006). For bending plates and beams fixed at one end, the Cauchy number is defined as :

$$C_Y = \frac{\rho U^2 d L^3}{2EI} \ , \tag{2.2}$$

where d and L are respectively, the width and the length of the beam or plate. In addition, ρ is the flow density and EI is the bending rigidity.

The reconfiguration number (Gosselin *et al.*, 2010) and similarly the "effective length" (Luhar and Nepf, 2011) demonstrate the effect of flexibility on the drag force which is exerted on a flexible body. The reconfiguration number is defined as the ratio of the drag force on the flexible body to the drag force of an equivalent rigid body with a similar geometry :

$$\mathcal{R} = \frac{D}{\frac{1}{2}\rho U^2 C_{D,rigid} A} \ . \tag{2.3}$$

The reconfiguration number is a measure of the drag reduction of a flexible structure because of its flexibility. It is suggested by Gosselin *et al.* (2010) that the reconfiguration number is a function of a constant drag coefficient and the Cauchy number. They define the "scaled Cauchy number" as $C_Y C_D$; this makes the reconfiguration number a function of the scaled Cauchy number only.

Figure 2.5 shows the variation of the reconfiguration number versus the Cauchy number for

three different plants and a bending fiber in fluid flow. In all cases the reconfiguration number decreases with increasing Cauchy number. For small Cauchy numbers, the reconfiguration number is near one which means that the deformation of the structure is small. This regime is equivalent to a Vogel exponent of zero. By increasing the Cauchy number, the flexible structure starts to deform therefore its drag scaling diverges from the drag scaling of rigid bodies. This reduces the reconfiguration number. In the large deformation regime where the Cauchy number is large, the drag scaling slope reaches a constant Vogel exponent.

2.3.2 Two-Dimensional Reconfiguration

A flexible beam undergoing bending due to flow is a simple academic representation of reconfiguration. For instance, to study two-dimensional reconfiguration of beams, Alben *et al.* (2002, 2004) tested glass fibers in a very thin layer of soap film to create a two-dimensional flow and be able to visualize the flow. In this experiment, a vertical soap film flow was used with film flow thickness of 1 to 3 μm and flow velocity ranging from 0.5 to 3 ms^{-1}. Thin glass fibers were then used as flexible beams to study two-dimensional reconfiguration. To theoretically model the bending fiber in the soap film flow, the authors coupled Euler-Bernoulli beam theory with an exact potential flow solution using Helmholtz's free streamline theory. The free streamline theory is used in this case to account for the wake behind the fiber. In the model, a constant pressure, different from the free stream pressure, is considered for the wake. However they had to introduce an empirical factor to account for the back pressure in the wake. Figure 2.5 shows the experimental drag measurements for a flexible glass fiber in dimensionless form. The Vogel exponent is found to be close to zero for small C_Y meaning that the glass fiber acts as a rigid body in this regime. The Vogel exponent reaches $-2/3$ in the large deformation regime (Alben *et al.*, 2002). As Gosselin *et al.* (2010) explain in detail, using dimensional analysis, the Vogel exponent can be predicted for large deformation where the initial length scale vanishes. This regime is called the asymptotic condition. In theory, this happens when the flexible structure is fully deformed and aligned with the flow so only a small fraction of the structure near its support produces pressure drag force. The regime of large deformation or asymptotic conditions cannot be reached completely in experiments because of flutter instabilities encountered for high Cauchy numbers. In this regime the initial length scale of the structure loses its role. For bending plates and beams we thus deal with a problem which can be defined by the bending rigidity per unit width, flow velocity, density and the drag force per unit width. According to the Buckingham π theorem (Buckingham,

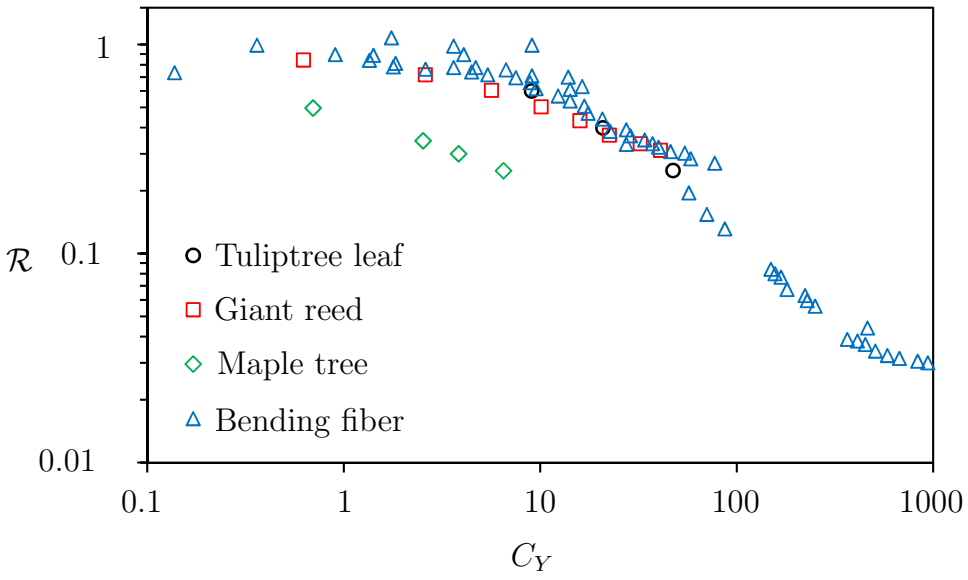

Figure 2.5 The variation of the reconfiguration number with the Cauchy number for different natural species (de Langre, 2008) compared with a fiber bending in flow (Alben *et al.*, 2002).

1914), the following single dimensionless number is sufficient to define the problem :

$$\frac{D}{d^{2/3}(EI)^{1/3}\rho^{2/3}U^{4/3}} ,$$

thus by comparing the power of the flow velocity in this dimensionless number with the definition of the Vogel exponent we obtain $D \propto U^{4/3}$ or equivalently $\vartheta = -2/3$.

Bending plates and cut disks have been modeled theoretically by coupling a semi-empirical drag formulation and the Euler-Bernoulli beam theory (Gosselin *et al.*, 2010). The theoretical model was then solved with the shooting method and Runge-Kutta integration along the beam's length. It was found that the reconfiguration of an elastic plate deforming in wind is similar to the bending fiber in soap film flow studied by Alben *et al.* (2002). Experiments on bending plates were also done in a wind tunnel with different geometries and material properties as well as cut disks, all made of transparent covers.

To study flexible aquatic plants, the Euler-Bernoulli beam model and semi-empirical drag formulation were coupled, this time considering the effect of buoyancy (Luhar and Nepf, 2011, 2016). They showed that buoyancy works against the drag force, therefore it delays the reconfiguration compared with a bending beam in wind with no buoyancy effect (Gosselin *et al.*, 2010). It was also found that for a beam bending in the water flow, the Vogel exponent is equal to $-2/3$ for large deformations ; the same result was previously obtained for bending plates in the wind flow (Gosselin *et al.*, 2010), bending fibers in soap film flow (Alben *et al.*,

2002) and tapered beams (Lopez *et al.*, 2013).

2.3.3 Three-Dimensional Reconfiguration

Although bending beams and fibers are suitable for modeling the two-dimensional bending of plants, they cannot be used for all forms of reconfiguration. Plants can also twist under fluid loading. The "twist-to-bend ratio" (Vogel, 1992; Faisal *et al.*, 2016) is defined as a dimensionless number denoted by η which is the ratio of the bending rigidity EI to the torsional rigidity GJ :

$$\eta = \frac{EI}{GJ} \ , \tag{2.4}$$

where E is the Young's modulus, I is the second moment of area or area moment of inertia, G is the shear modulus and J is the torsional constant. High values of η represent a structure which has a larger bending rigidity in comparison with the torsional rigidity so it can twist more easily than it can bend. The Young's modulus and the shear modulus are material properties while the second moment of area and the torsional constant are geometrical. For homogeneous and isotropic materials, the Young's modulus and the shear modulus are linearly related ; $E = 2G(1+\nu)$ where ν is the Poisson's ratio. However, this linear relationship is not typically applied for plants because their structure is usually inhomogeneous.

Leaves attached to petioles are good examples of twisting structures in nature. For example, the banana leaf has a coupling between the bending and torsional deformation due to a petiole with a hollow U-shape cross section. In this case, the torsional rigidity is less than the bending rigidity giving rise to a twist-to-bend ratio of approximately 70 (Ennos *et al.*, 2000). This causes the leaf to twist easily under the wind loading and consequently to bend in the direction with the lower bending rigidity.

Another interesting example of coupling between twisting and bending in nature is the daffodil flower. The daffodil's stem holds the flower horizontally and shows a combination of twisting and bending in reconfiguration. It was observed (Etnier and Vogel, 2000) that the daffodil stem has a large twist-to-bend ratio (see table 2.1) so the stem tends to twist to face downwind reducing its drag coefficient as illustrated in Fig. 2.6. The combination of twisting and bending deformation allows the daffodil flower to reduce the wind loading on its structure.

Large values of the twist-to-bend ratio have been observed in many structures in nature. Table 2.1 shows a comparison between the twist-to-bend ratios of some natural structures. In general, structures with a circular or semi-circular sections show a smaller twist-to-bend ratio compared with other section types because of the ratio of I/J (Pasini and Mirjalili, 2006). For comparison, a homogeneous and isotropic circular section has a twist-to-bend

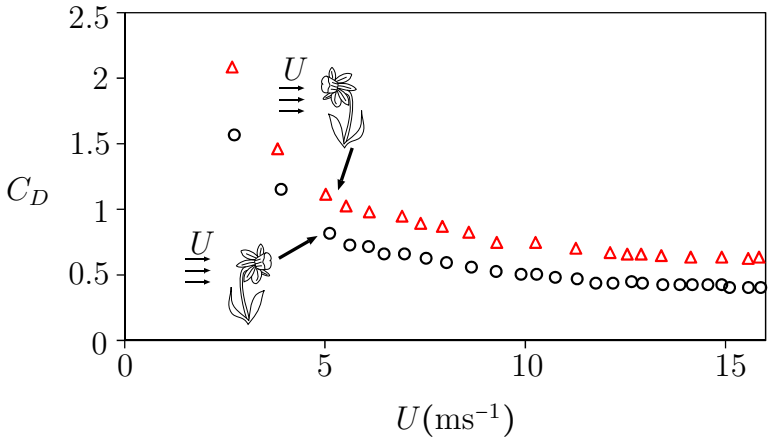

Figure 2.6 Comparison between the drag coefficient of a Daffodil flower facing downwind and upwind. Data has been extracted from Etnier and Vogel (2000).

ratio equal to $1+\nu$ or 1.5 for materials that maintain their volume in deformation. Also for a metallic circular rod, the twist-to-bend ratio is about 1.3 assuming a Poisson's ratio of 0.3.

2.3.4 Similarity in Reconfiguration

Figure 2.7a and Fig. 2.7b show the similarity between a palm tree and a poroelastic ball. In both cases, fluid passes through the bodies in addition to flowing around them. Theoretical modeling and experiments on a poroelastic ball consisting of multiple flexible filaments (Gosselin and de Langre, 2011) shows that in this case, the Vogel exponent varies depending on the density of filaments on the surface. The Vogel exponent is $-2/3$ for low surface density. This shows that in low surface density where filaments are few, each individual filament is not affected by the surrounding ones and thus acts like a simple bending fiber which leads to $\vartheta = -2/3$. The Vogel exponent reaches -1 for high surface density which has been found for coniferous trees (Vogel, 1984; Rudnicki *et al.*, 2004). This is because of an additional drag reduction mechanism for poroelastic structures which is the reduction of fluid's effective velocity as it passes through the structure.

Figure 2.7c and Fig. 2.7d show the resemblance between a tulip tree leaf and a circular flexible sheet cut along one radius which rolls up in fluid flow. The reconfiguration of a circular flexible sheet which rolls up in fluid flow was studied by Schouveiler and Boudaoud (2006). In the theoretical modeling, the bending angle of a circular plastic sheet which rolls up in fluid flow was found by minimizing its total potential energy due to the elastic bending and fluid pressure. The fluid pressure on the circular sheet was obtained from an exact solution of the potential flow since viscous effects are negligible for the range of the Reynolds number in

Table 2.1 The average of twist-to-bend ratio for some natural structures

Species	Geometry	η	Reference
Cucumber stem	semi-octagon	5.4	Vogel (1992)
Tomato stem	semi-circle	3.9	Vogel (1992)
Red maple petiole	semi-circle	2.8	Vogel (1992)
Sweet gum petiole	semi-pentagon	5.1	Vogel (1992)
Banana petiole	U-shape	68	Average of data from Ennos *et al.* (2000)
Sedge stem	semi-triangle	65	Average of data from Ennos (1993)
Daffodil stem	semi-circular	13.3	Vogel (2007)
Tree trunk	semi-circular	7.34	Vogel (2007)

their experiments. Circular plastic sheets with different size and rigidities were also tested in a water channel. The Vogel exponent was found to be $-4/3$ in the theoretical model and -1 experimentally.

Table 2.2 shows a comparison between the Vogel exponent of a variety of aquatic plants (Gaylord *et al.*, 1994), terrestrial ones (Vogel, 1984; de Langre *et al.*, 2012) and simple structures. This table shows the difference between the reconfiguration of species quantified by the Vogel exponent. Vogel exponents which are marked with an asterisk * are the theoretical values for the asymptotic regime of large deformations where the initial length scale is no longer applicable. Due to instabilities and high level of fluctuations at large deformations, the theoretical Vogel exponent can sometimes not be reached in experiments. All aforementioned flexible structures, from a bending fiber to a poroelastic ball, have different geometries, materials and flow conditions. The goal of the fundamental investigation of flexible structures with similar reconfiguring behavior to plants, is characterizing all these systems similarly. The review of the reconfiguration of some mechanical structures in addition to some species of plants, showed that they have similar reconfiguration characteristics when subjected to flow. For instance, plants with mainly two-dimensional reconfiguration, have a Vogel exponent of around -0.67 which is similar to that of bending beams and plates. As mentioned before, despite the differences between plants and simple engineering structures, similar trends are found when their reconfiguration is characterized by the reconfiguration number and the Cauchy number. This similarity is presented in Fig. 2.8 for different flexible structures subjected to fluid flow. In this logarithmic plot, the experimental reconfiguration number for several idealized structures as well as the mathematical model for a bending beam is plotted as a function of the Cauchy number. For all cases, $\mathcal{R}$ is approximately one for small Cauchy numbers. This

1. In soap film flow
2. In water flow
3. With flat blades

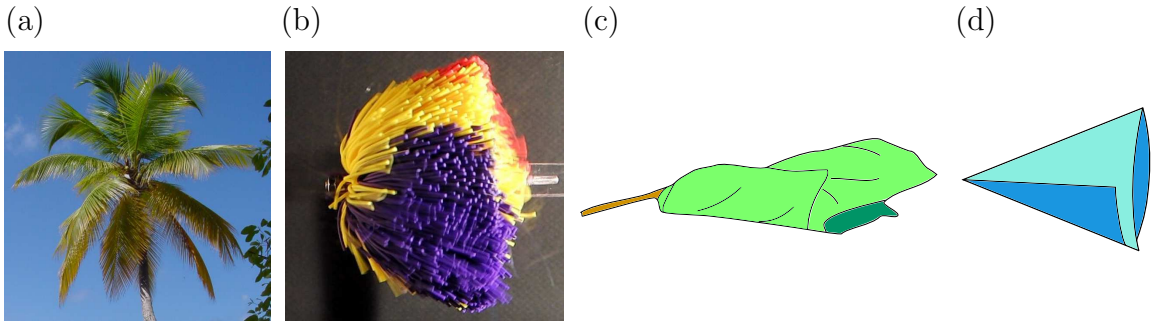

Figure 2.7 Similarity of simple mechanical structures with natural ones by comparing a) a palm tree with b) a poroelastic ball, and c) a tulip tree leaf with d) an elastic circular sheet which rolls up. The image of the palm tree is taken by Verdier (2003). The image of the poroelastic ball is extracted from Gosselin and de Langre (2011) and the others are reproduced from Schouveiler and Boudaoud (2006); Vogel (1989).

Table 2.2 The Vogel exponent for some flexible structures, aquatic and terrestrial organisms

Organism or structure	ϑ	Condition	Reference
Rigid bluff body	0	In fluid flow	-
Bending plate	−2/3 *	$U = 5 \sim 30$ ms^{-1}	Gosselin *et al.* (2010)
Bending fiber	−2/3 *	$U = 0.3 \sim 3$ ms^{-1} [1]	Alben *et al.* (2002)
Rolling up circular plate	−4/3 *	$U = 0 \sim 1$ ms^{-1} [2]	Schouveiler and Boudaoud (2006)
Daffodil flower	−0.6	$U = 2 \sim 16$ ms^{-1}	de Langre *et al.* (2012)
Poplar with leaves	−0.71	$U = 2 \sim 12$ ms^{-1}	de Langre *et al.* (2012)
Giant kelp	−1.11	$U = 1.3 \sim 2$ ms^{-1} [3]	Gaylord *et al.* (1994)
Feather boa kelp	−0.49	$U = 0.5 \sim 3$ ms^{-1}	Gaylord *et al.* (1994)
Loblolly pine	−1.13	$U = 8 \sim 19$ ms^{-1}	Vogel (1984)
Tulip tree leaf	−1.18	$U = 10 \sim 19$ ms^{-1}	Vogel (1984)

means that the amplitude of deformation is very small therefore a flexible structure acts as a rigid structure. Between $C_Y \approx 1$ and 10, depending on the case, the reconfiguration number starts to diverge from unity and decrease with increasing Cauchy number. This shows that the reconfiguration of these structures is fundamentally similar.

2.4 Chirality in Natural Structures

Many aquatic and terrestrial plants possess a slender structure with a chiral morphology. In mechanical engineering, a chiral structure is a structure which is twisted around its centerline in its natural state. Chirality is also found in organic structures such as DNA (Arbona *et al.*, 2012; Zhao *et al.*, 2015), synthesized ones such as polymers (Ye *et al.*, 2010) and nanomaterials (Chen *et al.*, 2005; Ji *et al.*, 2012; Zhao *et al.*, 2014). For example, Fig. 2.9a shows a

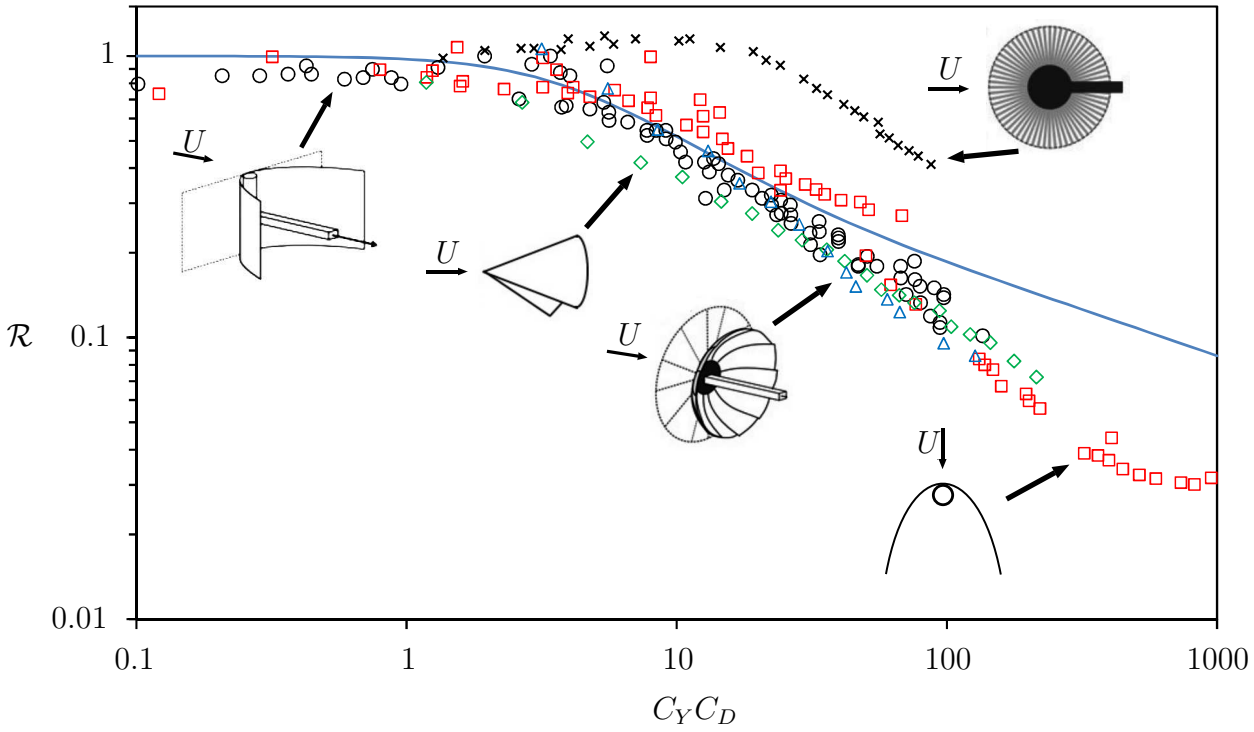

Figure 2.8 Similar trend of experimental results of different specimens subjected to flow and characterized by the reconfiguration number and the scaled Cauchy number for cut disks △ and a bending rectangular plate ○ (Gosselin *et al.*, 2010), poroelastic ball × (Gosselin and de Langre, 2011), circular flexible plate which rolls up in flow ◇ (Schouveiler and Boudaoud, 2006) and bending fibers □ (Alben *et al.*, 2004). The line represents the mathematical model for the two-dimensional reconfiguration of a plate in flow (Gosselin *et al.*, 2010). Images are extracted from the mentioned references.

carbon nanotube rope and Fig. 2.9b shows a cattail leaf both with a chiral morphology. In nature, it seems that upright plants with chirality are less vulnerable to wind loading and buckling (Schulgasser and Witztum, 2004; Zhao *et al.*, 2015; Rowlatt and Morshead, 1992). For instance, Schulgasser and Witztum (2004) show that large twist angles in flat upright leaves can lead to approximately 25 percent increase in the critical buckling length under self-weight loading. Thus, it is concluded that chirality helps upright plants to grow higher than untwisted ones without undergoing structural failure under their own weight. This may be evidence of adaptation of this type of plants to their environment through a long evolution process. The evolutionary aspect of chirality in biological structures has been discussed in many studies. For instance, it is of great interest to know whether the chiral morphology of DNA was a requirement or an outcome of evolution (Lunine *et al.*, 1999) since the chiral morphology of DNA leads to a minimum free energy (Ji *et al.*, 2012).

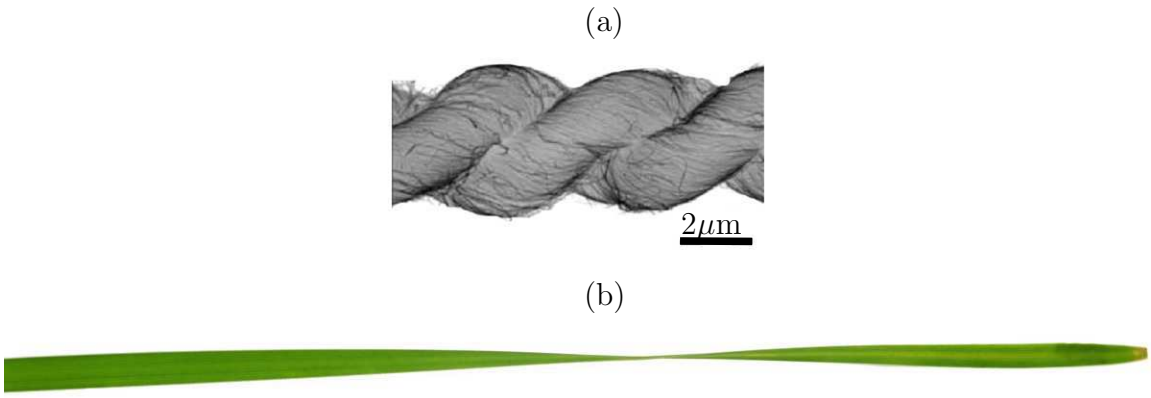

Figure 2.9 a) a carbon nanotube rope with a chiral morphology (Zhao *et al.*, 2014) and b) a chiral cattail leaf .

Chiral structures have been studied fundamentally using different mathematical models. For example, the Timoshenko beam model has been used to study the dynamics of twisted beams (Chen *et al.*, 2013) and the static stability of chiral upright plants (Zhao *et al.*, 2015). In the latter, the authors use a linear Timoshenko beam theory with a twisted section to model aquatic macrophytes assuming that the beam is linearly elastic with homogeneous and isotropic properties. In their buckling analysis, they assume a distributed compressive load along the length of the beam to mimic its weight plus a compressive point force at the free end to simulate a head organ. For the aerodynamic loading, they assume a distributed force which is simply proportional to the projected area of an undeformed beam. Importantly, they assume small deformations. Within their linear framework, they conclude that chirality improves the stability and resistance of upright emergent leaves against high winds and buckling.

To consider large three-dimensional deformations, Kirchhoff theory of rods has been used in several studies related to chirality such as in the behavior of tendrils of climbing plants (Goriely and Tabor, 1998), dynamics of helical strips (Goriely and Shipman, 2000), nanosprings (da Fonseca and Galvão, 2004), formation of chiral nanomaterials (Wang *et al.*, 2012) and chiral carbon nanotube ropes (Zhao *et al.*, 2014). For example, (da Fonseca and Galvão, 2004) use a classic Kirchhoff rod with intrinsic twist and curvature to study the structural properties of nanosprings. They evaluate the Hooke's constant of the nanosprings directly from their twist and curvature. Wang *et al.* (2012) also use a modified Kirchhoff model to take into account the effect of surface stresses. They state that the morphology of quasi-one-dimensional nanotubes is affected by the the surface stress. Despite the vast use of the Kirchhoff rod model, it is not applicable for the problems which involve elongation. To take elongation into account, Wang *et al.* (2014) develop a Cosserat rod model to study the growth of towel gourd tendrils.

2.5 Theoretical Framework for Modeling Plants

As noted earlier, plants can be modeled as slender flexible structures which bend in fluid flow. However, plants twist and bend simultaneously under fluid loading and their deformation can be very large. Therefore, an appropriate model is necessary to simulate large deformations of slender structures subjected to flow. Euler-Bernoulli beam is a mathematical model which has been used widely to model the deformation of plants (Alben *et al.*, 2002; Gosselin *et al.*, 2010; Luhar and Nepf, 2011). There is also the Timoshenko beam model to include the shear deformation which is ignored in the Euler-Bernoulli beam. However, for structures that are slender enough, the Euler-Bernoulli beam is generally accurate.

Although the Euler-Bernoulli beam model is simple and convenient, it does not take into account three-dimensional deformation. Therefore, in the present study, we consider the Kirchhoff model of elastic rods. An elastic rod is a three-dimensional slender structure where its length (L) is much larger than the other two dimensions which make its cross section. Kirchhoff's theory of rods is a classic theory considering finite displacements while neglecting the shear deformation and assuming small strains (Dill, 1992). In the theory, the rod is represented by an "inextensible" curve in three-dimensional space. As detailed by Audoly and Pomeau (2010), to track the twist of the centerline, a "material frame" is defined as a moving coordinate system $(\mathbf{e}_x, \mathbf{e}_y, \mathbf{e}_z)$ attached to the centerline (Fig. 2.10). Based on the Kirchhoff rod model, it is assumed that $\mathbf{e}_z$ is tangent to the centerline and remains perpendicular to the cross section through the rod's deformation. Without loss of generality, we consider that $\mathbf{e}_y$ is along the more rigid direction of the cross section. Due to the small strain assumption, the defined material frame remains orthonormal. This is also called the Euler-Bernoulli hypothesis or the unshearable rod assumption. The set comprising the centerline and the material frame is sometimes called the "Cosserat curve" (Audoly and Pomeau, 2010).

For a rod under distributed and point forces, the total applied force is written :

$$\mathbf{F}(s) = \left(\int_s^L \mathbf{p}(s')ds' \right) + \mathbf{p}(L) \ , \tag{2.5}$$

where s is the arclength, $\mathbf{p}$ is the distributed loading and $\mathbf{p}(L)$ is a point force at $s = L$. In addition, $\mathbf{F}(s)$ is the vector of external forces which is also equivalent to the vector of internal forces at the cross section located at s. Using the principle of virtual work we have :

$$\frac{d\mathbf{M}(s)}{ds} + \mathbf{e}_z(s) \times \mathbf{F}(s) + \mathbf{q}(s) = 0 \ , \tag{2.6}$$

where $\mathbf{M}(s)$ is the vector of internal moments and $\mathbf{q}(s)$ is the vector of distributed external

torques in the three directions of the material frame. The Kirchhoff model of rods is usually written as a set comprising Eq. (2.6) and the spatial derivative of Eq. (2.5). These two equations are evaluated for each of the three directions of the material frame which leads to a system of six differential equations. The curvatures around $\mathbf{e}_x$ and $\mathbf{e}_y$ are termed κ_x and κ_y, and the twist around $\mathbf{e}_z$ is termed τ. The material frame is connected to the centerline of the rod and follows its twist and deformation (Audoly and Pomeau, 2010).

There are several approaches to represent the rotation of the material frame with respect to a fixed Eulerian frame. "Euler angles" are the most common three-parameter representation and are named pitch θ, roll ϕ and yaw ψ. These angles are related to curvatures and twist using three differential equations (Love, 1944) :

$$\kappa_x = \frac{d\theta}{ds}\sin\phi - \frac{d\psi}{ds}\sin\theta\cos\phi \ , \tag{2.7}$$

$$\kappa_y = \frac{d\theta}{ds}\cos\phi + \frac{d\psi}{ds}\sin\theta\sin\phi \ , \tag{2.8}$$

$$\tau = \frac{d\phi}{ds} + \frac{d\psi}{ds}\cos\theta \ . \tag{2.9}$$

The state of the rod can be fully defined by coupling these three equations with the Kirchhoff model of rods. Although the Euler angles are directly identifiable in 3D problems and minimize the number of governing equations of a rod, they have some limitations. Equations

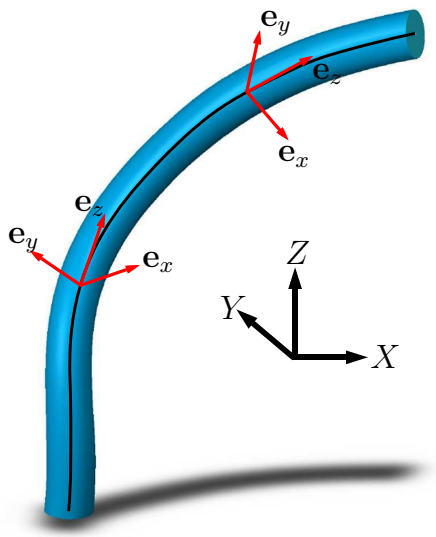

Figure 2.10 A rod connected to a fixed coordinate system with moving material frames connected to its centerline.

which relate the Euler angles to curvatures have sine and cosine terms which make them non-linear and difficult to solve. Solving these equations also implies mathematical singularities at specific angles where the determinant of the Jacobian matrix approaches zero. These singularities are discussed in detail by Ang and Tourassis (1987).

Another method to represent the moving material frame is using "quaternions" (Hamilton, 1853). Quaternions form a four-parameter representation of the rotation of the material frame without singularities unlike the Euler angles. According to Euler's theorem of rotation, the orientation of the material frame can be represented by a single rotation angle Φ about a vector $\mathbf{b} = (b_x, b_y, b_z)$ (Lazarus *et al.*, 2013). The combination of these four parameters make a quaternion as :

$$\tilde{\mathbf{Q}} = \left[b_X \sin\frac{\Phi}{2}, b_Y \sin\frac{\Phi}{2}, b_Z \sin\frac{\Phi}{2}, \cos\frac{\Phi}{2} \right] . \tag{2.10}$$

The "direction cosines" are another representation of the material frame's rotation (Love, 1944). They do not have singularities and their equations are linear unlike the Euler angles. They are also conceptually simple while the quaternions are more abstract. Direction cosines are the cosines of the angles between a vector and the three directions forming the fixed coordinate system. Since the material frame and the fixed frame have three directions each, nine direction cosines are needed to define the material frame. Six of the direction cosines are independent and the others can be calculated from these six independent ones. Table 2.3 shows a comparison of the advantages and disadvantages of the three different representations of the material frame presented above. Since singularities should be avoided, the Euler angles are rejected. Direction cosines are chosen over quaternions despite requiring more differential equations because they are conceptually simple. Direction cosines will be detailed in Chapter 3.

A special case of the deformation of a rod is pure bending under a distributed load. Since the deformation is two-dimensional, the flexible structure acts as a beam. The twist of the material frame is not needed and the beam can be defined by its centerline using Eq. (2.5) and (2.6). In this case, $p(s)$ is the distributed load acting in the bending direction and the bending moment is $M(s) = -EId\theta/ds$ where θ is the bending angle. In addition, the tensile

Table 2.3 A comparison between advantages and disadvantages of three different representations of the material frame

	Euler angles	Quaternions	Direction cosines
Singularity free		✓	✓
Conceptually simple	✓		✓
Fewer equations	✓	✓	

force in the beam is neglected. Simplifying the Kirchhoff equations, one differential equation known as the Euler-Bernoulli beam model can define the state of the bending beam :

$$EI\frac{d^3\theta}{ds^3} = p(s) \ . \tag{2.11}$$

The present study deals with the deformation of rods therefore the geometry and the aerodynamic loading are not constant and change with the state of rod. CFD methods are a possibility to find the aerodynamic loading on deformed rods but these method demand a great computation time. An approximate alternative is to calculate the fluid loading on a flexible structure using the exact solution for inviscid and incompressible flow or the potential flow using the free streamline theory. Since the exact potential flow solution leads to zero drag force, which is known as d'Alembert's paradox, it is necessary to use Helmholtz's free streamline theory to predict the separation behind a structure in fluid flow. Using this approach, it is possible to obtain the pressure drag exerted on structures in fluid flow (Sobey, 2000). In the method, the free streamline divides the flow around the body to two regions one of which is the wake behind the body and the other is the inviscid and irrotational flow outside the wake (Alben *et al.*, 2002).

The Finite Element Method and the Finite Difference Method are also candidates to solve problems which include the fluid-structure interaction. These methods have been used in several studies such as a swinging filament in uniform flow (Huang *et al.*, 2007), a flapping filament in a soap film (Zhu and Peskin, 2002), a largely deformed net in water flow (Moe *et al.*, 2010) and a hanging aerial fuel hose (Zhu and Meguid, 2007).

Taylor (1952) suggested a semi-empirical formulation to obtain the drag force on an oblique cylinder in three-dimensional flow. This method can also be used to estimate the drag force on a deformed rod. It was suggested that for the range of Reynolds number Re from 20 to 10^5, the pressure drag coefficient is approximately constant. For this range, the coefficient of friction drag normal to the centerline is $4Re^{-0.5}$ (Taylor, 1952). Taylor stated that only the normal component of the flow velocity to the cylinder's centerline contributes to the pressure drag force. This method is preferred in the present work due to its simplicity and will be explained in Chapter 3. The normal drag force on an oblique cylinder is thus calculated as :

$$p_n = \frac{1}{2}\rho U^2 A(C_{D,p}\sin^2\theta + 4Re^{-0.5}\sin^{1.5}\theta) \ , \tag{2.12}$$

where $C_{D,p}$ is the pressure drag coefficient and θ is the local angle between the cylinder's centerline and the flow direction. In this equation, the first term is the contribution of fluid pressure and the second term the contribution of the friction drag. The longitudinal force

along the centerline of the deformed rod is due to the friction force along the length of the rod :

$$p_z = \frac{1}{2}\rho U^2 A(5.4\mathrm{Re}^{-0.5}\cos\theta.\sin^{0.5}\theta) \ . \tag{2.13}$$

The inviscid dynamic fluid force on a deformed rod can be calculated using slender-body theory (Lighthill, 1960; Schouveiler *et al.*, 2005). According to this theory, the dynamic fluid force is proportional to the curvature of the rod :

$$F_d = -\rho A U^2 \frac{d\theta}{ds}\cos^2\theta \ . \tag{2.14}$$

where ρA is the added mass of fluid per unit of length. This force is produced because of the changing of the relative velocity of a body in fluid flow. In the present study, the large deformation of rods will be evaluated by coupling the Kirchhoff rod model with the aforementioned semi-empirical drag formulation. In the model, the normal and the longitudinal friction drag in addition to the dynamic fluid force will be ignored because in the present study, they are negligible compared with the normal drag force.

2.6 Biomimetics : Aeroelastic Tailoring

The passive reconfiguration of plants in nature inspires the design and fabrication of flexible wings and wind turbine blades with "morphing capabilities". This concept is usable in airplanes (Shirk *et al.*, 1986), drones (Ifju *et al.*, 2002; Weisshaar *et al.*, 1998), wind turbine blades (De Goeij *et al.*, 1999) and sport cars (Thuwis *et al.*, 2009). In the context of morphing structures, aeroelastic tailoring was developed for aerospace applications to design flexible structures to take advantage of deformation under flow loading. In general, aeroelastic tailoring is defined as "the embodiment of directional stiffness (rigidity) into an aircraft structural design to control aeroelastic deformation, static or dynamic, in such a fashion as to affect the aerodynamic and structural performance of that aircraft in a beneficial way" (Shirk *et al.*, 1986). Directional rigidity or asymmetric stiffness (De Goeij *et al.*, 1999) refers to the existence of different bending rigidities in different directions. Using aeroelastic tailoring, the aerodynamic center of the wing's section can be located behind the shear center (elastic axis or torsional axis) to produce a negative pitching moment which has a stabilizing effect when considering static divergence (Lago *et al.*, 2013). The shear center is a point on the cross section of the body where the applied force does not create torsional deformation.

Aeroelastic tailoring is not limited to the aerospace industry. In fact, directional stiffness can have many applications where flexible structures made of composite materials are used to improve the aerodynamic performance of structures (De Goeij *et al.*, 1999). For example,

in Formula 1 cars, a large downward force is needed to provide enough grip to stabilize the vehicle in tight turns. The major part of this force is provided by aerodynamic surfaces such as the front and rear wings (Zhang *et al.*, 2006). In this case, the goal of aeroelastic tailoring is to build a wing which can generate a high downward force coefficient at low speeds and deform passively to create less drag coefficient at high speeds allowing the car reach higher velocities in straight line (Thuwis *et al.*, 2009). In wind turbines, aeroelastic tailoring is used to couple bending and torsional deformation in blades. Using this approach, any change in wind speed causing bending deformation induces torsional deformation which alters the angle of attack. This has two advantages : first it can increase the fatigue life of blades because changing the angle of attack can reduce the effect of sudden loads caused by gusts. Secondly, tailored turbine blades can be designed to have an optimum angle of attack at each wind speed for optimum power generation (De Goeij *et al.*, 1999).

2.7 Problem Identification

Fundamental studies on simplified structures such as beams and plates have made it possible to understand the underlying mechanisms of reconfiguration of plants. This approach can help to predict the behavior of plants and even prevent wind damage. In this context, researchers have studied different flexible structures with a variety of geometries, materials and flow conditions to model plants as a classic fluid-structure interaction case. However, we deal with very large deformations in the reconfiguration of plants unlike in most engineering components such as wind turbine blades. Due to the simplicity of the beam models used to simulate the plants, researchers could investigate the effect of a range of parameters on reconfiguration. For example, the reconfiguration of plants can be characterized by the Vogel exponent. Similar values of the Vogel exponent are found for plants with similar mechanisms of reconfiguration. Although these studies cover the essence of reconfiguration, they mainly focus on the bending deformation (Alben *et al.*, 2002; Schouveiler *et al.*, 2005; Gosselin *et al.*, 2010; Luhar and Nepf, 2011). However, it is well known that plants also twist. In fact, many plants have large twist-to-bend ratios and twist when subjected to flow (Vogel, 1992; Etnier, 2003; Vogel, 2007). The following question therefore arises : What is the effect of torsional deformation in reconfiguration of plants and flexible structures ? The answer to this question is of great importance since it leads to a better and more accurate understanding of reconfiguration of plants in nature. However, to our knowledge, this is missing from the literature. Thus, further studies are required to evaluate the effect of torsional deformation in the reconfiguration of plants. Since the model of the bending beam cannot represent the torsional deformation of plants, a rod model is used to idealize plants.

Many species of plants have upright stems and leaves with a chiral morphology. These structures show a coupled bending and torsional deformation when subjected to flow and gravity. Studies on the chiral morphology of plants suggest that chirality increases the buckling stability (Schulgasser and Witztum, 2004; Zhao *et al.*, 2015). In addition, chirality seems to have an important role in the formation of different biological (Ji *et al.*, 2012) and artificial microstructures (Zhao *et al.*, 2014). Despite all the research in this field, a comprehensive study of the reconfiguration of chiral plants undergoing an arbitrary large deformation in fluid flow is missing from literature. In the present study, we aim to evaluate how chirality affects the drag reduction and the buckling stability of plants.

Finally, a mathematical model is developed to study a wide range of plants whether aquatic or terrestrial, chiral or non-chiral as an elastic rod undergoing a large deformation. The aerodynamic model used in this study is simple and at the same time accurate enough to simulate a real flow around plants with different cross sections. Moreover, the concept of passive reconfiguration of plants has been used in designing many mechanical structures which interact with fluid flow such as wings and blades with morphing capabilities. These structures are built flexible to have a better aerodynamic and structural performance. Although this concept is well established, very large deformations of flexible structures with morphing capabilities have not been studied thoroughly. Therefore, the present mathematical framework could also be used to model the interaction of these structures with the flow in large deformations.

CHAPTER 3 ARTICLE 1 : LARGE COUPLED BENDING AND TORSIONAL DEFORMATION OF AN ELASTIC ROD SUBJECTED TO FLUID FLOW

M. Hassani, N. W. Mureithi and F. P. Gosselin, 2016, published in the journal of *Fluids and Structures*.

Abstract

In the present work, we seek to understand the fundamental mechanisms of three-dimensional reconfiguration of plants by studying the large deformation of a flexible rod in fluid flow. Flexible rods made of polyurethane foam and reinforced with nylon fibers are tested in a wind tunnel. The rods have bending-torsion coupling which induces a torsional deformation during asymmetric bending. A mathematical model is also developed by coupling the Kirchhoff rod theory with a semi-empirical drag formulation. Different alignments of the material frame with respect to the flow direction and a range of structural properties are considered to study their effect on the deformation of the flexible rod and its drag scaling. Results show that twisting causes the flexible rods to reorient and bend with the minimum bending rigidity. It is also found that the Vogel exponent of a reconfiguring rod is not affected by torsion. Finally, using a proper set of dimensionless numbers, the state of a bending and twisting rod is characterized as a beam undergoing a pure bending deformation.

3.1 Introduction

In contrast to engineering structures, plants are generally flexible and deform significantly under fluid loading. This deformation typically causes drag reduction and is called *reconfiguration* in biomechanics (Vogel, 1984, 1989). Unlike rigid bluff bodies, the drag force on plants is not proportional to the square of the flow velocity. The drag force on flexible plants varies with the flow velocity as

$$D \propto U^{2+\vartheta}, \tag{3.1}$$

where ϑ is the Vogel exponent. This exponent quantifies the effect of flexibility on the drag scaling and is typically negative for plants (Vogel, 1984). Plants reconfigure using two main mechanisms : frontal area reduction and streamlining. The more negative ϑ is, the more the drag is reduced due to reconfiguration.

Many experimental drag measurements have been performed on trees (Vollsinger *et al.*, 2005), crops (Sterling *et al.*, 2003) and algae (Koehl and Alberte, 1988) whether in wind tunnels, water flumes or their natural setting. This was done to quantify the effect of streamlining and frontal area reduction on drag scaling. Understanding reconfiguration is necessary to predict or prevent the adverse effect of strong winds or water flows on plants such as windthrow, uprooting and lodging (Rudnicki *et al.*, 2004; Berry *et al.*, 2004). *Thigmomorphogenesis*, or the influence of mechanical stimuli such as wind loading on the growth of plants, is another area where a better understanding of plant-flow interaction can make a contribution (Niklas, 1998).

In general, plants are slender and a fundamental understanding of their reconfiguration has therefore been sought by modeling them as bending beams and plates (Alben *et al.*, 2002, 2004; Gosselin *et al.*, 2010; Luhar and Nepf, 2011; Gosselin and de Langre, 2011; Schouveiler and Boudaoud, 2006). A flexible beam undergoing bending due to flow is a simple academic representation of reconfiguration. For instance, the deformation and the drag of flexible glass fibers have been measured in a two-dimensional soap film flow which allows modeling and flow visualisation (Alben *et al.*, 2002, 2004). To theoretically model the bending fiber in the soap film flow, the authors coupled the Euler-Bernoulli beam theory with an exact potential flow solution using the Helmholtz free streamline theory. Bending plates made of transparency films were also studied in a wind tunnel (Gosselin *et al.*, 2010). Theoretical representation of these experiments was done by coupling a semi-empirical drag formulation and the Euler-Bernoulli beam theory.

Although bending beams and fibers capture the essence of the two-dimensional deformation of plants, they cannot represent all forms of reconfiguration. Other effects are important in reconfiguration and can influence the Vogel exponent such as buoyancy (Luhar and Nepf, 2011), poroelasticity (Gosselin and de Langre, 2011) and three dimensional bending deformation (Schouveiler and Boudaoud, 2006). Moreover, the approach of using simple structures was also employed to study inelastic brittle reconfiguration, i.e., pruning (Lopez *et al.*, 2011; Eloy, 2011).

While the aforementioned fundamental studies focus on bending deformation, torsion has been ignored in reconfiguration. However, it is known that plants twist significantly under fluid loading. For instance, the stem of a daffodil holds the flower horizontally and twists at the slightest breeze aligning the flower downwind thus reducing its drag (Etnier and Vogel, 2000). The trunks of trees with crown asymmetry also undergo significant twist under wind loading. Because of their fibrous construction, plants and trees are known to twist more easily than they bend (Vogel, 1992; Skatter and Kučera, 1997). This is quantified by the

twist-to-bend ratio,

$$\eta = \frac{EI}{GJ} \ , \tag{3.2}$$

where EI is the bending rigidity and GJ is the torsional rigidity. High values of η represent a structure which can twist more easily than it can bend. Table 3.1 shows a comparison between the twist-to-bend ratios of some natural and engineering structures. In comparison to engineering structures, branches, petioles and stems have a significantly larger value of η (Vogel, 1992; Pasini and Mirjalili, 2006). Figure 3.1a shows a schematic of the U-shape cross section of a banana petiole with a large twist-to-bend ratio of 68. As a result, a banana leaf twists while bending downwind (see Fig. 3.1b and c). For comparison, a homogeneous and isotropic material with circular section has a twist-to-bend ratio equal to $1 + \nu$ or 1.3 for metallic materials assuming the Poisson's ratio is about 0.3 (Vogel, 1992).

Since many plants twist when subjected to flow, the following question arises : What is the effect of torsional deformation on the reconfiguration of plants and flexible structures, and how does it change their drag scaling, i.e., their Vogel number ? The bending beams and plates of the previous studies cannot represent the torsional deformation of plants. Therefore a new approach is necessary to idealize plants with simple structures. In this paper, we consider the reconfiguration of an elastic rod which can twist and bend. A mathematical model is developed considering the arbitrary large deformation of a rod subjected to fluid flow. Tests are also done in a wind tunnel on flexible rods made of polyurethane foam with strategically placed reinforcements to tailor their twist-to-bend ratio and their twisting-bending coupling.

Table 3.1 The average of twist-to-bend ratio for some natural and engineering structures

Species	Geometry	η	Reference
Isovolumetric material	circular	1.5	-
Metallic rod	circular	1.3	-
Daffodil stem	semi-circular	13.3	Vogel (2007)
Banana petiole	U-shape	68	Ennos *et al.* (2000)
Sedge stem	semi-triangle	65	Ennos (1993)
Tree trunk	semi-circular	7.34	Vogel (2007)

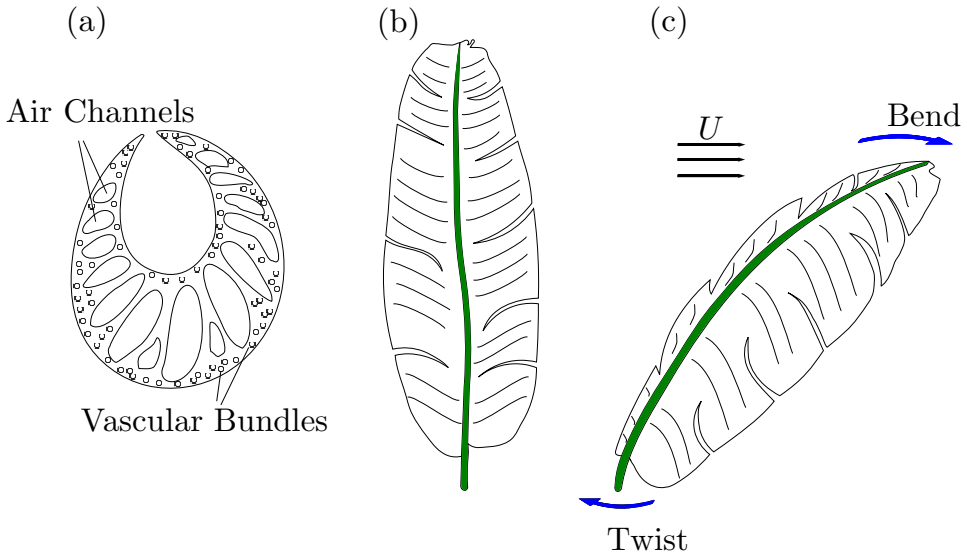

Figure 3.1 Schematics of a banana leaf (a) U-shape cross section of its petiole with a large twist-to-bend ratio ; (b) upright banana leaf ; and (c) leaf twisting to bend downwind. Inspired by Ennos *et al.* (2000).

3.2 Methodology

3.2.1 Experimental Procedure and Materials

The large deformation of a flexible rod bending and twisting under pressure drag is studied. The tests are performed in the closed-loop wind tunnel of the laboratory of Aerodynamics and Fluid-Structure Interactions at École Polytechnique de Montréal. The wind tunnel has a square test section of 60×60 cm^2 and can produce a maximum air speed of 90 ms^{-1}. Figure 3.2 shows the custom-made load measuring equipment used for the wind tunnel tests. The test setup consists of a force balance (3), a speed reduction gearbox (2), and a rotary servo motor (1) mounted on the gearbox. The 6-axis force balance (ATI GAMMA, ATI Industrial Automation, Apex, North Carolina) used in the present experiment, measures the aerodynamic forces in addition to the bending and twisting moments. The set of the servo, gearbox and force balance is mounted on an aluminum frame (4) and a wooden panel (5) which is used to support the setup on top of the wind tunnel. The rod (6) is fixed to the force balance inside the test section of the wind tunnel.

The ATI GAMMA force transducer was calibrated to measure a maximum 32 N of transverse loading, 100 N of axial loading and 2.5 Nm of torque and bending moments. The resolution of the force transducer is 6.25×10^{-3} N for the transverse loading, 12.5×10^{-3} N for the axial loading and 0.5×10^{-3} Nm for the moments. From static tests with a calibration weight of

200 g, we estimate the precision of the static force measurement to be within 1 percent of the time-averaged reading. Moreover, in the wind tunnel tests, the standard deviation of the time fluctuating forces and moments, mainly due to turbulence buffeting, was evaluated to be between 4 and 10 percent of the time-averaged measurement. For the velocity range of the present experiments, vortex shedding excitation is not significant because the predicted shedding frequency for a Strouhal number of 0.2 is more than 40 Hz while the fundamental frequency of the specimens is of the order of 1 Hz. Hence the measurements represent static values of the lightly fluctuating loads averaged over 30 seconds.

Rods are slender structures which can bend and twist. Rods with circular sections are used to simplify the geometry and the aerodynamic loading evaluation. For non-circular rods, fluid loading depends on the angle of each section of the rod with the flow direction i.e. the local angle of attack. The loading on a circular rod, however, is independent of the twist of the rod's sections. Moreover, the flow on a normal cylinder is on average symmetric and is not expected to generate a twisting moment. Coupling between torsional and bending deformation is achieved through *directional rigidity* which induces torsional deformation in a bending rod. This coupling gives rise to three-dimensional deformation. Herein, directional

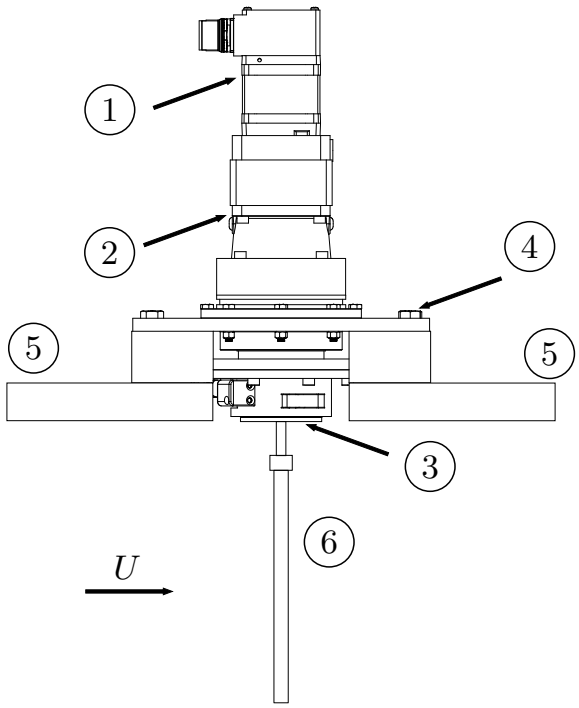

Figure 3.2 Schematic of the test setup installed on top of the wind tunnel. The setup consists of a servo (1), gearbox (2), force balance (3), aluminum frame (4), wooden panel (5) and a rod specimen (6).

rigidity or asymmetric stiffness (De Goeij *et al.*, 1999) refers to different bending rigidities in different directions.

Using this concept, composite rods are made using polyurethane foam and are reinforced in one direction using nylon fibers (see Fig. 3.3). Nylon fibers are pre-aligned along the axis of a non-stick Teflon tube. They are distributed along one diameter in the cross section of the rod to achieve directional rigidity. Two types of nylon fibers with different diameters and Young's moduli are used : d_f = 0.3 mm and E_f = 3300 MPa, d_f = 0.75 mm and E_f = 2360 MPa. The two-component polyurethane foam used (Flexfoam-iT, Smooth-on Inc., Easton, Pennsylvania) expands up to 6 times its original volume upon mixing. The mixture is poured and pressurized in the tube and left to harden over 4 to 5 hours (see Chapter 5 for more detail).

The rigidity of the rod depends on the amount of foam inside the mold, diameter of the fabricated rod, thickness and the distance of the fibers from the rod's neutral axis. Three-point bending tests are performed to determine the bending rigidities in the x and y-directions (Fig. 3.3). The directions x and y construct a *material frame* defined with the alignment of the reinforcement fibers.

The torsional rigidity of the rod is determined by measuring the frequency of torsional oscillation of the rod attached to a heavy weight at one end and fixed at the other. The system is designed to oscillate around the rod's centerline so the torsional rigidity is calculated from the measured frequency as $GJ = LJ_m{\omega_n}^2$. In this equation, J_m is the mass moment of inertia of the system around the rod's centerline and ω_n is the measured natural frequency of the rotational oscillation (see Chapter 5 for more detail). Table 3.2 shows the characteristics of tested specimens made of polyurethane foam.

In the experimental study, the rod is attached to the 6-axis force balance on one end via a 10 cm mast and is free at the other end. Normally, a cantilever rod under transverse loading is considered to have a fixed position and slope at the fixed end. However, in our experiments, the rod is made of a soft material which cannot be easily clamped to maintain a constant slope at its fixed end when subjected to wind loading. Trying to clamp the fixed end of the foam rod pinches it, thus inducing a rotation about its fixed end instead of a smooth deformation

Table 3.2 Physical properties of tested specimen

Specimen	L (cm)	d (cm)	$(EI)_y$(Nm^2)	$\frac{(EI)_y}{GJ}$	$\frac{(EI)_y}{(EI)_x}$	Weight (g)
R1	30	3.17	0.0563	1.00	0.41	120
R2	28	2.54	0.0262	1.26	0.24	65
R3	25	1.58	0.0033	1.20	0.21	20

along its length. To take into account this imperfection in the boundary condition, the fixed end is considered as a torsion spring in the mathematical model. The torsion coefficient of the spring (k_s) is then evaluated using the measured in-plane bending moment and the rotation angle at the clamped end captured from photographs. A linear relation is considered between the in-plane bending moment and the rotation angle :

$$M_Y = k_s \alpha_s \ , \tag{3.3}$$

where M_Y is the in-plane bending moment at the clamped end while Y is perpendicular to the flow direction (Fig. 3.3). In addition, α_s is the rotation angle at the clamped end (see Chapter 5 for more detail).

The fixed end of the rod is rotated incrementally around its central axis in the wind tunnel using the servo motor shown in Fig. 3.2. This is done to expose different alignments of the reinforcement direction at the clamped end with respect to the flow direction making an *angle of incidence* ψ_0 (see Fig. 3.3). For each angle of incidence, the drag scaling is evaluated for a range of flow velocities. A variety of dimensions, structural rigidity and bending-torsion coupling are therefore considered to study the effects of various parameters on the deformation of the flexible rod and its drag scaling. Measurements are performed for flow velocities ranging from 5 ms^{-1} to 65 ms^{-1} and angles of incidence ranging from 0 to 90 degrees. The Reynolds number for the tests varies from approximately 1.5×10^4 to 10^5 for R1 and R2 and from 5×10^3 to 6.5×10^4 for R3.

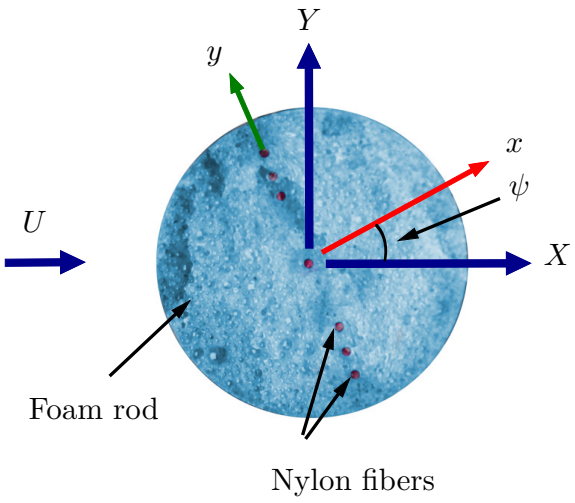

Figure 3.3 Photograph of a flexible rod's section made of polyurethane foam and reinforced with nylon fibers which have an angle of incidence ψ with the flow. The angle of incidence at the clamped end is defined by ψ_0.

Images of the test specimens are captured in the wind tunnel using a DSLR camera. For the side view, a 60×60 cm^2 LED panel was placed behind the test specimen outside the wind tunnel to capture high contrast images with a white background. For the frontal view, the camera was installed inside the wind tunnel far upstream of the specimens. Consequently, due to the large wind loading on the camera inside the wind tunnel, it was not possible to capture front view images in high velocities.

3.2.2 Theoretical Model

An elastic rod is a three-dimensional slender structure (Audoly and Pomeau, 2010) where its length, L, is much larger than its two other dimensions. Kirchhoff's theory of rods is a classic theory considering finite displacements while assuming small strains (Dill, 1992). The rod is represented by a curve which can deform in three-dimensional space. It can also twist around this curve. The curve is defined as the centerline of the rod which is assumed *inextensible* (Audoly and Pomeau, 2010). It is assumed that each cross section of the rod remains planar and normal to the centerline. Bending moments are proportional to the curvatures, κ_x and κ_y and the twisting moment is proportional to the twist τ. The constitutive relation for a bending and twisting rod made of isotropic material is then written as (Audoly and Pomeau, 2010) :

$$\mathbf{M} = (EI)_y \kappa_y \mathbf{e}_x + (EI)_x \kappa_x \mathbf{e}_y + GJ\tau \mathbf{e}_z \ . \tag{3.4}$$

where $\mathbf{M}$ is the vector of internal moments.

To track the rod twist, a material frame is defined as a moving coordinate system connected to the centerline of the rod following its twist and deformation (Audoly and Pomeau, 2010). Herein, we represent this frame by three unit vectors $\mathbf{e}_i(s)$ for $i = x, y$ and z. Since the material frame moves and twists with the centerline of the rod, s is considered as the distance in the curvilinear or Lagrangian coordinate system along the rod's centerline from its fixed end to its free end. The unit vector $\mathbf{e}_z$ is tangent to the rod's centerline and $\mathbf{e}_x$ and $\mathbf{e}_y$ are principal directions of curvature in the cross sectional plane (Audoly and Pomeau, 2010) as illustrated in Fig. 3.4. Due to the assumption of small strains, the directions of the material frame are considered approximately orthonormal. The set comprising the centerline and the material frame is sometimes called the *Cosserat curve* (Audoly and Pomeau, 2010). The rod is connected to a fixed Eulerian coordinate system which is shown by X, Y and Z with unit vectors $\mathbf{e}_X$, $\mathbf{e}_Y$ and $\mathbf{e}_Z$ as illustrated in Fig. 3.4.

To evaluate the full state of a Kirchhoff rod, the rotation of the material frame around the centerline should be considered. The direction cosines are a representation of the material

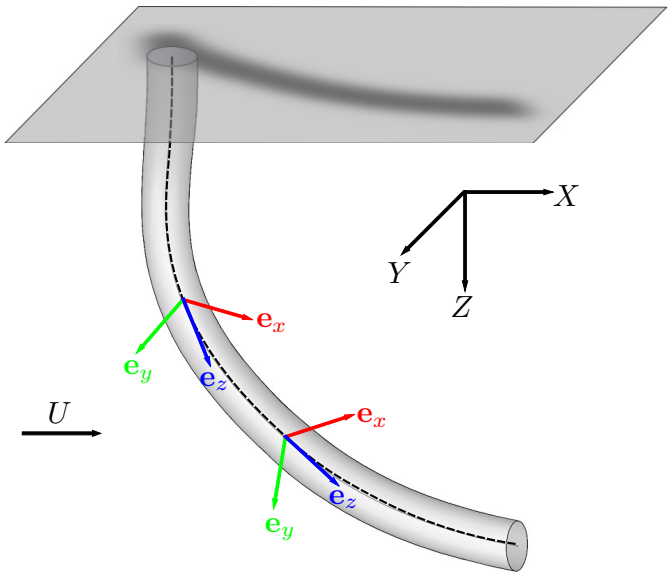

Figure 3.4 Schematic of a rod connected to a fixed coordinate system with moving material frames attached to its centerline.

frame's rotation. They form a transformation matrix $[c(s)]$ relating the material frame to the fixed frame as :

$$\begin{Bmatrix} \mathbf{e}_x \\ \mathbf{e}_y \\ \mathbf{e}_z \end{Bmatrix} = \begin{bmatrix} c_{11} & c_{12} & c_{13} \\ c_{21} & c_{22} & c_{23} \\ c_{31} & c_{32} & c_{33} \end{bmatrix} \begin{Bmatrix} \mathbf{e}_X \\ \mathbf{e}_Y \\ \mathbf{e}_Z \end{Bmatrix} , \tag{3.5}$$

where c_{ij} is a direction cosine (Love, 1944). The three direction cosines of each row of the matrix $[c]$ form a unit vector representing a direction of the material frame (Love, 1944). Consequently, six of the direction cosines are independent and the others can be calculated from these six independent ones. Alternatively to direction cosines, quaternions could have been used (Lazarus *et al.*, 2013). Following the approach explained in detail by Audoly and Pomeau (2010), the spatial derivative of each direction of the material frame with respect to s is defined by :

$$\mathbf{e}'_x(s) = \tau(s)\mathbf{e}_y(s) - \kappa_y(s)\mathbf{e}_z(s) , \tag{3.6a}$$

$$\mathbf{e}'_y(s) = -\tau(s)\mathbf{e}_x(s) + \kappa_x(s)\mathbf{e}_z(s) , \tag{3.6b}$$

$$\mathbf{e}'_z(s) = \kappa_y(s)\mathbf{e}_x(s) - \kappa_x(s)\mathbf{e}_y(s) , \tag{3.6c}$$

where a prime ($'$) denotes a spatial derivative with respect to s. Using this approach, nine first order differential equations, six of which are independent, are derived (refer to Appendix A).

The Kirchhoff equations for the equilibrium of forces and moments in a rod are written as :

$$\mathbf{F}'(s) + \mathbf{p}(s) = 0 \ , \tag{3.7}$$

$$\mathbf{M}'(s) + \mathbf{e}_z(s) \times \mathbf{F}(s) + \mathbf{q}(s) = 0 \ , \tag{3.8}$$

where $\mathbf{p}(s)$ is the vector of external forces per unit length and $\mathbf{q}(s)$ is the vector of external moments per unit length in the three directions of the material frame. $\mathbf{F}(s)$ is the vector of internal forces, namely the shear forces N_x, N_y and the axial tension T, i.e.,

$$\mathbf{F} = N_x\mathbf{e}_x + N_x\mathbf{e}_y + T\mathbf{e}_z \ . \tag{3.9}$$

Finally, by expanding Eqn. (3.7) and Eq. (3.8) and using Eq. (3.6), we obtain six separate differential equations which define the centerline curve of the rod.

The weight of the rod and the fluid loading are considered as external loading. The weight of the rod is calculated as the rod's mass m times the gravitational acceleration g acting in the Z-direction. To evaluate the fluid loading on a deformed rod, we use Taylor's semi-empirical formulation (Taylor, 1952) of the pressure drag force on an oblique cylinder in three-dimensional flow. This method was used successfully in previous reconfiguration studies on bending beams (Gosselin *et al.*, 2010; Luhar and Nepf, 2011). In the method, only the component of the flow velocity normal to the cylinder centerline contributes to the pressure drag force. The normal force on an oblique cylinder is proportional to $sin^2\theta$, where θ is the local angle that the cylinder centerline makes with the flow velocity vector. Without loss of generality, we consider a flow aligned with the X-axis, thus :

$$\cos\theta = \frac{\mathbf{e}_z.\mathbf{e}_X}{|\mathbf{e}_z|\,|\mathbf{e}_X|} = c_{31} \ , \ \sin\theta = \sqrt{1 - c_{31}^2} \ . \tag{3.10}$$

For Reynolds numbers ranging from 10^3 to 10^5, the drag coefficient of a cylinder is nearly constant. Thus, the normal force per unit length on an oblique cylinder is calculated as :

$$p_n = \frac{1}{2}\rho d C_D (U\sin\theta)^2 \ , \tag{3.11}$$

where C_D is the drag coefficient obtained from experiments on rigid circular rods with the same aspect ratio and surface roughness. For the range of the Reynolds number studied, the drag coefficient measured for the rigid test rods is approximately 0.95. Although the fluid model is simple, we expect that the complicated fluid mechanics and turbulence effects are reasonably accounted for by the drag measured on the rigid structure. The drag on a

deformed rod is therefore written in integral form :

$$D = \frac{1}{2}\rho d C_D U^2 \int_0^L \sin^3\left(\theta(s)\right) ds \ . \tag{3.12}$$

A drag coefficient is sufficient to define the fluid loading since the lift and pitching moment coefficients are zero on a circular rod section. Consequently, all external moments in Eq. (3.8) are null. The aerodynamic loading and the gravitational force on the rod are then decomposed into the x-, y- and z-directions of the material frame to obtain the external forces in Eq. (3.7). By expanding Eqns. (3.7) and (3.8) in three directions and introducing the external forces and moments, the Kirchhoff equations are written as :

$$\frac{dN_x}{ds} = N_y\tau - T\kappa_y - p_n.c_{11} - mgL^{-1}.c_{13} \ , \tag{3.13}$$

$$\frac{dN_y}{ds} = T\kappa_x - N_x\tau - p_n.c_{21} - mgL^{-1}.c_{23} \ , \tag{3.14}$$

$$\frac{dT}{ds} = N_x\kappa_y - N_y\kappa_x - mgL^{-1}.c_{33} \ , \tag{3.15}$$

$$\frac{d\kappa_x}{ds} = \frac{1}{(EI)_x}\left[(EI)_y\kappa_y\tau - GJ\kappa_y\tau + N_y\right] \ , \tag{3.16}$$

$$\frac{d\kappa_y}{ds} = \frac{1}{(EI)_y}\left[GJ\kappa_x\tau - (EI)_x\kappa_x\tau - N_x\right] \ , \tag{3.17}$$

$$\frac{d\tau}{ds} = \frac{1}{GJ}\left[(EI)_x\kappa_x\kappa_y - (EI)_y\kappa_x\kappa_y\right] \ . \tag{3.18}$$

To develop dimensionless equations of a deforming rod, the Cauchy number is introduced :

$$C_Y = C_D\frac{\rho U^2 L^3 d}{2(EI)_y} \ . \tag{3.19}$$

The Cauchy Number C_Y represents the ratio of the fluid force to the minimum bending rigidity of the flexible body (Chakrabarti, 2002; de Langre, 2008; Gosselin and de Langre, 2011). The square root of the Cauchy number is similar to the dimensionless velocity (Alben *et al.*, 2002, 2004) or the elastohydrodynamical number (Schouveiler and Boudaoud, 2006) which do not include the drag coefficient in their definition.

The reconfiguration number (Gosselin *et al.*, 2010) and similarly the effective length (Luhar and Nepf, 2011) represent the effect of flexibility on the drag force. The reconfiguration number is defined as the ratio of the drag force of the flexible body to the drag force of an equivalent rigid body :

$$\mathcal{R} = \frac{D}{\frac{1}{2}\rho U^2 C_D dL} \ . \tag{3.20}$$

It is a measure of the drag reduction of a flexible structure due to its flexibility. The Vogel exponent relates the Cauchy number (Eq. (3.19)) to the reconfiguration number (Gosselin *et al.*, 2010) as :

$$\mathcal{R} \propto C_Y{}^{\frac{\vartheta}{2}} \ . \tag{3.21}$$

The bending rigidity ratio, is defined as :

$$\lambda = \frac{(EI)_y}{(EI)_x} \ , \tag{3.22}$$

where $(EI)_y$ and $(EI)_x$ are bending rigidities about the y and x-directions respectively. By definition, we take $(EI)_y < (EI)_x$. The flexible rods therefore have directional rigidity which causes a bending-torsion coupling when transverse loads are not aligned with the x or y axes. Based on the aforementioned directional rigidity, we redefine the twist-to-bend ratio (Eq. (3.2)) as :

$$\eta = \frac{(EI)_y}{GJ} \ . \tag{3.23}$$

The following dimensionless parameters are also required :

$$\bar{s} = s/L \qquad \bar{\kappa_x} = \kappa_x L \qquad \bar{\kappa}_y = \kappa_y L \qquad \bar{\tau} = \tau L \ ,$$
$$\bar{N}_x = \frac{N_x L^2}{(EI)_y} \qquad \bar{N}_y = \frac{N_y L^2}{(EI)_y} \qquad \bar{T} = \frac{T L^2}{(EI)_y} \qquad \mathcal{W} = \frac{mgL^2}{(EI)_y} \ .$$

By applying the external loading in the equations, the deformed shape of the rod's centerline (Eq. (3.13) to (3.18)) can be defined by the following six dimensionless equations :

$$\frac{d\bar{N}_x}{d\bar{s}} = \bar{N}_y\bar{\tau} - \bar{T}\bar{\kappa}_y - C_Y\sqrt{1-c_{31}^2}.c_{11} - \mathcal{W}.c_{13} \ , \tag{3.24}$$
$$\frac{d\bar{N}_y}{d\bar{s}} = \bar{T}\bar{\kappa}_x - \bar{N}_x\bar{\tau} - C_Y\sqrt{1-c_{31}^2}.c_{21} - \mathcal{W}.c_{23} \ , \tag{3.25}$$
$$\frac{d\bar{T}}{d\bar{s}} = \bar{N}_x\bar{\kappa}_y - \bar{N}_y\bar{\kappa}_x - \mathcal{W}.c_{33} \ , \tag{3.26}$$
$$\frac{d\bar{\kappa}_x}{d\bar{s}} = (\lambda - \frac{\lambda}{\eta})\bar{\kappa}_y\bar{\tau} + \lambda\bar{N}_y \ , \tag{3.27}$$
$$\frac{d\bar{\kappa}_y}{d\bar{s}} = (\frac{1}{\eta} - \frac{1}{\lambda})\bar{\kappa}_x\bar{\tau} - \bar{N}_x \ , \tag{3.28}$$
$$\frac{d\bar{\tau}}{d\bar{s}} = (\frac{\eta}{\lambda} - \eta)\bar{\kappa}_x\bar{\kappa}_y \ . \tag{3.29}$$

As previously mentioned, the three direction cosines can be calculated from the six independent ones. Arbitrarily, using Eq. (3.6), the six equations defining the x- and z-directions

of the material frame are considered as the six independent equations. By coupling these six equations with Eqns. (3.24) to (3.29), the full state of a deforming rod can be defined. The set of twelve ordinary differential equations is solved with the `bvp4c` solver of MATLAB. The boundary conditions at the rod's free end ($\bar{s} = 1$) and the rod's fixed end ($\bar{s} = 0$) are :

$$\bar{N}_x(\bar{s}=1) = 0 \ , \qquad \bar{N}_y(\bar{s}=1) = 0 \ , \qquad \bar{T}(\bar{s}=1) = 0 \ ,$$
$$\bar{\kappa}_x(\bar{s}=1) = 0 \ , \qquad \bar{\kappa}_y(\bar{s}=1) = 0 \ , \qquad \bar{\tau}(\bar{s}=1) = 0 \ ,$$
$$c_{11}(\bar{s}=0) = \cos(\alpha_s)\cos(\psi_0) \ , \quad c_{12}(\bar{s}=0) = \cos(\alpha_s)\sin(\psi_0) \ , \quad c_{13}(\bar{s}=0) = -\sin(\alpha_s) \ ,$$
$$c_{31}(\bar{s}=0) = \sin(\alpha_s) \ , \qquad c_{32}(\bar{s}=0) = 0 \ , \qquad c_{33}(\bar{s}=0) = \cos(\alpha_s) \ ,$$

where α_s is the rotation of the clamp due to the imperfect boundary condition evaluated with Eq. (3.3). A continuation method is used to calculate the full state of the rod for a range of Cauchy numbers. In this method, the solver uses an initial guess for all twelve variables of the governing equations for a very small Cauchy number i.e. $C_Y = 0.1$. The solution of this step is then used as the initial guess for the next iteration for a higher Cauchy number. This procedure is repeated until the Cauchy number reaches its specified higher limit i.e. $C_Y = 1000$.

It is expected that the rod undergoes a bifurcation when $\psi_0 = 90°$. However, the developed MATLAB code is unable to predict static instabilities for this angle of incidence because it cannot calculate and follow more than one branch of the solution. Thus, for $\psi_0 = 90°$, a software package AUTO (Doedel and Kernevez, 1986) is used with the same aforementioned governing equations and boundary conditions. This software package has been developed to solve continuation and bifurcation problems. According to the Implicit Function Theorem (Inayat-Hussain *et al.*, 2003), the system of ordinary differential equations presented in Eq. (3.24) to Eq. (3.29), has a stationary solution. In the software, using a successive continuation approach, the governing equations are solved starting from an initial known solution for a range of a continuation parameter values. In the present work, the Cauchy number is considered as the continuation parameter. Bifurcation points are detected by seeking the singularities in the Jacobian of the governing equations where eigenvalues change signs. A cross-comparison for cases with $\psi_0 \neq 90°$ between the MATLAB code and the AUTO solver shows identical results to 7 significant figures.

3.3 Results and Discussion

Three flexible rods made of polyurethane foam (Table 3.2) were tested in the wind tunnel to investigate the effect of bending and torsion on rod drag. In Fig. 3.5, highly contrasted

photographs depict the frontal and side views of specimen R3 in the wind tunnel for three flow velocities and three angles of incidence. In this figure, the thin solid lines represent the shape of an equivalent rod predicted using the mathematical model. The rod undergoes a two-dimensional bending or *in-plane* deformation for $\psi_0 = 0°$. In this condition, the rod's material frame with the minimum bending rigidity $(EI)_y$ is aligned with the flow therefore the reconfiguration is in pure bending. The magnitude of deformation increases with increasing flow velocity. For a non-zero angle of incidence, e.g. $\psi_0 = 45°$, where the rod's material frame is not aligned with the flow, the magnitude of the in-plane deformation is smaller compared to the case $\psi_0 = 0°$. This is due to the increasing contribution of the reinforcement fibers to the bending rigidity leading to less deformation. However, for non-zero angles of incidence, because of asymmetric bending, the rod undergoes a three-dimensional deformation showing both in-plane and *out-of-plane* deformation. This out-of-plane deformation creates a moment arm about the rod's root which twists the rod to realign it with the flow. For $\psi_0 = 90°$, the rod's material frame is aligned with the flow but with the maximum bending rigidity $(EI)_x$. Because of symmetry, the rod does not show an out-of-plane deformation at 10 ms^{-1}. Compared with $\psi_0 = 0°$, at $\psi_0 = 90°$ the deformation is smaller. At $\psi_0 = 90°$, for larger flow velocities ($U = 20,\ 30\ \text{ms}^{-1}$), the symmetry is broken and significant out-of-plane deformation is observed. In this case, the rod undergoes a supercritical and static pitchfork bifurcation which is discussed below. The difference between the experimental and mathematical results is mainly due to imperfect boundary conditions in the experiments.

Figure 3.6a shows the variation of the X-component displacement (X_{tip}) of the tip of specimen R3 with increasing flow velocity for different angles of incidence. Experimental data points extracted from photographs are also presented with markers for reference. To visualize the out-of-plane deformation, the camera had to be placed inside the wind tunnel. Therefore, there are no experimental data points for flow velocities higher that 30 ms^{-1} due to technical limitations in taking photographs. For all incidence angles, the X-component of the tip increases with flow velocity. However, the rate of increase of X_{tip} becomes considerably small for high velocities therefore X_{tip} asymptotically approaches a constant value. It is also seen that by increasing the angle of incidence, the magnitude of the in-plane deformation decreases. This is due to the increasing bending rigidity with the angle of incidence. Figure 3.6b shows the out-of-plane deformation of specimen R3 by providing the variation of the tip's Y-component displacement (Y_{tip}) with velocity. For $\psi_0 = 0°$ the rod does not have an out-of-plane deformation, thus $Y_{tip} = 0$. For $\psi_0 = 30°,\ 45°$ and $60°$, Y_{tip} variation shows an initial increase in the out-of-plane deformation. However, the experimental results and the mathematical predictions show that Y_{tip} starts to decrease as the rod twists back and becomes more aligned with the flow. For $\psi_0 = 90°$, Y_{tip} is zero prior to a critical velocity of

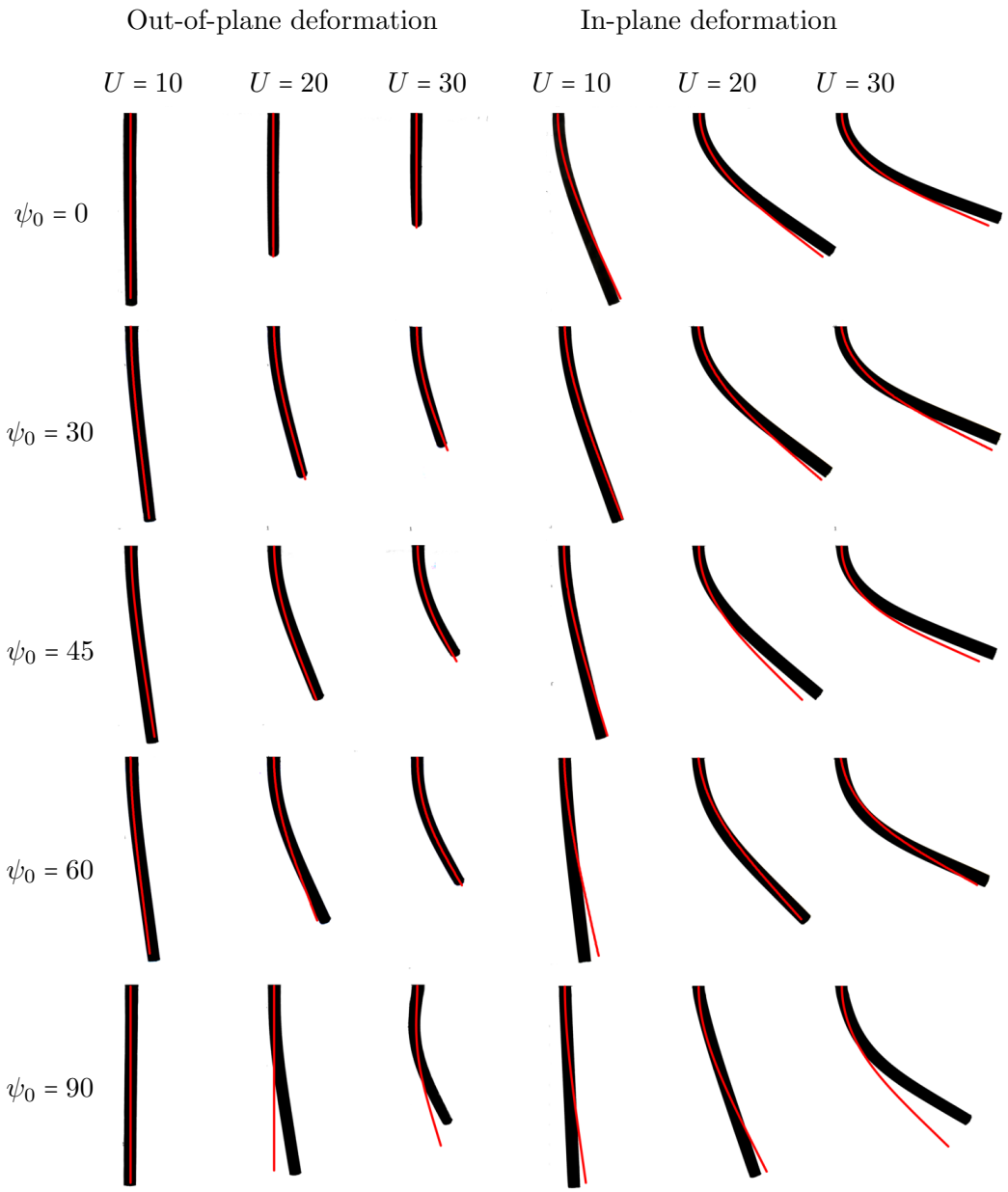

Figure 3.5 Photographs of deformed shapes of the specimen R3. Thin lines represent the deformation of an equivalent rod predicted by the mathematical model. The velocity unit is ms^{-1}.

approximately 26 ms^{-1}, thus the rod does not undergo an out-of-plane deformation below this velocity. Beyond the critical velocity, Y_{tip} undergoes a jump to a maximum or minimum value approximately ±31 mm exhibiting a pitchfork bifurcation. Y_{tip} then decreases with flow velocity showing the rod becoming aligned with the flow. Prior to the bifurcation point, the symmetric bending of the rod is stable but beyond that point, the rod loses its stability and jumps to a stable branch to either sides showing a sudden out-of-plane deformation. The

post-bifurcation displacement is triggered by an infinitesimal out-of-plane deformation along with the resulting moment arm about the root. This moment arm twists sections of the rod to an angle of incidence smaller than 90, inducing a larger out-of-plane deformation. The larger out-of-plane deformation amplifies the moment arm and this interaction continues until the rod finds a new three-dimensional equilibrium state. Similarly to Fig. 3.5, for $\psi_0 = 90°$, the experimental and mathematical results are not in exact agreement due to imperfect boundary conditions in the experiments which advances the bifurcation.

Figure 3.7 presents the variation of the measured drag of the specimen R3 with increasing flow velocity for a range of angles of incidence. The measured drag for an equivalent rigid structure is also shown for reference. The drag on the rod increases with the flow velocity as well as the angle of incidence. For low flow velocities, the drag on the flexible rod is similar to the drag force on an equivalent rigid structure following the U^2 scaling curve. However, with increasing flow velocity, the drag force on the flexible rod increases in a less pronounced way than the equivalent rigid bar. This divergence from the U^2 scaling results from the increase in the static deformation. The divergence is delayed by increasing the angle of incidence. Thus, the drag on the flexible rod increases monotonically with the angle of incidence because of the increasing contribution of fibers to the rod rigidity.

The twisting moment at the root (M_Z), simply referred to as the torque hereafter, is a direct indicator of the magnitude of torsional reconfiguration. The torque is measured directly by the force transducer as the twisting moment about the Z-axis. Figure 3.8 shows the variation of the torque with flow velocity for a range of angles of incidence for R3. For $\psi_0 = 0°$, the torque is null because there is no out-of-plane deformation to create a moment arm. For a non-zero angle of incidence, the torque remains approximately zero for low flow velocities since the rod does not deform significantly to create a moment arm. For U greater than approximately 10 ms^{-1}, the deformation of the rod creates a moment arm. The torque increases with increasing flow velocity as well as angle of incidence. This is due to the combined increase in the moment arm and fluid loading. The reinforced rods under study make it possible to control the amount of twisting reconfiguration by varying the angle of incidence.

In Fig. 3.8, the calculated torque for a rod equivalent to specimen R3 at the same angles is presented. The mathematical model shows a good agreement with the experiments for $\psi_0 < 90°$. However, for $\psi_0 = 90°$, the mathematical model is shifted as compared to the experimental data points. The mathematical model predicts that prior to a critical flow velocity of $U \approx 27$ ms^{-1} the torque is null due to symmetric bending. Beyond this critical flow velocity, the symmetry is broken due to the rod undergoing a pitchfork bifurcation. The difference between the experimental and mathematical results for $\psi_0 = 90°$ is likely due

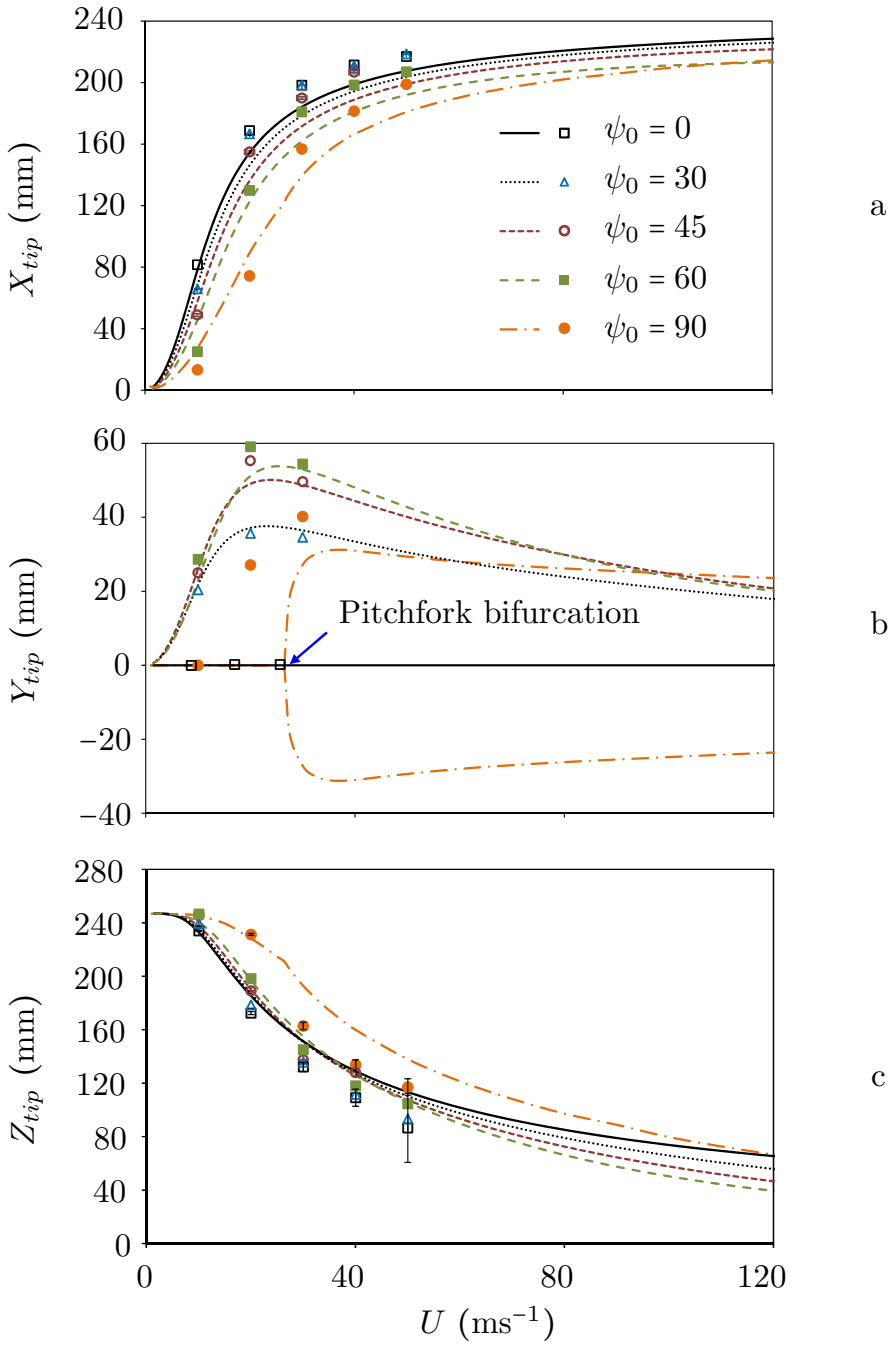

Figure 3.6 Mathematical evaluation of the in-plane and out-of-plane deformation of specimen R3 for three angles of incidence by showing a) the variation of the tip's X-component, b) the tip's Y-component and c) the tip's Z-component with flow velocity. Some experimental data points are provided for reference as markers. Error bars represent the standard deviation of the time fluctuations of the tip position.

to imperfect symmetry in the experiments which causes early bifurcation. This imperfect symmetry may be caused by an error in the angle of incidence, imperfect clamped boundary

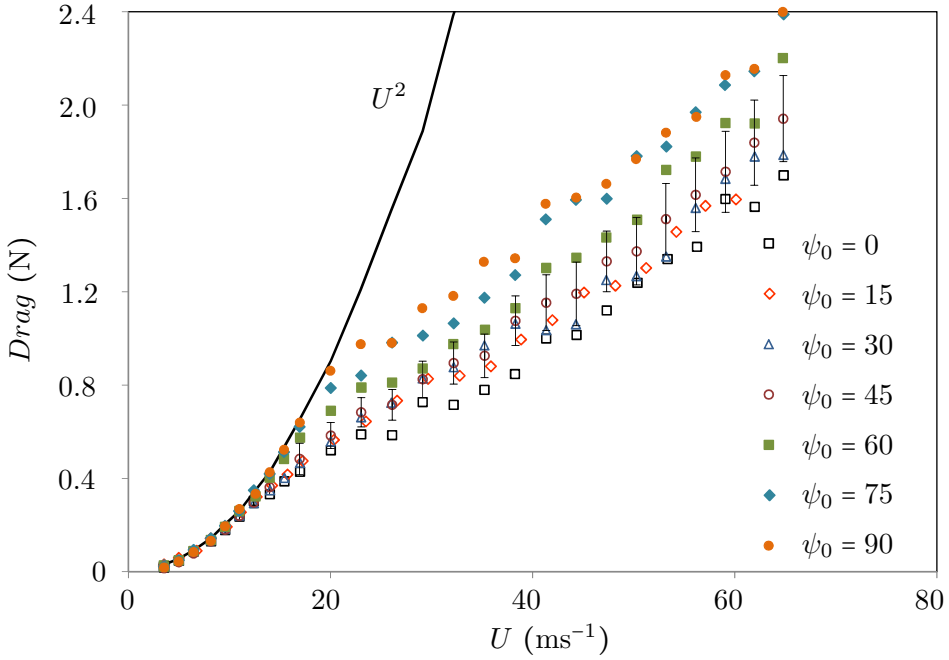

Figure 3.7 Time-averaged drag of the specimen R3 for a range of ψ_0 from 0° to 90°. Drag loading on an equivalent rigid rod is provided as a line for reference. Error bars represent the standard deviation of the time fluctuations for series $\psi_0 = 45°$. Time fluctuations are similar for other series.

condition, heterogeneous mass distribution or a slight natural curvature in the rods. Figure 3.8 shows that there is a limiting behavior which leads to a bifurcation at $\psi_0 = 90°$. Moreover, the mathematical result for $\psi_0 = 85°$ represents a better agreement with the experimental results for $\psi_0 = 90°$. This suggests that the combined effect of the aforementioned factors particularly the angle of incidence may lead to a large imperfection responsible for the inconsistency between the numerical and experimental results for $\psi_0 = 90°$.

3.3.1 Dimensionless Representation

The system of equations (3.24) to (3.29) representing the arbitrary large deformation of a rod is rendered dimensionless by introducing the Cauchy number in Eq. (3.19). From the experimental drag measurements, the variation of the reconfiguration number of the specimens R3 with increasing Cauchy number is presented in Fig. 3.9 for a range of ψ_0 from 0° to 90° degrees. By definition, the dimensionless drag scaling of a rigid bar is presented with a horizontal line at $\mathcal{R} = 1$ in this figure. It is seen that for small Cauchy numbers the reconfiguration number is approximately 1 which means that the drag force on the flexible rod is close to that acting on an equivalent rigid bar. Between $C_Y \approx 3$ and 20, depending

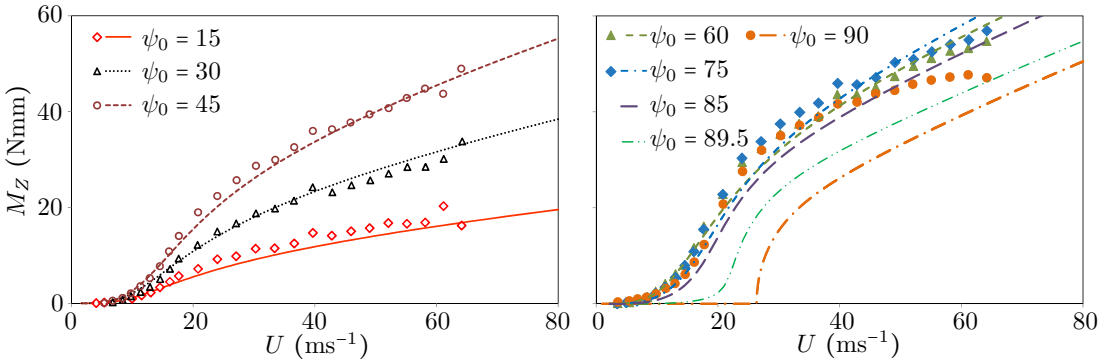

Figure 3.8 Twisting moment at the root of the specimen R3 varying by the flow velocity and angle of incidence. The mathematical evaluation of the root's twisting moment is provided as lines for reference.

on the angle of incidence, the reconfiguration number starts to diverge from that of the equivalent rigid bar and decreases with increasing Cauchy number. This divergence is delayed by increasing the angle of incidence due to the increasing contribution of the fibers in the bending rigidity against the flow.

The variation of $\mathcal{R}$ with C_Y calculated with the mathematical model is presented as lines in Fig. 3.9 for three angles of incidence. The reconfiguration number is 1 for small Cauchy numbers but it diverges from $\mathcal{R} = 1$ for Cauchy numbers greater than unity. Similarly to the experimental measurements, the reconfiguration number decreases with the Cauchy number and increases with increasing angle of incidence. All experimental drag measurements in dimensionless form are found to fall between the two limiting mathematical curves for $\psi_0 = 0°$ and $\psi_0 = 90°$.

For Cauchy numbers greater than 100, the experimental data points for each angle of incidence can be fitted with a power law which appears as a straight line on the $\mathcal{R}-C_Y$ log-log plot. The slope of this line is the exponent of the power law. According to Eq. (3.21), the Vogel exponent is twice this slope. In Fig. 3.9, the slope of −0.33, equivalent to $\vartheta = -0.66$ expected for pure bending (Alben *et al.*, 2002, 2004; Gosselin *et al.*, 2010), is provided for reference. Table 3.3 presents the Vogel exponents calculated from the experimental data points for specimen R3 for different angles of incidence and $C_Y > 100$. The Vogel exponent is found to vary from −0.62 to −0.86 and the average coefficient of determination for the fitted data is 0.85. With the mathematical model, the predicted Vogel exponent does not change significantly with the variation of angle of incidence. It remains approximately −0.7 for any angle of incidence and very high Cauchy numbers. However, in the experiments the predicted mathematical Vogel exponent is not reached for all angles of incidence because for higher angles, the maximum

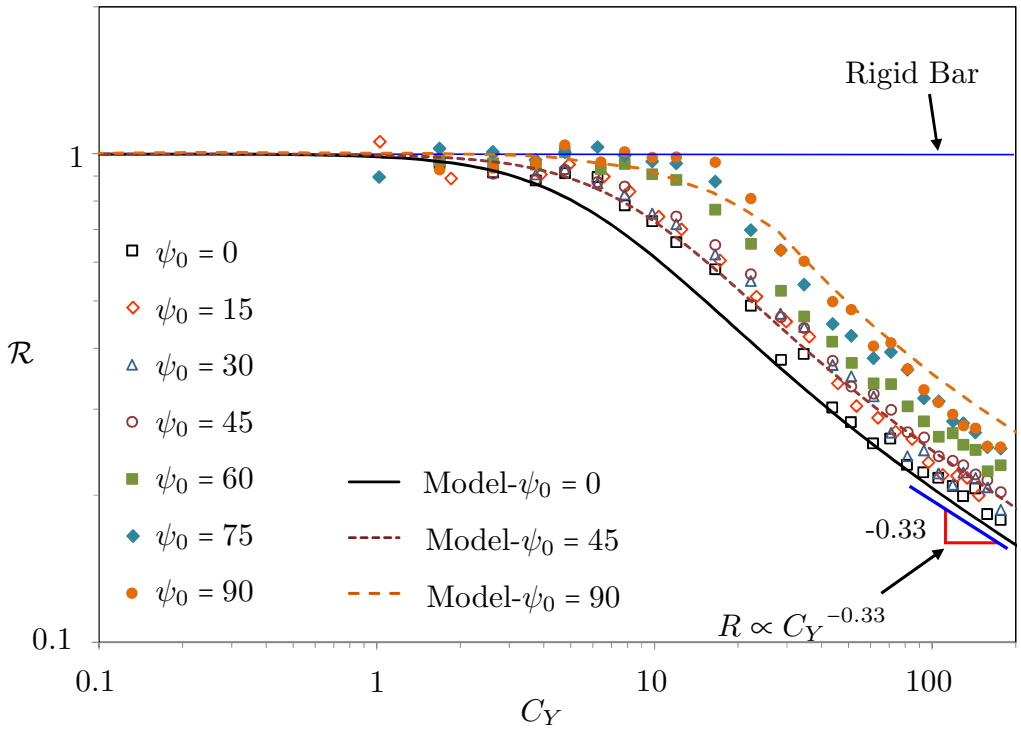

Figure 3.9 Experimental drag scaling of the specimen R3 represented by the Cauchy number and the reconfiguration number. The equivalent mathematical model for $\psi_0 = 0°$, 45° and 90° is provided as lines.

Cauchy number attainable in the wind tunnel is not sufficient to align the rod with the flow. The small difference between the predicted Vogel exponent in our mathematical model and that of previous studies in pure bending is due to the non-negligible weight of the rod in the present model (see Luhar and Nepf (2011)).

The torsion of a rod alters its effective bending rigidity in the flow direction for non-zero angles of incidence. The choice of $(EI)_y$ is therefore not representative when computing the Cauchy number (Eq. (3.19)) for a non-zero angle of incidence. An alternative is proposed in

Table 3.3 The Vogel exponent for a range of angle of incidence calculated from the experimental data points and the mathematical simulation of R3

ψ_0	0°	15°	30°	45°	60°	75°	90°
ϑ (Exp. $C_Y > 100$)	−0.70	−0.62	−0.66	−0.66	−0.68	−0.86	−0.86
ϑ (Math. $100 < C_Y < 300$)	−0.76	−0.76	−0.76	−0.76	−0.74	−0.74	−0.76
ϑ (Math. $300 < C_Y < 500$)	−0.72	−0.72	−0.72	−0.72	−0.70	−0.68	−0.68
ϑ (Math. $500 < C_Y < 1000$)	−0.7	−0.72	−0.72	−0.72	−0.70	−0.68	−0.68
Exp. Coeff. of Determination	0.88	0.85	0.76	0.97	0.82	0.94	0.95

the following which considers the effect of torsion on the bending rigidity and the Cauchy number.

3.3.2 Equivalent Bending Rigidity

We seek a modification to the Cauchy number to account for the effective bending rigidity which lies somewhere between $(EI)_x$ and $(EI)_y$. This effective rigidity depends on the angle the material frame makes with the flow, thus it depends on the incidence angle ψ_0 and the torsional rigidity. A dimensionless representation is proposed in the following which considers the effect of the angle of incidence and the rigidity ratios (λ and η) on the equivalent bending rigidity and the Cauchy number.

The rigidity of a flexible rod comes from a contribution of the foam matrix and reinforcement fibers :

$$(EI)_{eq} = (EI)_{matrix} + (EI)_{fiber} \ . \tag{3.30}$$

For the configuration shown in Fig. 3.3, in the undeformed case and based on the parallel axis theorem, the equivalent bending rigidity is written as :

$$(EI)_{eq} = (EI)_{matrix} + E_f \sum_{1}^{n_f} I_{f,0} + A_f (r \sin\psi_0)^2 \ . \tag{3.31}$$

where r is the radial distance of each fiber from the rod's centerline, A_f is the fiber sectional area, n_f is the number of fibers and $I_{f,0}$ is the second moment of area of each fiber around its neutral axis. Since the fibers are very thin relative to the rods, $E_f I_{f,0}$ is negligible. Therefore the bending rigidity around the two directions of the material frame can be approximated as :

$$(EI)_y \approx (EI)_{matrix} \ , \tag{3.32}$$

$$(EI)_x \approx (EI)_{matrix} + E_f \sum_{1}^{n_f} A_f r^2 \ . \tag{3.33}$$

By subtracting Eq. (3.32) from Eq. (3.33) and introducing the result into Eq. (3.31), the equivalent bending rigidity can be written as :

$$(EI)_{eq} = (EI)_y + [(EI)_x - (EI)_y] \sin^2\psi_0 \ , \tag{3.34}$$

where $[(EI)_x - (EI)_y] \sin^2\psi_0$ is the contribution of the reinforcement fibers in the equivalent bending rigidity. This could be an improved definition of the bending rigidity to construct the Cauchy number. However, according to Eq. (3.18) the reinforced rod twists proportionally

to :

$$\zeta = \frac{(EI)_x - (EI)_y}{GJ} = \frac{\eta}{\lambda}(1-\lambda) \ . \tag{3.35}$$

As a result, the equivalent bending rigidity of the rod varies with the twist angle. When the rod bends in the flow, it also reorients to bend in its most flexible direction by aligning the x-direction of the material frame with the flow. Therefore the angle of incidence at each section of the rod may become smaller than the initial angle of incidence ψ_0. This decreases the contribution of the reinforcement fibers in the bending rigidity and consequently reduces the overall bending rigidity of the rod. We therefore propose the following ansatz for an improved equivalent bending rigidity definition :

$$(EI)_{eq} = (EI)_y + \frac{[(EI)_x - (EI)_y]\sin^2\psi_0}{1+\zeta^\beta} \ , \tag{3.36}$$

where $\beta > 0$ is an exponent to be defined. In Eq. (3.36), the bending-torsion coupling parameter ζ varies the contribution of the reinforcement fibers in the equivalent bending rigidity. If $\zeta \ll 1$, the rod is rigid in torsion and the correction found in Eq. (3.34) holds. If $\zeta \gg 1$, the rod twists freely, it reorients under the slightest load to bend in its most flexible direction and $(EI)_{eq} \approx (EI)_y$. Assuming small deformations, the curvatures κ_x and κ_y are approximated as :

$$\kappa_x = \frac{d^2\left(w_{eq}\sin\psi_0\right)}{ds^2} \ , \tag{3.37}$$

$$\kappa_y = \frac{d^2\left(w_{eq}\cos\psi_0\right)}{ds^2} \ , \tag{3.38}$$

where w_{eq} is the deformation in the flow direction due to a uniform pressure. This deformation is calculated from linear Euler-Bernoulli beam theory as :

$$w_{eq} = \frac{p_n s^2[6L^2 - 4Ls + s^2]}{24(EI)_{eq}} \ . \tag{3.39}$$

The equivalent bending rigidity is a bulk property. By substituting Eq. (3.37), (3.38) and (3.39) in Eq. (3.18) and rewriting it in integral form, we obtain the average twist :

$$\begin{aligned}\tau_{avg} &= \frac{1}{2}\zeta\sin(2\psi_0)\int_0^L\left(\frac{d^2w_{eq}}{ds^2}\right)^2 ds \\ &= \frac{{p_n}^2}{40}L^5\sin(2\psi_0)\frac{\zeta}{\left[(EI)_{eq}\right]^2} \ ,\end{aligned} \tag{3.40}$$

Equation (3.40) shows that for a given load, the average twist remains constant if $(EI)_{eq} \propto$

$\zeta^{1/2}$ which leads us to choose $\beta = 1/2$. An *equivalent Cauchy number* is then defined as :

$$C_Y^* = C_D \frac{\rho U^2 L^3 d}{2(EI)_{eq}} \ , \tag{3.41}$$

The variation of $\mathcal{R}$ with C_Y (Eq. (3.19)) for the three flexible rods (Table 3.2) and for a range of angle of incidence from 0 to 90 is presented in Fig. 3.10a. As seen in the figure, the reconfiguration number is approximately 1 for all three specimens for small Cauchy numbers, which means that the drag is close to that of the equivalent rigid bar. Starting from mid-range Cauchy numbers between $C_Y \approx 5$ and 20, the reconfiguration number decreases with increasing Cauchy number. The maximum reachable Cauchy number is less than 100 for the rods R1 and R2 due to the limitation of the test equipment. The slope of the log-log plot is therefore less than -0.33 for these two specimens. The variation of $\mathcal{R}$ with C_Y using the mathematical model is presented as lines for R3 in Fig. 3.10a. It is found that all the experimental drag measurements fall between the two limiting curves for $\psi_0 = 0°$ and 90°. However, the measurements for the three specimens do not collapse on a single curve.

Figure 3.10b presents the dimensionless drag measurements for all three specimens obtained using the equivalent Cauchy number (Eq. (3.41)) for the range of angles of incidence from 0 to 90. The results show that the reconfiguration number is approximately 1 for small equivalent Cauchy numbers and starts to diverge from $\mathcal{R} = 1$ near $C_Y^* \approx 2$ to 8. It decreases

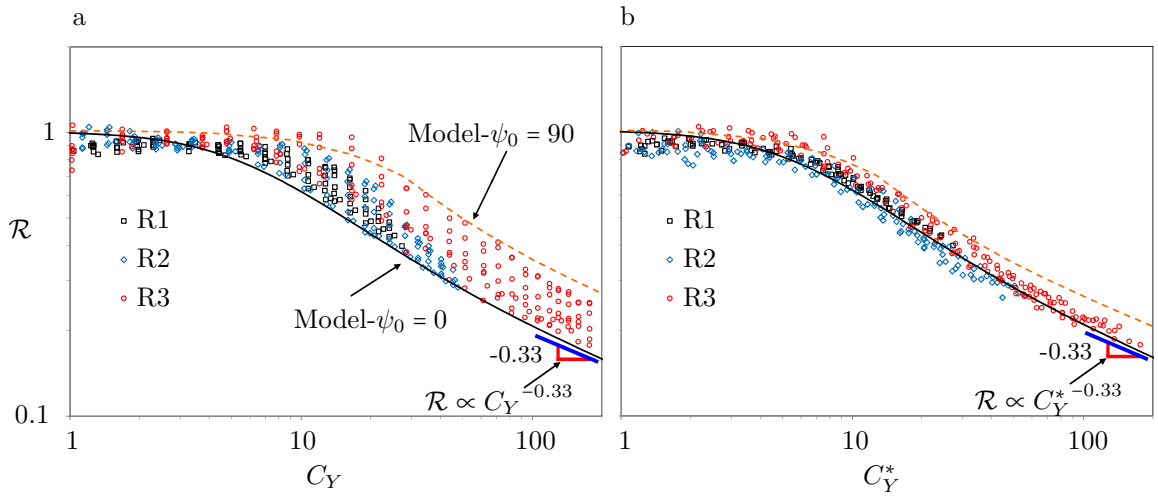

Figure 3.10 The reconfiguration number of the three specimens (table 3.2) for a range of ψ between 0° and 90° plotted versus a) the Cauchy number and b) the equivalent Cauchy number to find a generic representation of the drag scaling. The Mathematical models for $\psi_0 = 0°$ and $\psi_0 = 90°$ are presented as lines.

with increasing equivalent Cauchy number and a constant power law exponent is reached for large equivalent Cauchy numbers. In the figure, the $\mathcal{R} - C_Y^*$ plots of the mathematical model for specimen R3 for $\psi_0 = 0°$ and 90° are presented for reference. As shown, all experimental results effectively collapse onto a single curve regardless of test conditions. The single curve, representing the two-dimensional bending deformation for $\psi_0 = 0°$, can quantify the drag scaling of bending and twisting rods independently of their geometry, material properties and angle of incidence. This means that using the right set of dimensionless numbers ($\mathcal{R}$ and C_Y^*), the three-dimensional reconfiguration of a rod and the bending deformation of a beam are similar, both governed by a single parameter (C_Y^*). In this representation, the Vogel exponent of a bending-twisting rod approaches the Vogel exponent of the two-dimensional bending case, −0.66.

To have a better understanding of the torsion of the rod along its length, the variation of the dimensionless twist ($\bar{\tau}$) along the dimensionless length of the rod is studied using the mathematical model. The dimensionless twist represents the variation of the sectional angle of incidence. Figure 3.11 shows the variation of the dimensionless twist for specimen R3 along its length for small to very high equivalent Cauchy numbers and two angles of incidence. This figure is an illustration of the magnitude of torsion at each section of the rod. By definition, the area under each curve in Fig. 3.11 gives the total twist angle of the rod's tip relative to its root.

The figure shows that most of the torsion occurs close to the fixed end of the rod. In addition, as the equivalent Cauchy number increases, the generated torsion also increases close to the fixed end. The reason being that as the Cauchy number increases, sections of the rod far from the fixed end become aligned with the flow. As a result, no significant moment arm is created about these sections. At the same time, this aligned part of the rod acts as a moment arm for the sections close to the fixed end. As the equivalent Cauchy number increases, more sections become aligned with the flow increasing the torsion near the fixed end. In general, $\bar{\tau}$ at the rod's root increases with the equivalent Cauchy number due to increasing fluid loading and out-of-plane deformation. For $\psi_0 = 45°$, the maximum dimensionless twist is found at the fixed end of rod. However, for $\psi_0 = 90°$, the location with the maximum torsion is found within the first quarter of the rod; the maximum torsion location then moves towards to the fixed end as the equivalent Cauchy number increases. The reason is probably due to the non-uniform out-of-plane deformation of the rod for $\psi_0 = 90°$ (see for instance Fig. 3.5). As seen in Fig. 3.5, generally the rod has an out-of-plane deformation towards the right side. However, for $\psi_0 = 90°$ and $U = 30\ ms^{-1}$ ($\approx C_Y^* = 30$), the rod deforms to the left up to a certain point along its length and beyond this point, it twists and bends to the right. Thus, for $\psi_0 = 90°$, $\bar{\tau}_{max}$ is found close to this turning point rather than the root. This also explains

the reduction of the torque for $\psi_0 = 90°$ compared to the smaller angles in Fig. 3.8 since the torque at the root in $\psi_0 = 90°$, is not the maximum twisting moment along its length.

To better understand the rod's twist, the following torsion length (ℓ) is proposed :

$$\ell = \frac{GJ\psi_0}{M_z L} \ , \tag{3.42}$$

where ψ_0 is in radians. The torsion length ℓ is the dimensionless length the rod would need to twist by an angle ψ_0 under the torque M_z measured at its root. Figure 3.12 shows the variation of the torsion length of specimen R3 with increasing equivalent Cauchy number on a logarithmic scale. For small C_Y, the torsion length is large and thus the rod does not twist to align itself with the flow. With increasing equivalent Cauchy number, the torsion length decreases, corresponding to an increase in torsion. As C_Y is increased further, ℓ becomes smaller than unity. The rod can thus align its most flexible direction with the flow and the torsion increases and becomes more localized at the root. This is due to the increasing out-of-plane deformation and moment arm magnitude which lead to a larger torque. Once the rod is twisted and aligned with the flow, the rod shows a reconfiguration similar to a bending beam. For $\psi_0 = 90°$, the torsion length is infinite prior to the bifurcation because the deformation is symmetric, but the torsion length decreases suddenly beyond a critical equivalent Cauchy number. Once the bifurcation occurs, a moment arm is created which leads to a larger torque and smaller torsion length. As seen in Fig. 3.12, in the asymptotic regime of large deformation, the torsion length scales as $\ell \propto {C_Y^*}^{-0.33}$. This is interesting because as we observed in Fig. 3.10, the same scaling emerges for $\mathcal{R}$ as a function of C_Y^*.

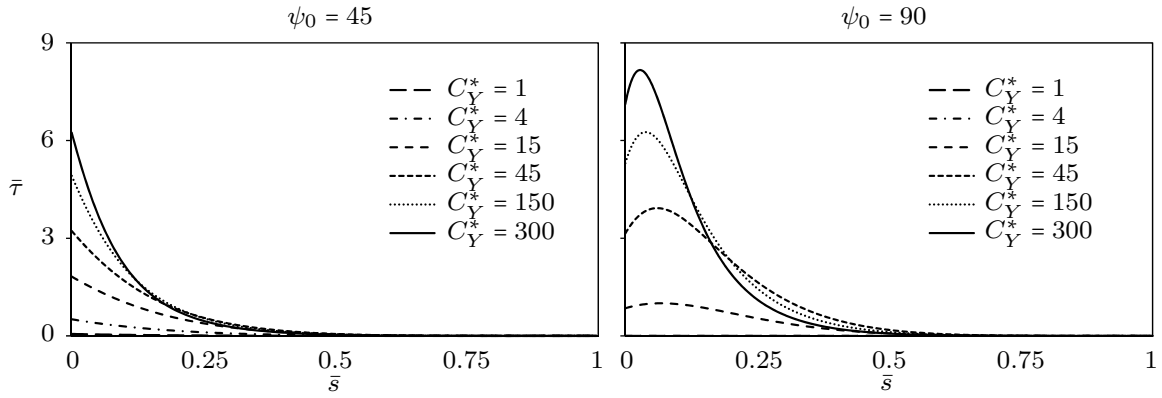

Figure 3.11 Mathematical demonstration of torsion of R3 along its length by plotting the variation of $\bar{\tau}$ with $\bar{s}$, C_Y^* and ψ_0.

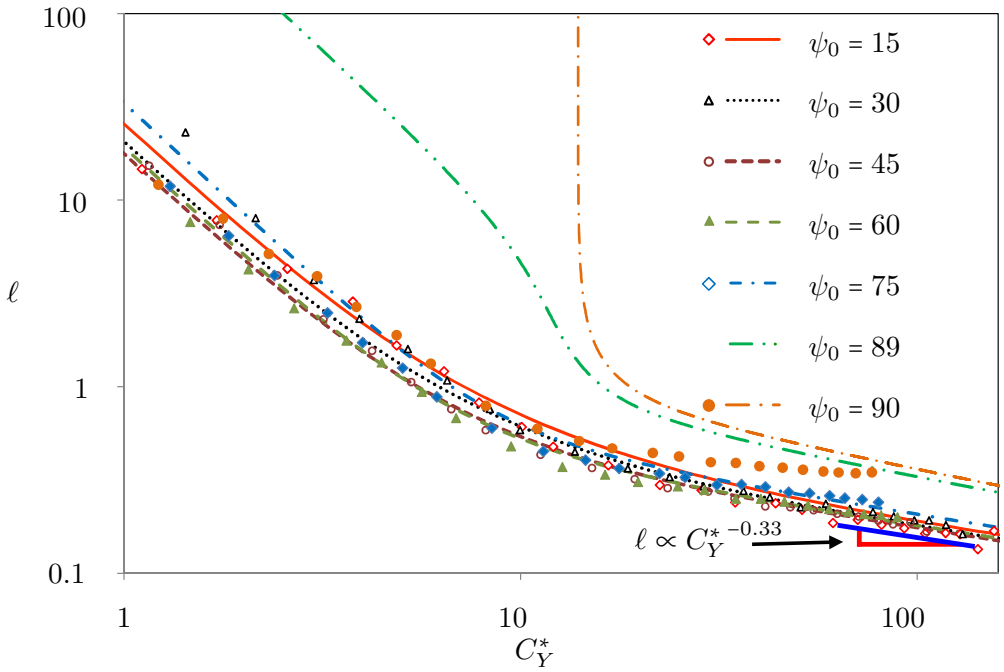

Figure 3.12 Experimental evaluation of the torsion length of specimen R3 varying with the equivalent Cauchy number. The mathematical model is provided as lines for comparison.

3.4 Conclusion

The three-dimensional reconfiguration of plants was studied using flexible rods with structural anisotropy. The work aims to answer the following question : What is the effect of torsion on reconfiguration ? It was shown that reinforcing the flexible rods in one direction leads to coupling between torsional and bending deformation. This allowed us to benefit from the simplicity of circular rods while being able to alter the bend-twist coupling. As observed in the experiments, the drag scaling of a flexible rod diverges from a U^2 relation with increasing magnitude of deformation.

It was shown that the direction of reinforcement with respect to the flow (ψ_0) is a key parameter in the effective bending rigidity of the rod. Based on this parameter, the definition of the Cauchy number was modified by introducing an equivalent bending rigidity. It was concluded that the equivalent Cauchy number and the reconfiguration number effectively characterize the three-dimensional reconfiguration of the rod as a beam undergoing a two-dimensional bending.

The Vogel exponent of the reconfiguring rod approaches −0.7 which is the exponent of bending beams and plates considering their weight. This shows that the three-dimensional reconfiguration of the rod becomes approximately two-dimensional in the regime of very large

deformations. It is concluded that in the large deformation regime, torsion has no effect on the Vogel exponent since the exponent was found to be independent of the angle of incidence.

A mathematical model was developed by coupling the Kirchhoff theory of rods with a semi-empirical drag formulation. The model predicted that the Vogel exponent reaches -0.7 for high Cauchy numbers independently of the angle of incidence, the rod's material and geometrical characteristics. A pitchfork bifurcation was also predicted for $\psi_0 = 90°$. However, due to imperfect symmetry and flow perturbations in the experiments, the mathematical model overestimated the critical velocity at which bifurcation occurs. It would be interesting to evaluate and implement the imperfection of the boundary conditions to obtain a better prediction of the bifurcation.

While this paper focused on the effect of torsion on the reconfiguration of flexible rods, studying the three-dimensional reconfiguration of slender lifting surfaces might be of interest. In addition, the present work considers a rod which is initially undeformed. It would be of interest to study the reconfiguration of a rod with a pre-twisted material frame along its length. This case can be found in the structure of many plants with chiral morphology.

Acknowledgment

The authors are thankful to Benedict Besner and Nour Aimene for their technical support and Michael Plante, Diego Altamirano, Pablo Maceira-Elvira and Anthony Salze for their work on preliminary versions of the experimental setup. The financial support of the Natural Sciences and Engineering Research Council of Canada is acknowledged.

CHAPTER 4 ARTICLE 2 : BENDING AND TORSIONAL RECONFIGURATION OF CHIRAL RODS UNDER WIND AND GRAVITY

M. Hassani, S. Molgat Laurin, N. W. Mureithi and F. P. Gosselin, 2017, published in the journal of *Extreme Mechanics Letters*.

Abstract

We seek to understand the effect of chirality on the reconfiguration and the self-buckling strength of chiral plants subjected to wind and gravity by experimental and theoretical modeling of their large deformation. Chiral rod and ribbon specimens are made of polyurethane foam reinforced with nylon fibers and ABS plastic. Wind tunnel tests are performed to evaluate the effect of chirality on flow-induced reconfiguration. A theoretical model is developed by coupling the Kirchhoff rod theory with a semi-empirical formulation for aerodynamic loading evaluation. A range of geometrical, material and flow parameters are studied in the experimental and theoretical model. It is shown that for rods, chirality decreases the maximum root bending moment. For ribbons, chirality leads to a trade-off with higher self-buckling strength but also higher root bending moment. Moreover, chirality reduces the effect of the loading direction on deformation. Chirality plays an important structural role in the interaction of slender structures with fluid flow and gravity loading.

4.1 Introduction

In general, plants and vegetation are flexible and are prone to significant deformation under fluid loading, their own weight or precipitation load. The deformation of plants which usually leads to a drag reduction, is termed reconfiguration (Vogel, 1989). The reconfiguration of plants has been studied fundamentally by modeling them as simple mechanical structures such as bending beams (Luhar and Nepf, 2011), fibers (Alben *et al.*, 2002, 2004) and plates (Gosselin *et al.*, 2010; Gosselin and de Langre, 2011; Schouveiler and Boudaoud, 2006). Although these aforementioned models can simplify the two-dimensional deformation of plants, they are not representative for all forms of reconfiguration. For instance, many plants grow with a chiral morphology which cannot be modeled by a simple bending beam.

Chirality can be found in many biological and artificial structures, from DNA and several types of plants (Zhao *et al.*, 2015) to some polymers (Ye *et al.*, 2010) and nano-materials (Chen *et al.*, 2005; Zhao *et al.*, 2014). Many aquatic plants such as cattail, threeleaf arrowhead,

sweet flag, bur-reed (Zhao *et al.*, 2015) and terrestrial plants such as daffodil and pancratium possess chiral leaves or stems (Schulgasser and Witztum, 2004). In general, the evolutionary aspect of chirality in biological structures has been discussed in many studies. For instance, it is of great interest to know whether the chiral morphology of DNA was a requirement or an outcome of evolution (Lunine *et al.*, 1999). Moreover, it has been claimed in some studies that erect plants with chiral morphology are less vulnerable to distributed transverse loading and Euler buckling (Zhao *et al.*, 2015; Schulgasser and Witztum, 2004; Rowlatt and Morshead, 1992). The latter may be evidence of adaptation of this type of plants to their environment through a long evolution process.

Chiral structures have been studied mathematically using different theories such as Timoshenko pre-twisted beams (Zhao *et al.*, 2015; Schulgasser and Witztum, 2004), Kirchhoff rods (Zhao *et al.*, 2014; Goriely and Shipman, 2000; Wang *et al.*, 2012), and Cosserat rods (Wang *et al.*, 2014). However, the mathematical study of the large deformation of chiral plants bending and twisting in flow is missing from the literature. Therefore, the goal of this work is to study the reconfiguration mechanisms of chiral plants subjected to wind and gravity through a combination of chiral rod simulations and wind tunnel experiments. We seek to understand the effect of chirality on the ability of plants to withstand the fluid loading and their own weight.

4.2 Methodology

4.2.1 Experimental Procedure and Materials

The tests on flexible specimens with chiral morphology were performed in a wind tunnel located at École Nationale d'Aérotechnique (Saint-Hubert, QC, Canada). The wind tunnel has a square test section of 60×60 cm^2 and can produce a maximum air speed of 38 ms^{-1}. As detailed in (Hassani *et al.*, 2016), a six-axis force transducer (ATI GAMMA, ATI Industrial Automation, Apex, North Carolina) was used in the present experiments to measures the aerodynamic forces and moments in three orthogonal directions. It can measure transverse forces, axial forces and moments up to 32 N, 100 N and 2.5 Nm, respectively. The resolution of the force transducer is 6.25×10^{-3} N and 12.5×10^{-3} N for the transverse and axial loading and 0.5×10^{-3} Nm for moments. The force transducer was fixed to the top of the wind tunnel test section. The specimens were clamped to the force balance at one end using a mast to subtract the effect of boundary layer on the tunnel wall from the measurements. In each test, the root incidence angle of a specimen was fixed within a range of $\psi_0 = 0°$ to $90°$ or $90°$ to $180°$, then the flow velocity was increased from 3.5 ms^{-1} to more than 30 ms^{-1} depending

on the stability of the specimen. A Labview code was used to acquire and save aerodynamic forces and moments.

Two types of flexible specimens were used in the experiments : circular rods and flat ribbons. The circular rods are made using polyurethane foam and are internally reinforced with nylon fibers as described in (Hassani *et al.*, 2016) and Chapter 5. The fibers are positioned along one diameter of a cylindrical mold and twisted around its centerline. Foam is poured and and left to expand in the closed mold, then cure over several hours. As a result, the rod is conferred with anisotropic bending rigidity $(EI)_y/(EI)_x < 1$ and a natural twist (Fig 4.1a). To evaluate the uniformity of foam rods, a specimen was cut to smaller pieces of equal size. Measuring the weight of pieces showed that the density of the foam varies by approximately seven percent along the length of a rod, which is uniform enough for the purpose of this study. Moreover, the foam rigidity is significantly smaller than that of fibers therefore the effect of this non-uniformity is minimized. To maintain the uniformity of fibers inside the foam, they were kept apart with small spacers to ensure a uniform twist and a constant distance between them. A circular section was used in order to simplify the fluid loading evaluation in the theoretical model. The flat ribbons, on the other hand, have intrinsic directional rigidity due to their greater-than-unity width to thickness ratio (Fig 4.1b). They are made of ABS plastic and twisted along their length with a range of intrinsic twist angles τ_0. Annealing at 100 C for several hours was performed to make the twisted state of the rods their stress-free state (see Chapter 5 for more detail).

The anisotropic bending rigidity of the rods and the ribbons form a material frame $(\mathbf{e}_x, \mathbf{e}_y, \mathbf{e}_z)$ where $\mathbf{e}_y$ is along the more rigid direction (Fig 4.1c and d) and $\mathbf{e}_z$ is tangent to the centerline (Fig 4.1e). For a chiral ribbon, fluid loading depends on the alignment of its sections with respect to the flow direction i.e. the local angle of incidence ψ (Hassani *et al.*, 2016). The directional rigidity gives rise to a three-dimensional deformation in asymmetric bending. In the tests, the clamped end of each specimen was rotated around its centerline to have different values of incidence angle at the clamped end ψ_0. Eleven specimens, as listed in Table 4.1, were made for a range of intrinsic twist angles τ_0 varying from 0° to 720°. The specimens named C are circular reinforced rods made of polyurethane foam and the specimens named S are ribbons made of ABS plastic. Three-points bending tests were performed with a universal testing frame to evaluate the bending rigidity of the rods and ribbons. The Young's modulus for all ribbon specimens is the same. For the circular rods, it is assumed that the Young's modulus of the foam part has a linear relation with the rod's density. The maximum and minimum bending rigidity for a circular rod with τ_0 = 0° was measured and the rigidity of the other circular rods was reconstructed based on the aforementioned assumption.

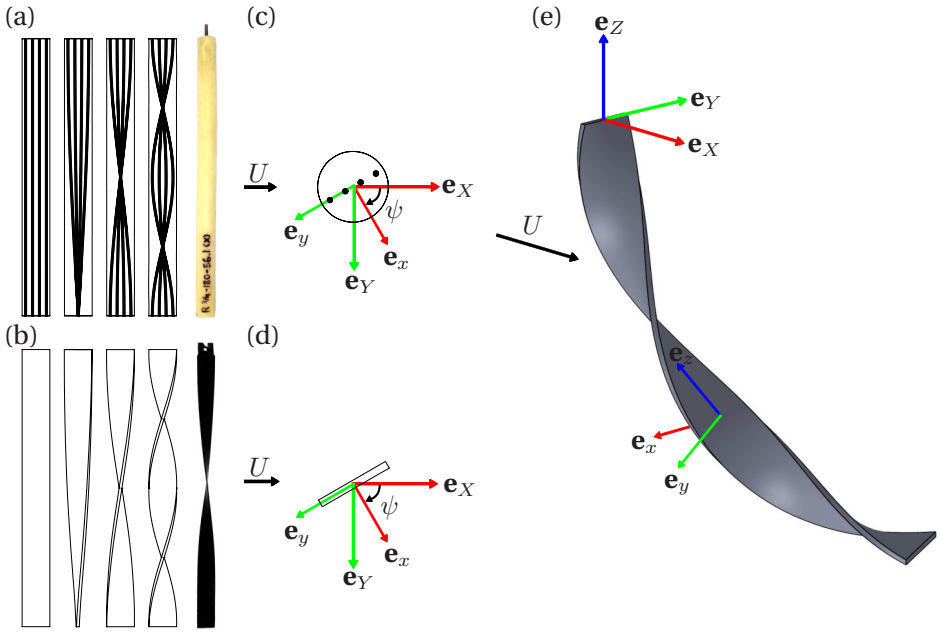

Figure 4.1 a) Schematics of chiral rods with an intrinsic twist angle varying from 0° to 360° as well as a real rod specimen. b) Schematics of chiral ribbons with an intrinsic twist angle varying from 0° to 360° a well as a real twisted ribbon. c) Section of a chiral rod and d) section of a chiral ribbon both with an incidence angle of ψ. e) Schematic of a chiral ribbon deformed in the flow with a moving material frame attached to its centerline.

Table 4.1 Physical properties of tested specimens

Specimen	L (cm)	d (cm)	t (cm)	$(EI)_y$(Nm^2)	$\frac{(EI)_y}{GJ}$	$\frac{(EI)_y}{(EI)_x}$	Weight (g)	Twist τ_0
C1	26	1.9	-	0.0036	1.25	0.16	25	0°
C2	26	1.9	-	0.0036	1.25	0.16	25	90°
C3	26	1.9	-	0.0036	1.25	0.16	25	180°
C4	26	1.9	-	0.0029	1.25	0.13	20	270°
C5	26	1.9	-	0.0029	1.25	0.13	20	360°
C6	26	1.9	-	0.0029	1.25	0.13	20	720°
S1	40	2.5	0.12	0.010	0.675	0.0022	13	0°
S2	40	2.5	0.12	0.010	0.675	0.0022	13	90°
S3	40	2.5	0.12	0.010	0.675	0.0022	13	180°
S4	40	2.5	0.12	0.010	0.675	0.0022	13	270°
S5	40	2.5	0.12	0.010	0.675	0.0022	13	360°

4.2.2 Theoretical Model

The three-dimensional reconfiguration of chiral structures is modeled theoretically using the Kirchhoff theory of rods. In the model, a rod is represented by a deforming three-dimensional

and inextensible curve with the assumption of small strains (Dill, 1992). It is also assumed that each cross section of the rod remains planar and normal to the centerline. The rod is attached to a fixed coordinate system $(\mathbf{e}_X, \mathbf{e}_Y, \mathbf{e}_Z)$ from one end and moving material frames $(\mathbf{e}_x, \mathbf{e}_y, \mathbf{e}_x)$ are attached to its centerline (Fig 4.1e). Bending moments and the twisting moments are proportional to the curvatures, $(\kappa_x\ ,\ \kappa_y)$ and the twist (τ), respectively :

$$M_x = (EI)_x \kappa_x\ ,\ M_y = (EI)_y \kappa_y\ ,\ M_z = GJ\tau\ , \tag{4.1}$$

where $(EI)_y$ and $(EI)_x$ are the bending rigidities and GJ is the torsional rigidity. In this model, the natural twist and curvature of a rod is represented by $\kappa_{x,0}$, $\kappa_{y,0}$ and τ_0. As detailed in (Hassani *et al.*, 2016), the equilibrium Kirchhoff equations are :

$$\frac{dN_x}{ds} = N_y\tau - T\kappa_y - P_x - W_x\ , \tag{4.2}$$

$$\frac{dN_y}{ds} = T\kappa_x - N_x\tau - P_y - W_y\ , \tag{4.3}$$

$$\frac{dT}{ds} = N_x\kappa_y - N_y\kappa_x - P_z - W_z\ , \tag{4.4}$$

$$(EI)_x\frac{d\kappa_x}{ds} = (EI)_y(\kappa_y - \kappa_{y,0})\tau - GJ(\tau - \tau_0)\kappa_y + N_y\ , \tag{4.5}$$

$$(EI)_y\frac{d\kappa_x}{ds} = GJ(\tau - \tau_0)\kappa_x - (EI)_x(\kappa_x - \kappa_{x,0})\tau - N_x\ , \tag{4.6}$$

$$GJ\frac{d\tau}{ds} = (EI)_x(\kappa_x - \kappa_{x,0})\kappa_y - (EI)_y(\kappa_y - \kappa_{y,0})\kappa_x\ , \tag{4.7}$$

where N_x and N_y are shear forces and T is the internal tensile force. Moreover, P is the external loading and $W = mgL^{-1}$ is the weight per unit length in the Z-direction, both decomposed in the three directions of the material frame. The material frame $(\mathbf{e}_x, \mathbf{e}_y, \mathbf{e}_z)$ is related to the fixed frame $(\mathbf{e}_X, \mathbf{e}_Y, \mathbf{e}_Z)$ through the direction cosine matrix $[c]$:

$$\begin{Bmatrix} \mathbf{e}_x \\ \mathbf{e}_y \\ \mathbf{e}_z \end{Bmatrix} = \begin{bmatrix} c_{11} & c_{12} & c_{13} \\ c_{21} & c_{22} & c_{23} \\ c_{31} & c_{32} & c_{33} \end{bmatrix} \begin{Bmatrix} \mathbf{e}_X \\ \mathbf{e}_Y \\ \mathbf{e}_Z \end{Bmatrix}\ . \tag{4.8}$$

The direction cosines represent the rotation of the material frame and they are the cosines of the angles between a direction of the material frame and the directions of the fixed frame. The spatial derivative of a direction of the material frame with respect to the arclength s is (Audoly and Pomeau, 2010) :

$$\frac{d\mathbf{e}_i}{ds} = \mathbf{\Omega} \times \mathbf{e}_i\ , \tag{4.9}$$

where $\mathbf{e}_i$ is a direction of the material frame and $\mathbf{\Omega}$ is the *Darboux vector* :

$$\mathbf{\Omega} = \kappa_x \mathbf{e}_x + \kappa_y \mathbf{e}_y + \tau \mathbf{e}_z \ . \tag{4.10}$$

Substituting Eq.(4.10) in Eq.(4.9) leads to a system of nine equations, six of which are independent. In the model, the six independent spatial derivative equations are coupled with the Kirchhoff equations (Eq.(4.2) to Eq.(4.7)) to define the full state of the deformed rod.

A semi-empirical formulation of the aerodynamic force on a rod is also used to evaluate the loading on the deformed specimens (Hassani *et al.*, 2016; Taylor, 1952). In this method, the local lift and drag of a rod element depends only on the element's orientation and the normal component of the flow velocity to the centerline at the element. The flow velocity is taken to be in the X-direction :

$$\mathbf{U} = U\mathbf{e}_X = U_z \mathbf{e}_z + U_n \mathbf{e}_n \ , \tag{4.11}$$

where U is the magnitude of the flow velocity and $\mathbf{e}_n$ is the direction normal to the centerline in the XZ-plane. The local angle θ between the centerline of the rod and the flow velocity direction is :

$$\cos\theta = \mathbf{e}_z.\mathbf{e}_X = c_{31} \ , \ \sin\theta = \sqrt{1 - c_{31}^2} \ . \tag{4.12}$$

Therefore, the component of flow velocity normal to the centerline is :

$$U_n = U\sqrt{1 - c_{31}^2} \ . \tag{4.13}$$

The friction drag along the centerline produced by $U_z\mathbf{e}_z$ is not considerable therefore we neglect it in the model. The drag normal to the centerline per unit length is in the direction of the normal velocity :

$$\mathbf{D} = \frac{1}{2}\rho d C_D {U_n}^2 \mathbf{e}_n \ , \tag{4.14}$$

where C_D is the drag coefficient. Similarly, the normal lift force per unit of length is written as :

$$\mathbf{L} = \frac{1}{2}\rho d C_L {U_n}^2 \mathbf{e}_l \ , \tag{4.15}$$

where C_L is the lift coefficient and $\mathbf{e}_l$ is the direction of the normal lift force. The direction of the normal drag $\mathbf{e}_n$ is parallel to the projection of $\mathbf{e}_X$ on the xy-plane :

$$\mathbf{e}_n = \frac{\mathbf{e}_X - (\mathbf{e}_X.\mathbf{e}_z)}{|\mathbf{e}_X - (\mathbf{e}_X.\mathbf{e}_z)|} = \frac{c_{11}\mathbf{e}_x + c_{21}\mathbf{e}_y}{\sqrt{1 - c_{31}^2}} \ , \tag{4.16}$$

Similarly, the direction of the normal lift $\mathbf{e}_l$ is parallel to the projection of $\mathbf{e}_Y$ on the xy-plane :

$$\mathbf{e}_l = \frac{\mathbf{e}_Y - (\mathbf{e}_Y.\mathbf{e}_z)}{|\mathbf{e}_Y - (\mathbf{e}_Y.\mathbf{e}_z)|} = \frac{c_{12}\mathbf{e}_x + c_{22}\mathbf{e}_y}{\sqrt{1 - c_{32}^2}} \ . \tag{4.17}$$

By extending this approach, the normal lift and drag forces of a deformed ribbon element δs can be evaluated locally by introducing the sectional drag and lift coefficients $C_D(s)$ and $C_L(s)$ which depend on the local orientation of the rod. This is based on the assumption that the cross section of rods and ribbons does not deform. To evaluate the sectional drag and lift coefficients for ribbons whether chiral or straight, wind tunnel measurements are performed on rigid straight metallic strips with a similar geometry and the same sectional aspect ratio $\sqrt{(I_x/I_y)}$ for a range of angles of incidence ψ_0. Consequently, the variation of C_D and C_L as a function of the angle of incidence is obtained for a rectangular section. In addition, the variation of the sectional angle of incidence for a deformed ribbon, as a function of the arc length s, is calculated in the mathematical model. Therefore, C_D and C_L as a function of the arc length s can be evaluated. For a circular rod, $C_D(s)$ is a constant and $C_L(s)$ is null. It is assumed that for Reynolds numbers within the range of 10^3 to 10^5, the drag and lift coefficients do not change with flow velocity.

The external loading P in Eq.(4.2) to Eq.(4.4) for a rod in fluid flow is the resultant of the drag and lift forces. By decomposing the external loading in the directions of the material frame we have :

$$P_x = \mathbf{D}.\mathbf{e}_x + \mathbf{L}.\mathbf{e}_x \ , \tag{4.18}$$

$$P_y = \mathbf{D}.\mathbf{e}_y + \mathbf{L}.\mathbf{e}_y \ , \tag{4.19}$$

$$P_z = 0 \ . \tag{4.20}$$

The angle between the x and y-components of the normal drag is the sectional angle of incidence. Therefore, using Eq.(4.18) and Eq.(4.19)

$$\psi = \arctan(-\frac{c_{21}}{c_{11}}) \ . \tag{4.21}$$

In the model we assume that the positive rotation is clockwise thus a negative sign is imposed in Eq.(4.21).

Dimensionless Equations

Dimensionless Kirchhoff equations of a deforming rod are written using the Cauchy number :

$$C_Y = \frac{\rho U^2 L^3 d}{2(EI)_y} \ . \tag{4.22}$$

The Cauchy Number is the ratio of the fluid force to the minimum bending rigidity of the flexible body (Gosselin and de Langre, 2011; Chakrabarti, 2002; de Langre, 2008). The following dimensionless parameters are also introduced in the Kirchhoff equations (Hassani *et al.*, 2016) :

$$\bar{s} = s/L \qquad \bar{\kappa}_x = \kappa_x L \qquad \bar{\kappa}_y = \kappa_y L \qquad \bar{\tau} = \tau L \ ,$$
$$\bar{N}_x = \frac{N_x L^2}{(EI)_y} \qquad \bar{N}_y = \frac{N_y L^2}{(EI)_y} \qquad \bar{T} = \frac{T L^2}{(EI)_y} \qquad \mathcal{W} = \frac{mgL^2}{(EI)_y} \ .$$

By introducing the aforementioned dimensionless parameters in Eq.(4.2) to Eq.(4.7), dimensionless Kirchhoff equations are written as follows :

$$\frac{d\bar{N}_x}{d\bar{s}} = \bar{N}_y\bar{\tau} - \bar{T}\bar{\kappa}_y - \bar{P}_x - \mathcal{W}_x \ , \tag{4.23}$$
$$\frac{d\bar{N}_y}{d\bar{s}} = \bar{T}\bar{\kappa}_x - \bar{N}_x\bar{\tau} - \bar{P}_y - \mathcal{W}_y \ , \tag{4.24}$$
$$\frac{d\bar{T}}{d\bar{s}} = \bar{N}_x\bar{\kappa}_y - \bar{N}_y\bar{\kappa}_x - \bar{P}_z - \mathcal{W}_z \ , \tag{4.25}$$
$$\frac{d\bar{\kappa}_x}{d\bar{s}} = \lambda(\bar{\kappa}_y - \bar{\kappa}_{y,0})\bar{\tau} - (\frac{\lambda}{\eta})(\bar{\tau} - \bar{\tau}_0)\bar{\kappa}_y + \lambda\bar{N}_y \ , \tag{4.26}$$
$$\frac{d\bar{\kappa}_x}{d\bar{s}} = (\frac{1}{\eta})(\bar{\tau} - \bar{\tau}_0)\bar{\kappa}_x - (\frac{1}{\lambda})(\bar{\kappa}_x - \bar{\kappa}_{x,0})\bar{\tau} - \bar{N}_x \ , \tag{4.27}$$
$$\frac{d\bar{\tau}}{d\bar{s}} = (\frac{\eta}{\lambda})(\bar{\kappa}_x - \bar{\kappa}_{x,0})\bar{\kappa}_y - \eta(\bar{\kappa}_y - \bar{\kappa}_{y,0})\bar{\kappa}_x \ , \tag{4.28}$$

where the dimensionless external forces are

$$\bar{P}_x = C_Y C_D(s)\sqrt{(1 - {c_{31}}^2)}c_{11} + C_Y C_L(s)\frac{1 - {c_{31}}^2}{1 - {c_{32}}^2}c_{12} \ , \tag{4.29}$$
$$\bar{P}_y = C_Y C_D(s)\sqrt{(1 - {c_{31}}^2)}c_{21} + C_Y C_L(s)\frac{1 - {c_{31}}^2}{1 - {c_{32}}^2}c_{22} \ . \tag{4.30}$$

Dimensionless parameters λ and η are the bending rigidity ratio and the twist-to-bend ratio, respectively (Hassani *et al.*, 2016) :

$$\lambda = \frac{(EI)_y}{(EI)_x} \ , \tag{4.31}$$

$$\eta = \frac{(EI)_y}{GJ} \ . \tag{4.32}$$

Since the dimensionless weight of the rod is in the Z-direction of the fixed frame, it is decomposed in the three directions of the material frame as :

$$\mathcal{W}_x = \mathcal{W}.c_{31} \ , \tag{4.33}$$

$$\mathcal{W}_y = \mathcal{W}.c_{32} \ , \tag{4.34}$$

$$\mathcal{W}_z = \mathcal{W}.c_{33} \ . \tag{4.35}$$

The system of equations including Eq.(4.23) to Eq.(4.28) coupled with Eq.(4.9) is solved using MATLAB as a boundary value problem using the `bvp4c` solver. As explained in (Hassani *et al.*, 2016), a continuation approach is used to solve the system of equations. In the method, an initial guess for all twelve variables is considered. The solution is then evaluated step by step for an increasing Cauchy number. This approach is continued up to a higher limit of Cauchy number i.e. 1000. However, to study the cases including a static instability such as buckling, the governing equations are solved using AUTO (Doedel and Kernevez, 1986). This software package solves problems which can include bifurcations. In the software, a continuation parameter is considered and the governing equations are solved for a range of that parameter. For this buckling problem, the dimensionless weight $\mathcal{W}$ is the continuation parameter. A cross-comparison has been done for cases without bifurcation between the MATLAB code and the AUTO solver which show identical results to seven significant figures (Hassani *et al.*, 2016).

4.3 Results and Discussion

4.3.1 Mathematical Model Verification

A comparison has been performed in (Hassani *et al.*, 2016) on the three-dimensional deformed shape of non-chiral rods, obtained from wind tunnel tests and the present mathematical model. Herein, only the validation of the chirality component in the mathematical model is investigated. To validate the mathematical model, the numerical and experimental results for the deformation of circular chiral rods with different τ_0 are presented in Fig. 4.2a. In the test,

the rods were clamped from one end horizontally, and deforming under their own weight. Each specimen was rotated around its centerline to have different values of incidence angle at the clamped end ψ_0. In the figure, the tip vertical deflection is plotted as a function of the incidence angle for three different intrinsic twist angles. Markers represent the measured values and curves represent the mathematical prediction. Results show that the maximum vertical deflection and consequently the effective bending rigidity varies with the incidence angle ψ_0. Moreover, by increasing the intrinsic twist angle, the deflection of the rods becomes less dependent upon the direction of loading. The mathematical model shows good agreement with the experimental results. Another verification is carried out by comparing the measured drag and lift coefficients of a rigid twisted rod ($\tau_0 = 90°$) with the mathematical model which is provided in Chapter 5.

4.3.2 Buckling

It has been noted that chirality is beneficial to plants since it increases their strength against buckling under their own weight or that of their head organ (Zhao *et al.*, 2015; Schulgasser and Witztum, 2004). We study the buckling of chiral ribbons and rods under their own weight which are similar to upright slender plants without a head organ such as a cattail leaf. Figure 4.2b illustrates the effect of chirality on the relative critical length of buckling $L_r = L_{cr}/L_{cr,0}$ where $L_{cr,0}$ is the critical length of a non-chiral rod or ribbon ($\tau_0 = 0°$) buckling in the plane of least resistance ($\psi_0 = 0°$). It should be mentioned that according to our mathematical modeling and also the Euler buckling theory, $L_{cr,0} \approx \sqrt[3]{7.837(EI)_y/\gamma}$ for a self weight buckling case where γ is the weight per unit length. In the figure, L_r is plotted for several bending rigidity ratios and for a range of intrinsic twist angle from 0° to 720°. Each curve corresponds to a value of the bending rigidity ratio while the other structural parameters are kept constant. It is shown that increasing the intrinsic twist angle increases the critical buckling length meaning that the buckling strength is increased. Moreover, decreasing the bending rigidity ratio or equivalently increasing the sectional aspect ratio, increases the influence of chirality on the critical buckling length. This means that chirality is more effective for ribbons with a small λ than rods with a circular section and large λ. In addition, the twist-to-bend ratio η does not affect the critical buckling length.

4.3.3 Drag and Lift Coefficients

As mentioned before, for the mathematical model it is necessary to evaluate the sectional drag and lift coefficients of the rods as a function of the sectional angle of incidence. For circular rods, the drag coefficient of an equivalent rigid rod is measured as $C_D = 0.95$ which

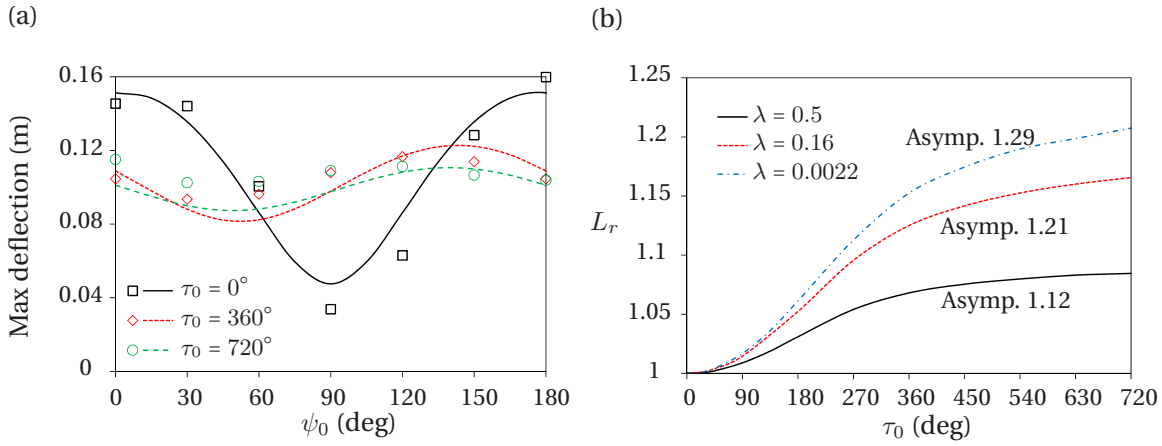

Figure 4.2 a) Static bending test for chiral circular rods. The rods are fixed horizontally from one end and their maximum vertical deflection is plotted vs. the angle of incidence at the fixed end. Markers represent the experimental results. b) The effect of chirality and the bending rigidity ratio of rods on their critical buckling length.

is used as the sectional drag coefficient. For the ribbons, the drag and lift coefficients of an equivalent flat metallic strip were measured for a range of incidence angles. To simplify the model, the average of the drag and lift measurements for Re = 10000 and 20000 were fitted using trigonometric functions (see Chapter 5) :

$$C_D(\psi) = 1.37\,|\cos(\psi)| + 0.05\ , \tag{4.36}$$

$$C_L(\psi) = 0.80\sin(2\psi)\ . \tag{4.37}$$

The flat metallic strip possessed the same dimensions as the flexible ribbons (400×25.4 mm). Moreover, the measured pitching moment was found to be very small with respect to the torsional rigidity of ribbons therefore it was neglected in the mathematical model.

4.3.4 Drag of Flexible Specimens

Herein, the wind tunnel results represent the time-averaged values of fluctuating loads measured over 30 seconds. The time-averaged values exhibit a standard deviation of less than 10 percent, or else are deemed unacceptable and are discarded. At high velocities, the rods and the ribbons underwent large amplitude vibrations possibly due to turbulence buffeting, although some flutter or galloping phenomena cannot be ruled out. For the lowest flow velocity in the experiments, the vortex shedding frequency is estimated to 40 Hz for a Strouhal number of 0.2. This frequency is largely beyond the fundamental frequency of the tested ribbons and circular rods which is of the order of 2 Hz (Hassani *et al.*, 2016). In the results

presented here, only the static deformations of the rods and ribbons are considered.

In reality, plants can be subjected to wind loading from any direction. The present work shows that the drag on a specimen is highly dependent on the incidence angle. Figure 4.3a and Fig. 4.3b show rose plots of drag force on chiral circular rods at $U = 13$ ms^{-1} and ribbons at $U = 15$ ms^{-1}, respectively. On the rose plots, the radial distance of points indicates the drag loading magnitude as a function of the angle of incidence, i.e. the loading direction. In the figures, each curve represents a simulation for a fixed value of the intrinsic twist angle while symbols represent its equivalent experimental data. The aforementioned flow velocities were selected for large deformations with a maximum number of valid wind tunnel tests. A range of 90° for ψ_0 was tested in the wind tunnel. However, depending on the initial alignment and the handedness of chiral specimens, either the range of $\psi_0 = 0°$ to 90° or $\psi_0 = 90°$ to 180° was measured. As seen, the drag force strongly varies with the wind direction for a non-chiral rod and ribbon. As the intrinsic twist angle increases, both plots approach a perfect circle meaning that the drag becomes less direction dependent. It should be noted that some of the experimental data are missing in the plots because they were not acceptable due to a standard deviation larger than 10 percent.

To better understand the effect of chirality, for each intrinsic twist angle, we vary the incidence angle to maximize and minimize drag. Figure 4.3c and Fig. 4.3d show the mathematical prediction of these extremums for chiral circular rods and ribbons for a range of the intrinsic twist angle τ_0 from 0° to 720°. In these figures, the relative drag of rigid circular rods as well as the maximum and minimum drag of equivalent rigid ribbons are provided for reference. In the mathematical model, the relative drag of chiral rods and ribbons with a specific chiral angle τ_0, is evaluated for a range of ψ_0 from 0° to 360°. The maximum and minimum relative drag can be found at any angle in this range depending on τ_0. The relative drag force is calculated as $D_r = D/D_0$ where D_0 is the drag of a rod with $\tau_0 = 0°$ and $\psi_0 = 0°$. The markers represent the experimental drag data regardless of the incidence angle. The relative drag force of a non-chiral rod is maximum at $\psi_0 = 90°$ and minimum at $\psi_0 = 0°$. On the other hand, the relative drag force of a non-chiral ribbon is maximum at $\psi_0 \approx 45°$ and the minimum at $\psi_0 = 90°$. The reason is that the projected area of a circular rod does not change with ψ_0 but the projected area of a non-chiral ribbon is minimum at $\psi_0 = 90°$ and maximum at $\psi_0 = 0°$. This is valid only for non-chiral rods and ribbons and it is not necessarily applied to chiral ones. In Fig. 4.3c, the flow velocity is $U = 13$ ms^{-1} which is equivalent to $C_Y = 10$ where reconfiguration is important. For the mathematical model, the average mechanical properties of the circular rods in Table 4.1 were used. Moreover, a constant $C_D = 0.95$ was considered. As seen, the maximum relative drag decreases and the minimum relative drag increases. This means that the difference between the maximum and the minimum drag decreases indicating

that the drag becomes direction independent for high intrinsic twist angles. This is similar to the static bending results presented in Fig. 4.2a which shows that the chirality makes the deformation of a rod less dependent on the loading direction. It can also be found in Fig. 4.3c that chirality is beneficial for circular rods since it decreases the fluid loading. Higher drag forces usually lead to higher stresses therefore chirality should be helpful for plants with circular or semi-circular sections in reducing the probability of structural failure.

Fig. 4.3d presents the relative drag force on chiral ribbons for $U = 15$ ms^{-1} or $C_Y = 20$. It is seen that the minimum and the maximum relative drag increase up to a value of τ_0 of 90° and 180°, respectively. Beyond 180°, the maximum drag decreases. Similarly to Fig. 4.3c, the range between the maximum and the minimum drag values decreases with increasing intrinsic twist angle. In addition, the drag of rigid ribbons also becomes less directional and approaches an asymptotic value. Similarly, it was reported in (Cucuel, 2016) that the drag coefficient of a rigid chiral ribbon approaches a constant value for very high twist angles. The maximum and minimum drag of rigid ribbons exhibit a periodic variation with chirality. This periodic variation is less pronounced for flexible ribbons. The reason is that in general, the drag of flexible ribbons is less than rigid ones therefore the variation amplitude of their maximum and minimum drag is also smaller. Moreover, flexible ribbons deform and become aligned with the flow. This reduces the effect of chirality on their drag.

This trend is not present for circular chiral rods because it is related to the complex aerodynamic loading on chiral ribbons. For a chiral cylinder, the aerodynamic loading is governed by a single constant drag coefficient regardless of the intrinsic twist angle. In this case, the structural effect of chirality governs the drag scaling. On the other hand, a chiral ribbon is affected by both the structural and the aerodynamic aspects of the chiral morphology. The competition between these two aspects of chirality leads to a more complex response in chiral ribbons.

4.3.5 Curvature and Bending Moment

Chirality induces a non-uniform distribution of curvature along the length of the rod or ribbon. This is shown in Fig. 4.4 for ribbons using the mathematical model. The results are qualitatively similar for circular rods (not shown). In Fig. 4.4a, the deformed shape of a non-chiral ribbon with $\psi_0 = 0°$ under a terminal dimensionless bending moment $\bar{M}_Y = M_Y L/(EI)_y = 1.2$ is shown. As expected, the deformation is uniform with a constant curvature. On the other hand, Fig. 4.4b shows the deformed shape of a chiral ribbon with $\tau_0 = 360°$ under the same loading. As indicated with small arrows, the deformed shape includes three regions of concentrated curvature which we call “nodes”. Moreover, the amplitude of deformation is smaller

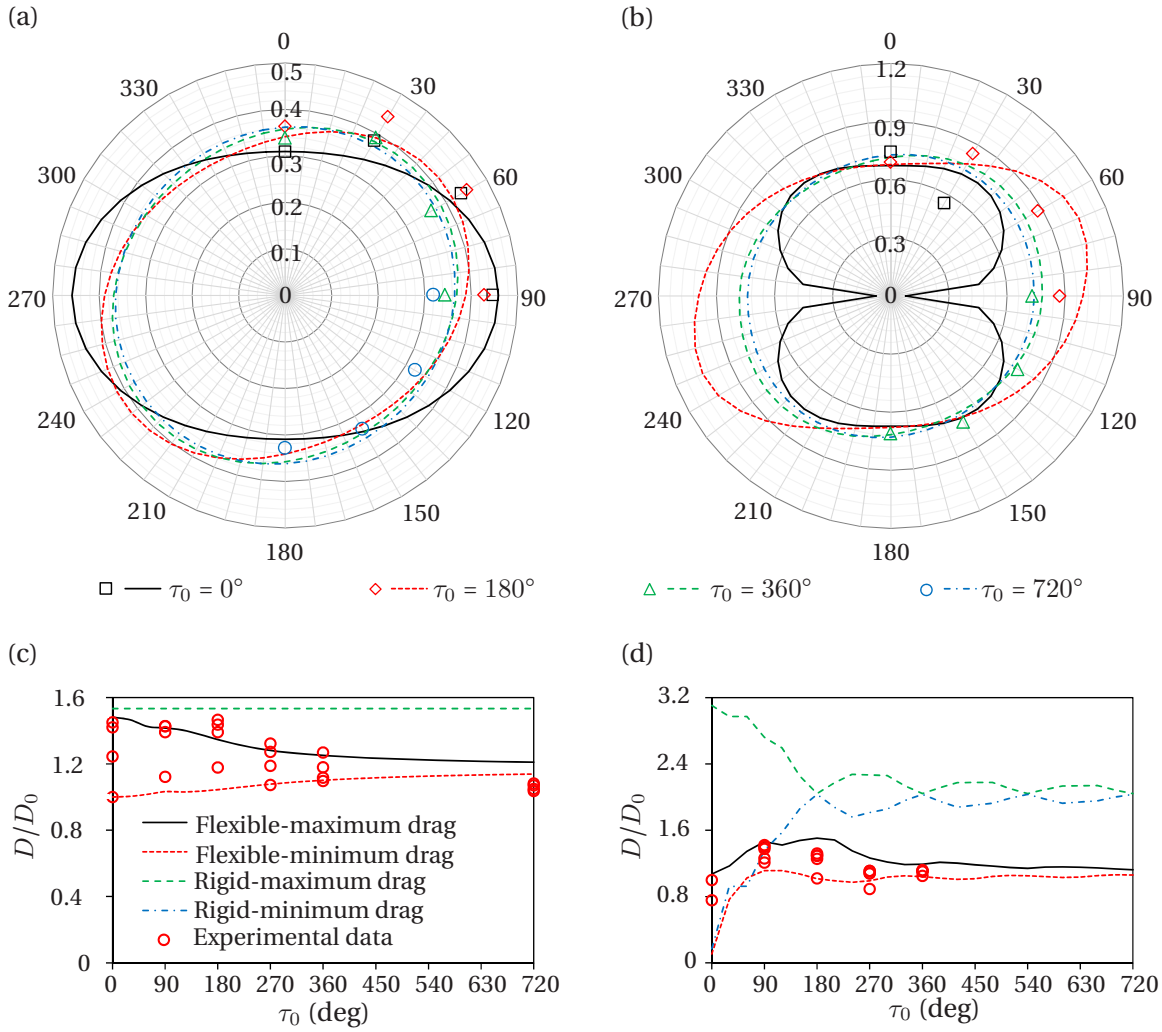

Figure 4.3 Rose plot of drag as a function of the intrinsic twist angle, τ_0 and the incidence angle, ψ for a) chiral circular rods with U = 13 ms^{-1} and b) chiral ribbons with U = 15 ms^{-1}. c) Maximum and minimum relative drag of chiral circular rods at U = 13 ms^{-1} and d) chiral ribbons at U = 15 ms^{-1} among a range of incidence angles. Markers represent the experimental data and lines show the mathematical prediction. The maximum and minimum drag of equivalent rigid rods and ribbons are also provided for reference.

compared with a non-chiral ribbon because the overall effective bending rigidity is increased due to the twist of the material frame along the centerline. To understand this, the total curvature $\kappa_t = \sqrt{\kappa_x^2 + \kappa_y^2}$ of weightless deforming ribbons under a terminal moment $\bar{M}_Y = 1.2$ with $\psi_0 = 0°$ is presented as a contour plot in Fig. 4.4e. The contour shows the variation of the total curvature along the ribbon's length for a range of τ_0 from 0° to 720°. The nodes can be recognized in the contour as the dark regions. For instance, for τ_0 = 360° we can find three distinctive dark regions in the contour which represent three nodes. As seen, by increasing the intrinsic twist angle, the number of nodes increases. Therefore, we say that

chirality "discretizes" the deformation.

Figure 4.4c shows a non-chiral upright ribbon and Fig. 4.4d shows a chiral upright ribbon ($\tau_0 = 360°$) both deforming under wind and gravity with $C_Y = 30$ and $\psi_0 = 0°$. Similarly to the previous case, the non-chiral ribbon undergoes a smooth deformation while the deformed chiral ribbon has two distinctive curvature nodes. Moreover, the deformation of the chiral ribbon is smaller because its overall rigidity is higher due to chirality. Fig. 4.4f shows a contour of the total curvature for upright ribbons in flow with the same aforementioned conditions. Similarly to the case with a terminal moment, it is found that chirality "discretizes" the deformation and the number of nodes increases with chirality. For instance, there are two nodes for $\tau_0 = 360°$ at $\bar{s} = 0$ and 0.4 and four nodes for $\tau_0 = 720°$ at $\bar{s} = 0$, 0.25, 0.5 and 0.75.

An excessive turning moment may uproot a plant. To study the effect of chirality on the maximum root bending moment of chiral plants, we model mathematically five cases as described in Table 4.2 to cover a variety of structural and flow parameters. It should be noted that a negative value for $\mathcal{W}$ indicates that the specimen is upright and a positive value represents a buoyant one. The structural properties for the flexible ribbons and weightless

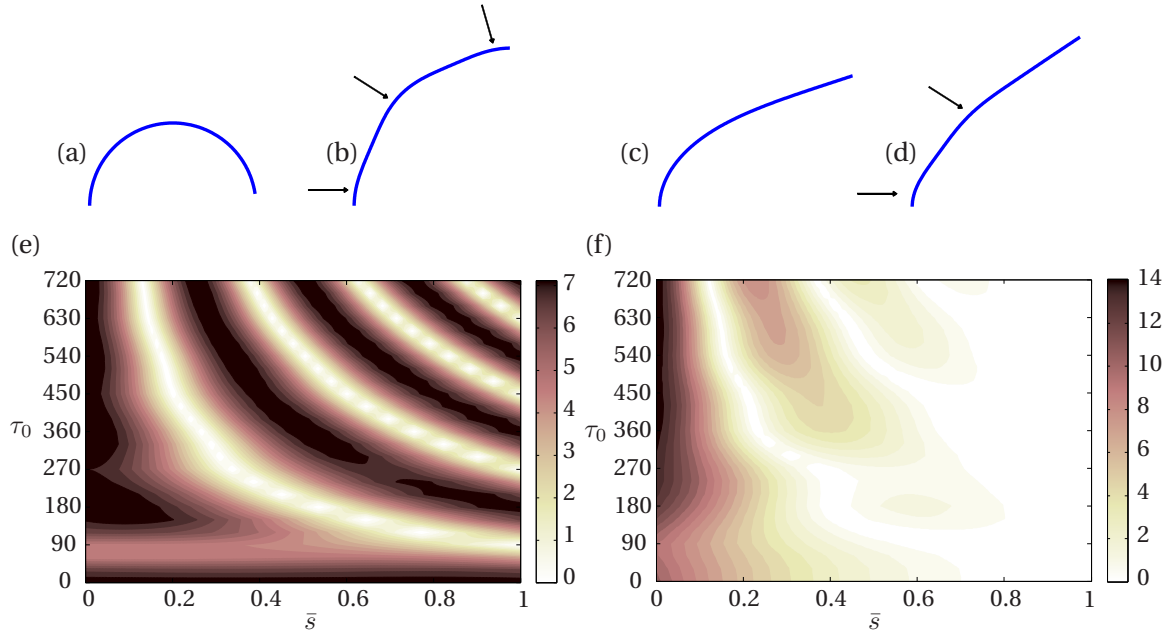

Figure 4.4 Theoretical evaluation of the deformed shape of weightless ribbons under a terminal moment with a)$\tau_0 = 0°$ and b)$\tau_0 = 360°$. Deformed shape of upright ribbons under the wind loading with c)$\tau_0 = 0°$ and d)$\tau_0 = 360°$. Contour of the total curvature κ_t for e) weightless chiral ribbons under a terminal moment and f) upright ribbons in the flow. The terminal moment is $\bar{M}_Y = 1.2$, the Cauchy number is $C_Y = 30$ and ψ_0 is null for all cases. Small arrows show the curvature nodes on the deformed ribbons.

Table 4.2 Physical properties of study cases

Case	Section	L (cm)	d (mm)	t (mm)	$(EI)_y$(Nm^2)	η	λ	$\mathcal{W}$	C_Y
Flexible Ribbon	Rectangular	40	25.4	1.2	0.01	0.675	0.0022	−1.93	30
Ealgrass	Rectangular	40	8	0.35	$2.8e-5$	1	0.0019	20	30
Cattail leaf	Rectangular	65	7.6	1.26	$0.87e-3$	1	0.032	−6.6	30
Weightless Rod	Circular	26	19	-	0.0033	1.25	0.16	0	30
Daffodil Stem	Semi-circular	27	8.5	-	0.012	13.3	0.5	−0.92	30

rods are based on our experimental specimens. The structural properties of eelgrass (Zostera) and daffodil stem are taken from (Luhar and Nepf, 2011; Abdelrhman, 2007) and (Etnier and Vogel, 2000), respectively. It should be noted that the effect of the daffodil flower on top of the stem is not modeled here. For the cattail leaf (Typha angustifoli), the values are the average of measurements which we did on several leaves. Twelve mature leaves were collected from the Voyageur Provincial Park (ON, Canada) in August, 2016. Three-points bending tests were done on segments of the leaves to evaluate their bending rigidity, one day after being collected. It was found that the bending rigidity of a cattail leaf decreases significantly from root to tip mainly due to the reduction of its thickness. Therefore, the average of the bending rigidity, width and thickness of multiple leaf segments was used in the mathematical model. Based on present experiments on cattail leaves, the bending rigidity varies from 0.03×10^{-3} Nm^2 for the tip section to 3.9×10^{-3} Nm^2 for the root section. This shows two orders of magnitude of change in the bending rigidity from tip to root. The average bending rigidity for the cattail leaves is 0.87×10^{-3} Nm^2. Moreover, λ varies for the tested cattail leaves from 0.0025 to 0.1 with an average of 0.032 (see Chapter 5 for more detail). Using the model, the maximum value of the dimensionless bending moment $\bar{M}_{max}$ computed over a range of incidence angles from 0° to 180° is plotted for the aforementioned cases in Fig. 4.5, where $\bar{M} = L\sqrt{M_x^2 + M_y^2}/(EI)_y$. The plots illustrate the variation of $\bar{M}_{max}$ at root as a function of the intrinsic twist angle τ_0. For the daffodil stem, an aerodynamic model similar to a circular rod is used although in reality, the cross section is semi-circular or elliptic. Moreover, the bending rigidity ratio λ for the daffodil stem is calculated as the ratio of the second moment of area around the two sectional axes of symmetry (I_y/I_x). As seen, the variation of $\bar{M}_{max}$ is different between the ribbons with rectangular sections and rods with circular or semi-circular sections. For the circular or semi-circular cases, $\bar{M}_{max}$ at root decreases with increasing τ_0 and approaches a constant value for very high intrinsic twist angles. However, for the cases with a ribbon-like structure, $\bar{M}_{max}$ increases up to a certain value of τ_0 between 120° and 150° ; beyond that, it decreases and approaches a constant value. The mathematical model showed that for cattail leaves in air flow, $\bar{M}_{max}$ is not significantly sensitive to the variation of λ and the bending rigidity. Moreover, the peak value of $\bar{M}_{max}$ is found at 150° for all the study cases. At first

glance, the figure suggests that an untwisted structure is better for plants to reduce the root bending moment. However, as we understood from Fig. 4.2b, chirality increases the buckling strength of upright ribbons which reduces the chance of structural failure. Therefore, chirality brings a trade-off for upright plants with increased buckling strength but also higher root bending moment. For instance, cattail leaves are chiral and according to our measurements, their average intrinsic twist angle is $380^\circ \pm 110^\circ$. The shaded area in Fig. 4.5 represents the distribution of twist angles of the cattail specimens which we have collected. It should be noted that the intrinsic twist angle of plants may vary with environmental parameters.

The results show that eelgrass is subjected to a larger root bending moment with respect to an upright ribbon and a cattail leaf. The reason is that the buoyancy effect decreases the deformation magnitude which leads to a larger drag as suggested by Luhar and Nepf (2011). A larger drag on the plant's body leads to a larger root moment. In comparison, an upright ribbon and a cattail leaf are subjected to a smaller root moment since their weight contributes to the deformation and drag reduction. On the other hand, the reconfiguration of the daffodil stem is highly affected with its large η. This means that the daffodil stem easily reorients to its less rigid direction which leads to a large deformation. The large deformation of the daffodil then reduces the drag and the root moment. However, as seen in Fig. 4.5, a weightless rod with a smaller η than the daffodil stem, has a larger root bending moment. This is specifically interesting since it is known that many plants twist more easily than they bend (Vogel, 1992), which shows that low torsional rigidity is beneficial for plants to reduce the risk of uprooting.

According to Eq.(4.1), $\bar{M}_{max}$ is created at the root due to the contribution of the curvatures in the x and y-directions. Although κ_x is usually smaller than κ_y, its contribution to the bending moment is usually more important due to the higher bending rigidity. This means that uprooting happens because of an excessive bending moment created in the stiffer direction of the plant. Finally, the difference in behavior between structures with rectangular sections and those with circular or semi-circular sections comes from the different aerodynamic loadings on these structures.

4.4 Concluding Remarks

The reconfiguration and buckling of chiral plants was studied using flexible rods and ribbons with a chiral morphology. Wind tunnel experiments were conducted using circular rods with internal reinforcement as well as chiral ribbons. For the theoretical analysis, a Kirchhoff rod model was coupled with a semi-empirical drag and lift formulation. The theoretical model provides a general framework to study the large deformation of rods and ribbons

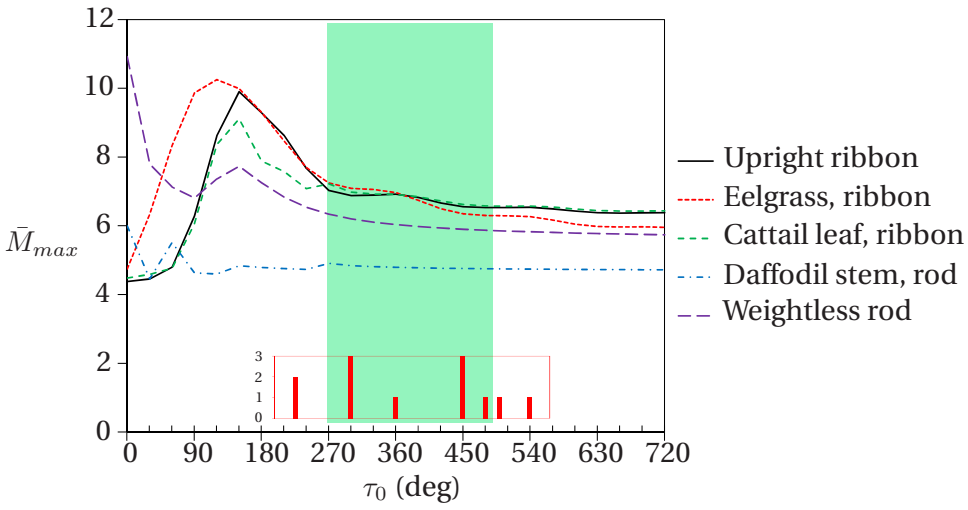

Figure 4.5 Maximum dimensionless bending moment at root of five study cases at $C_Y = 30$. Plots are predicted using the mathematical model. The shaded area represent the range of the most probable intrinsic twist angle of the cattail specimens collected for this study. The small histogram plot shows the distribution of the collected specimens in terms of the intrinsic twist angle.

as well as slender wings in flow. It was shown that chirality increases the critical buckling length and consequently the buckling strength of upright slender structures under their own weight. Chirality was found to render the rods and ribbons less dependent on the direction of external loading such as gravity or wind. Moreover, chiral rods and ribbons show a non-smooth deformation with one or more nodes in their deformed shape due to their geometrical twist. Thus chirality can be said to "discretize" the deformation.

The theoretical model predicts that for circular rods, chirality decreases the root bending moment. On the contrary, the root bending moment of chiral ribbons is higher than a straight ribbon, especially at intermediate angles of chirality around $\tau_0 \approx 150°$. Despite this, many upright plants show a chiral morphology possibly due to its aforementioned benefits including higher buckling strength and weaker dependency on the loading direction. Our measurements on chiral cattail leaves showed that the distribution of their inherent twist angle bypasses the intermediate chiral angles and is centered around a large chiral angle. However, it is of interest to perform measurements on more chiral species which grow upright, to verify their angle of chirality. It is also recommended to account for the variation of the sectional area and bending rigidity along the length in the mathematical model to represent real plant organs such as leaves and stems. Moreover, further experimental and theoretical investigations should be done to study the effect of chirality on the dynamic stability of chiral plants against flutter and vortex-induced vibration.

Acknowledgment

The financial support of the Natural Sciences and Engineering Research Council of Canada is acknowledged.

CHAPTER 5 DETAILS OF EXPERIMENTS

In this chapter, experimental approaches and the fabrication procedure of specimens in the present study is detailed.

5.1 Specimen Fabrication

Both the chiral and straight circular rods were made using polyurethane foam reinforced with nylon fibers. This type of flexible specimen was used for several reasons. First, polyurethane foam is very flexible and can undergo large elastic deformation. Moreover, it is very light which reduces the effect of oscillations on measured loads in the wind tunnel experiments. A circular section was selected due to its simple aerodynamics for the mathematical modeling. However, isotropic circular rods do not twist in flow therefore reinforcement fibers were used to induce anisotropy and torsion. As a result, this study could benefit from the simplicity of circular rods and an induced bending-torsion coupling at the same time. It should be mentioned that the number and the position of nylon fibers were not an interest of this study as they only served to create anisotropy in circular rods. To achieve a proper foam density and flexibility, several types of polyurethane foam from Flexfoam-iT series (Smooth-on Inc., Easton, Pennsylvania) were used to fabricate rod samples. Based on these samples, FlexFoam-iT ! X was selected which provided the best flexibility and integrity for the purpose of this study.

In the fabrication process, nylon fibers were aligned along the axis of a cylindrical mold shown in Fig. 5.1. Fibers were slightly stretched through small holes on the two end caps of

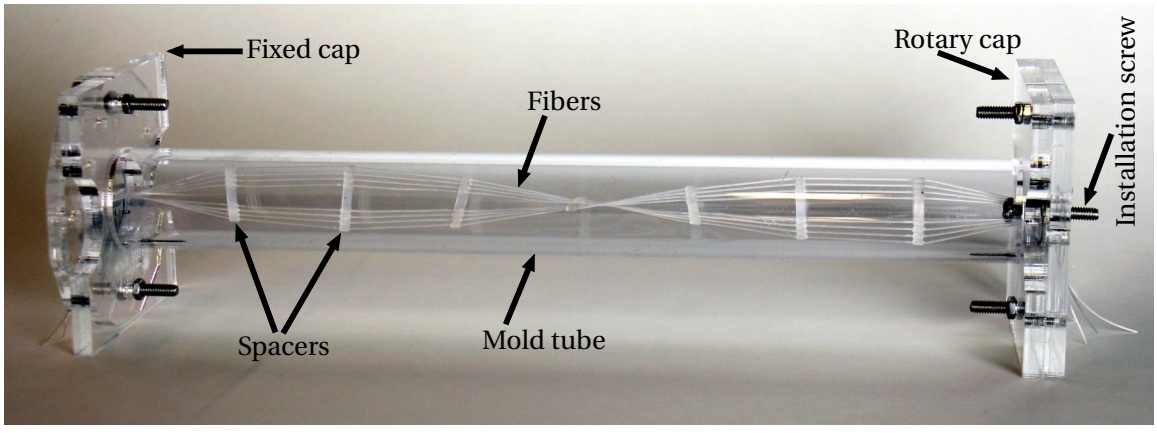

Figure 5.1 Photograph of the mold used to fabricate circular rods.

the mold. Special attention was paid to prevent over-stretching the fibers as it could cause an unwanted natural curvature in the rods after demolding. As seen in the figure, small spacers were used to ensure a uniform twist and a constant distance between fibers. FlexFoam-iT ! X has two liquid components which were mixed for 30 seconds by equal volume before pouring in the mold. A quick release agent was used to prevent foam from sticking to the mold. After pouring the foam from a hole located in the middle of the mold, it expands up to 6 times through an exothermic process. It should be noted that this process releases gas therefore the mold should have a few small ventilation holes otherwise the final result will not have a proper uniformity and integrity. In the case of this study, the produced gas could pass through small fiber holes on the caps. The initial volume of the foam components was found through trial and error for a proper integrity and uniformity. To ensure the uniformity of the fabricated foam rods, a foam specimen without fibers was cut to smaller pieces of equal size. By measuring the weight of each piece, it was found that the density of the foam varies by approximately seven percent along the length of the rod. By performing measurements on the foam rods, it was found that their Young's modulus varied approximately in a linear manner with their density. Therefore, it was concluded that the variation of the Young's modulus and the bending rigidity should be approximately seven percent along the length. This amount of variation was negligible in this study because the rigidity of the fibers was largely greater than that of the foam. In this study, the relative density of the foam was not an important factor because measurements were performed on each fabricated specimen to evaluate their weight, bending rigidity and torsional rigidity. An upside down M4 screw was also placed halfway inside each foam rod during the molding process to facilitate their fixture (Fig. 5.1)

To fabricate ribbons, ABS strips with the thickness of 0.12 cm (3/64 in) and the width of 2.54 cm (1 in) (McMaster-Carr, Elmhurst, Illinois) were used. ABS strips were cut into multiple 42 cm ribbons. Each ribbon was twisted to an angle between 0° and 360°. The twisted ribbon was fixed in a wooden fixture to prevent it from returning to its initial state because of its elasticity. The assembly was then placed in an oven for several hours at 100 C for annealing. The annealing process made the twisted state of the ribbons their stress-free state.

5.2 Bending and Torsional Rigidity

A standard three-point bending test was performed on non-chiral rod and ribbon specimens to measure their bending rigidity. Therefore, the bending rigidity of each specimen was calculated directly from the slope of the load-deflection plot at its middle point. The purpose of these measurements was evaluating the bending rigidity ratio ($\lambda = (EI)_y/(EI)_x$) for all

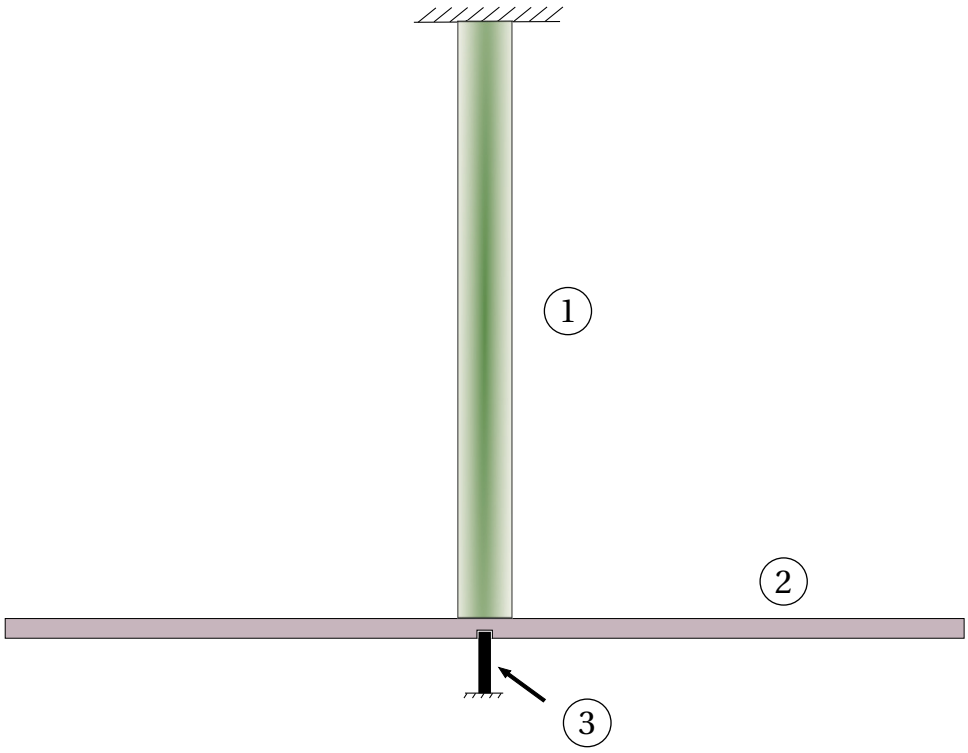

Figure 5.2 Schematic of the test setup used to measure the torsional rigidity of a rod. In this test setup, the rod (1) is attached to the center of a rectangular aluminum plate (2) which can rotate around a pin (3) freely. The pin limits the movement of the aluminum plate to rotation around its center.

specimens. For ribbons, the minimum bending rigidity (EI_y) and the Young's modulus was measured for a straight ribbon and the maximum bending rigidity (EI_x) was evaluated based on the measured Young's modulus and the calculated second moment of area in x-direction (I_x). For straight rods, (EI_y) was measured at $\psi_0 = 0°$ and (EI_x) was measured at $\psi_0 = 90°$ where the incidence angle was defined based on the direction of gravity. However, it was impossible to measure the bending rigidity ratio for chiral rods directly therefore their rigidity was evaluated based on the straight rod rigidity and the assumption of linear relation between the foam density and rigidity.

The torsional rigidity of ribbons was calculated based on their cross sectional dimension :

$$GJ = 0.33Gdt^3 \ , \tag{5.1}$$

where the shear modulus G was calculated from the measured Young's modulus :

$$G = \frac{E}{2(1+\nu)} \ . \tag{5.2}$$

For a circular rod, the torsional rigidity was evaluated by measuring the torsional vibration frequency of the rod attached to a flywheel (Fig. 5.2). In this test, the assembly of a foam rod (1) and a rectangular aluminum plate (2) was constrained to rotate around the rod centerline using a pin (3). For each rod, the natural frequency of the rotational oscillation of the rod-plate assembly ω_n was measured several times to evaluate the rod torsional rigidity using the following :

$$GJ = LJ_m{\omega_n}^2 \ , \tag{5.3}$$

where J_m is the sum of the mass moment of inertia of the foam rod and the aluminum plate around the rod centerline as shown in the figure.

5.3 Drag of Rigid Specimens

To evaluate the reconfiguration number, the drag coefficient of an equivalent rigid specimen with similar geometry was required. For circular rods, the equivalent rigid specimen was made by placing a threaded metallic rod inside the same mold used to make circular rods. Therefore, the surface of the rigid specimen was similar to the circular foam rods. The drag coefficient of the rigid circular rod was measured and found to be approximately constant at $C_D = 0.95$ over the range $5000 < Re < 30000$ of the wind tunnel tests. For the ribbons, an aluminum ribbon with the same dimensions as the ABS ribbons was used as an equivalent rigid structure. Figure 5.3 shows the variation of the drag and lift measurements averaged over $Re = 10000$ and $Re = 20000$ for the aluminum ribbon as a function of the ribbon's incidence angle. To simplify the mathematical model, the average of the drag and lift measurements were fitted using trigonometric functions (Eq. (4.36) and Eq. (4.37))

Figure 5.4 presents the variation of the lift and drag coefficients of a twisted metallic strip ($\tau_0 = 90°$) as a function of the incidence angle ψ_0. The dimensions of the metallic strip are similar to the flexible ribbons used in experiments. In the wind tunnel test, the clamped end of the twisted metallic strip is rotated around its centerline to impose a range of incidence angles from $0°$ to $90°$. In the figure, the lines represent the mathematical prediction for the thickness of $t = 1.5$ mm and $t = 3$ mm. Moreover, the symbols represent the experimental data for two different Reynolds numbers : $Re = 10000$ and $Re = 20000$. As seen, the experimental and the mathematical results are in agreement.

5.4 Details of Wind Tunnel Tests

Test specimens whether rigid or flexible were attached to the force balance using a cylindrical mast to eliminate the effect of the wall boundary layer. To evaluate the drag scaling of each

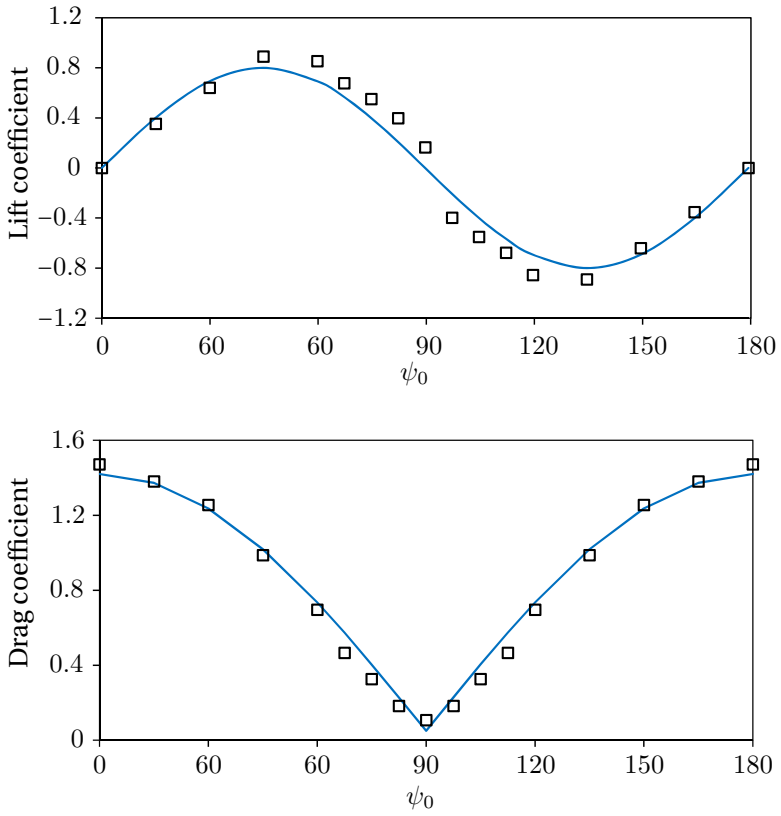

Figure 5.3 Wind tunnel measurements of the lift and drag coefficients of a metallic ribbon equivalent to flexible ABS ribbons averaged over Re = 10000 and Re = 20000. Markers represent experimental values and lines are fitted trigonometric functions (Eq. (4.36) and Eq. (4.37)).

specimen, the drag of the mast was measured separately and subtracted from the total drag of the mast-specimen assembly. The mast used for circular rods is shown in Fig. 5.5a. This is also shown in Fig. 3.2 between the test specimen and the force transducer. As seen in Fig. 5.5a, This mast consists of a circular rod made of acrylic (2a) which can be connected to the force transducer using a circular adapter (1a). A small sleeve (3a) is glued to the acrylic rod with the same internal diameter as the diameter of foam rods. Since the circular foam rods were very soft, their M4 screws were fixed in a threaded hole (4a) and the sleeve was used for additional support. The sleeve was designed to fit around the foam rod and ensure a better clamped boundary condition. Despite these efforts, it was impossible to maintain a perfect clamped condition for the foam rods due to their soft structure. The sleeve of the mast dug into the foam rods when they were subjected to flow. To compensate for this imperfection at the clamped end, a modification was made in the mathematical model. For this modification, the clamped boundary condition was relaxed into a torsion spring. The side view photographs of the foam rods in flow at $\psi_0 = 90°$ were used to estimate the rotation

of the rods around their clamped end as a function of flow velocity. The incidence angle of 90° was chosen because at this angle rods are very rigid and they do not deform significantly along their length therefore they can be considered as a straight rod. Using this assumption, it was possible to evaluate the bending moment around the clamped end M_Y for each flow velocity. Therefore, the torsion coefficient of spring k_s could be evaluated considering a linear spring. By knowing k_s, a Robin boundary condition can be formulated for the attached end (Eq. (3.3)).

The mast used for ribbons is shown in Fig. 5.5b. As seen, this mast is an acrylic rod (2b) connected to the force transducer using a circular adapter (1b). At one end of the acrylic rod, there is a slot (3b) to hold ribbons using a screw which goes to a threaded hole (4b). The slot was slightly smaller than the thickness of ribbons to ensure a tight fit. The reference point or the origin of the fixed coordinate system used for all results considering the rod shape such as Fig. 3.6, is shown schematically in Fig. 5.5a and b as small green ellipses at the end of the masts.

Drag and lift measurements were performed in a wind tunnels. For each test, an incidence angle was set and the flow velocity was changed from 5 ms^{-1} to a maximum velocity before strong instabilities occur. During the tests, aerodynamic loading and the air pressure at the test section were monitored and saved using a Labview program for at least 30 seconds. Each angle of incidence for a specific specimen was tested once. The time-average and the

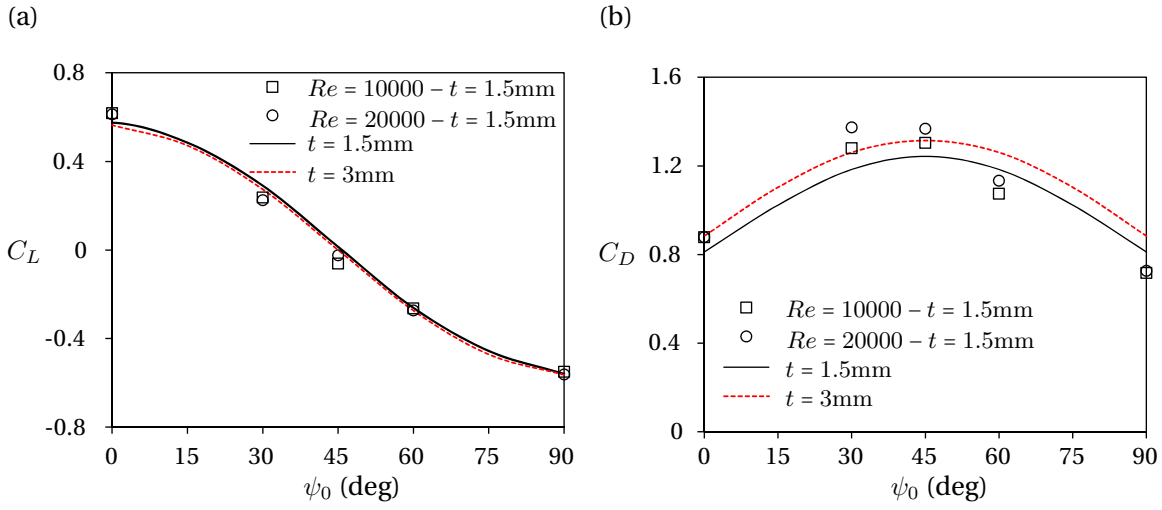

Figure 5.4 Variation of a) the lift and b) the drag coefficients for a rigid chiral ribbon with τ_0 = 90° as a function of the incidence angle ψ_0. The length and width of the ribbon are 400 mm and 25.4 mm respectively. Lines represent the mathematical model for two different thicknesses. Symbols represent the experimental results for two different Reynolds numbers.

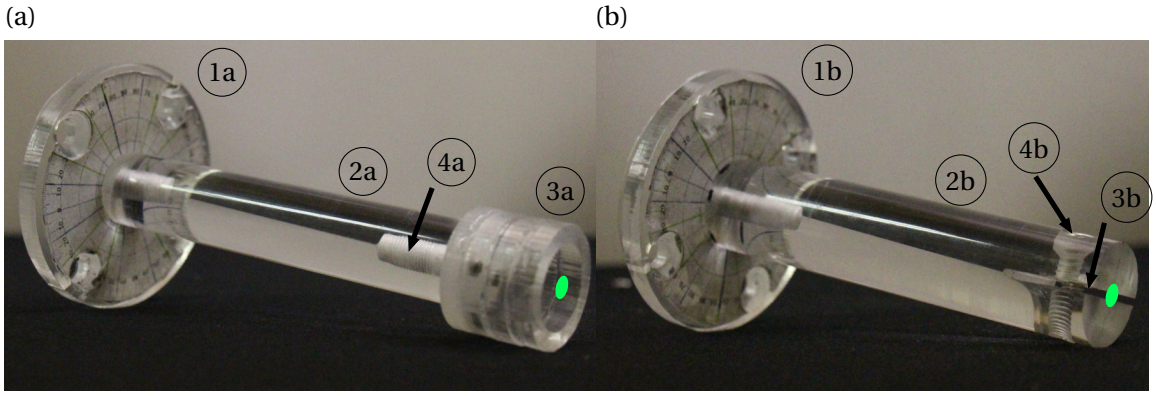

Figure 5.5 a) Photograph of the mast used for testing circular rods. It consists of a circular adapter for connection to the force transducer (1a), an acrylic rod (2a), a sleeve (3a) and a threaded hole to hold the M4 screw of circular rods (4a). b) Photograph of the mast used for testing ABS ribbons. It consists of a circular adapter for connection to the force transducer (1b), an acrylic rod (2b), a slot (3b) and a threaded hole to keep ribbons in place (4b). Small ellipses at the end of masts represent the reference point schematically.

standard deviation of fluctuating forces and moments were considered in the present study. For instance, the experimental points in Fig. 3.7 were the average of time fluctuating drag for a specific incidence angle and flow velocity. Similarly, each error bar in this figure represents the standard deviation of the time fluctuating drag for a single test including a specific incidence angle and a specific flow velocity. Images and videos were also captured during the tests using a DSLR camera. To capture the out-of-plane deformation of rods used in Fig. 3.5 and Fig. 3.6, the camera was fixed inside the wind tunnel at a distance of 1.5 m upstream from the test specimen. No aerodynamic loads were measured when the camera was inside the wind tunnel.

A special case for the reconfiguration of reinforced rods in the present study was at $\psi_0 = 90°$ with the occurrence of a pitch-fork bifurcation. In this angle of incidence, a rod underwent a two-dimensional bending in its rigid direction. Prior to the bifurcation point, the symmetric bending of the rod was stable but beyond that point, the rod lost its stability and jumped to a stable branch showing a sudden out-of-plane deformation. This phenomenon was very sensitive to imperfections in the rod structure, its clamped condition, and the accuracy of the imposed incidence angle. Due to the presence of several imperfections especially in the clamped boundary condition, the bifurcation happened earlier than the mathematical model prediction.

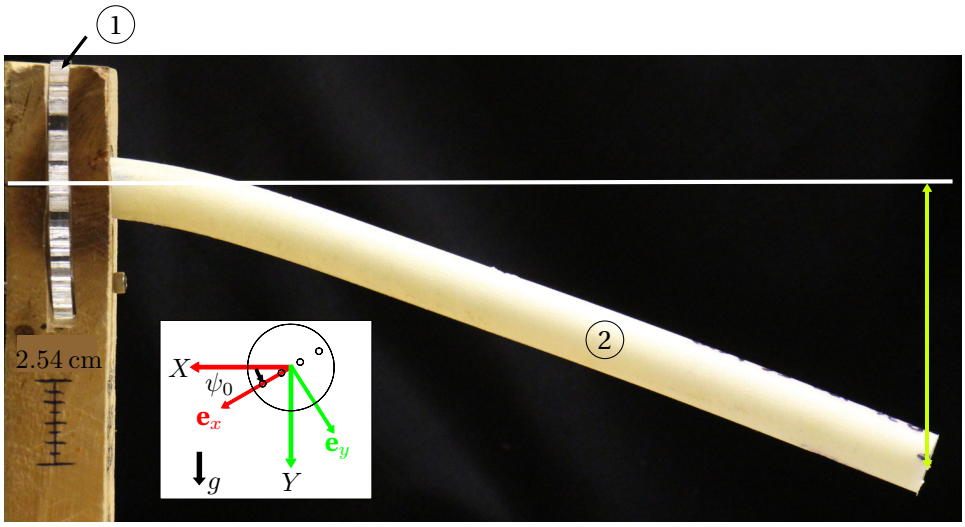

Figure 5.6 Test setup for the static bending test showing a cantilever rod (2) deforming under its own weight. The rod is attached to a disk (1) which can be rotated around its center to impose different incidence angles. The definition of the incidence angle is shown at the lower left of the figure.

5.5 Static Bending Test

A static bending test was conducted in this study to validate the mathematical model. The test setup is shown Fig. 5.6. As seen, a rod (2) is clamped from one end horizontally and deforms under its own weight. The clamped end of the rod is attached to a disk (1) which can be rotated around its center to impose an incidence angle on the rod. The definition of the incidence angle in this test is shown in the lower left of the figure. In the test, the gravitational force was in the Y-direction. For each test, the vertical deflection of the rod tip was measured from a horizontal line (as shown in the figure) for a range of incidence angles from 0° to 180°. Figure 4.2a shows the variation of the measured tip vertical deflection as a function of the incidence angle.

5.6 Details of Measurements on Cattail Leaves

In the study of chiral plants, cattail leaf (Typha angustifoli) were collected from the Voyageur Provincial Park (ON, Canada) in August, 2016 (Fig. 5.7). Twelve mature leaves were cut from their lowest point outside the water. The leaves were cut to segments of 12 cm to 20 cm for the three-point bending test one day after being collected. In the test, the distance between the supports was 10 cm and the downward velocity of the middle point was 1 cms^{-1}. Leaves were kept in the room temperature after collection as well as during the three-point bending

Figure 5.7 Photograph of cattail leaves at the the Voyageur Provincial Park in Ontario, Canada.

test. The minimum bending rigidity $(EI)_y$ of leaf segments was measured in the three-point bending test. This value was mainly used to estimate the dimensionless weight $\mathcal{W}$. However, the bending rigidity ratio λ and the twist-to-bend ratio η were evaluated based on an average rectangular section for the cattail leaves. Based on the mathematical model, it was found that the reconfiguration of cattail leaves is not significantly sensitive to the variation of $(EI)_y$ despite a two order of magnitude of change in the measured values.

CHAPTER 6 GENERAL DISCUSSION

In the literature, a bending beam is a common academic representation of plants. However, plants generally undergo a combination of bending and torsion under external loading. In this study, plants were modeled as a circular rod due to the simplicity of their aerodynamics. However, circular rods are completely symmetric and do not twist under drag loading. As a result, the circular rods used in this study were reinforced with nylon fibers to impose directional rigidity. This innovative approach helped to induce a controlled torsional deformation. In the wind tunnel tests and the mathematical modeling, the rods were rotated around their fixed end to alter their bending-torsion coupling.

Researchers usually use the Elastica model to study the reconfiguration of plants such as the work done by Alben *et al.* (2002) on bending fibers. However, a more general model is required to study the anisotropic circular rods. Thus, in this study the Kirchhoff rod model was used coupled with the Taylor semi-empirical drag formulation. This drag formulation is simple and accurate enough for the purpose of this study and has been proved to be effective in previous studies (Gosselin *et al.*, 2010; Luhar and Nepf, 2011). The mathematical model along with the wind tunnel tests showed that the torsional deformation in the reconfiguration of plants reduces their drag by letting them to bend in their less rigid direction. However, in large deformations, torsion has a small effect because the reconfiguration becomes nearly two-dimensional. Consequently, it was found that the Vogel exponent of anisotropic circular rods is similar to that of bending beams which is $-2/3$ (Gosselin *et al.*, 2010) if the equivalent Cauchy number is used.

Another significant aspect of this research was studying the effect of chirality on the reconfiguration of plants such as cattail. Few studies were found on this subject such as a study on aquatic emergent macrophytes (Zhao *et al.*, 2015). However, fundamental understanding of the large reconfiguration of chiral plants using an accurate structural and aerodynamic model was missing from the literature. In this research, chiral ribbons made of ABS plastic and circular rods with an internal chiral reinforcement were modeled and tested in a wind tunnel for a variety of flow conditions and structural properties. In contrast to the circular rods, chiral ribbons generate a lift force in addition to the drag force. Therefore, the existing mathematical model was modified to account for the chirality and lift. The mathematical model showed that chirality increases the self-buckling strength in plants which was also in agreement with another study on chiral upright plants (Schulgasser and Witztum, 2004). If was found from the mathematical model that chirality makes the deformation of rods inde-

pendent of the loading direction which was also supported by a simple static bending test and the wind tunnel tests. Moreover, the mathematical model was used to simulate the effect of chirality on several real plants such as daffodil (Etnier and Vogel, 2000), eelgrass (Abdelrhman, 2007; Luhar and Nepf, 2011) and cattail. It was found that chirality has different effects on plants with circular and non-circular sections. For circular plants, chirality reduced the bending moment at the root. However, for ribbon-like plants such as cattail, the root bending moment was found very high for intermediate chirality angles. In addition, there was a compromise between a high self-buckling strength and a high root bending moment. The measurements on chiral cattail leaves showed that the distribution of their chirality bypasses the intermediate chiral angles and is found around a large angle.

CHAPTER 7 CONCLUSION

The present study provided a fundamental understanding of the underlying mechanisms of plants reconfiguration which undergo three-dimensional deformation in flow. This multidisciplinary problem is intrinsically a fluid-structure interaction case initiated from a problem in the field of biology and forestry. The existing state of knowledge in this field was improved by using a better model to evaluate the reconfiguration of plants.

7.1 Contribution

In the literature, plants have been modeled as bending beams and plates neglecting their torsional deformation. However, many species of plants possess an asymmetric body, a chiral morphology or an internal fibrous structure which induces a bending-torsion coupling. These plants can twist more easily than bend under the flow (Vogel, 1992). In this study, the effect of torsional deformation and chirality on reconfiguration was investigated. Plants were modeled as slender rods which bend and twist under loading, giving a more accurate image of their reconfiguration. An innovative experimental and mathematical approach was introduced using elastic circular rods made of foam and reinforced with fibers. The reinforcement created a directional rigidity which induced a torsional deformation in asymmetric bending. This directional rigidity was quantified by the bending rigidity ratio. Along with this, the orientation of the reinforcement fibers at root or the incidence angle, was another key parameter to alter the bending-torsion coupling. In this study, circular rods were used due to their simple aerodynamic model. In addition to the circular rods, elastic ribbons made of ABS plastic with a twisting chirality were tested and modeled to mimic chiral plants. The similarity of elastic ribbons to slender wings, has opened an opportunity to analyze large deformations of lifting surfaces.

The mathematical model was based on the Kirchhoff theory of rods coupled with a semi-empirical drag formulation and the blade element theory. Using this model, it was possible to study an extended range of flow and structural parameters in the three-dimensional reconfiguration of rods. In the model, the evaluation of the aerodynamic loading was simple and accurate enough which largely reduced the computational time. For flexible ribbons, the blade element theory was applied to account for the variation of the sectional drag and lift coefficients where torsional deformation happens. This methodology proved to be in agreement with experiments regardless of its simplicity. The same approach can be applied for modeling flexible wings and turbine blades, as they are intrinsically similar to a ribbon bending and

twisting in flow. The model provides a generic mathematical framework that can be used for practical engineering problems with a minimum number of inputs. It is also capable of analyzing the large deformation of rods under external loads and torques other than the fluid loads.

The reconfiguration of chiral rods and ribbons subjected to flow and gravity was studied. Chirality was introduced into the model as an intrinsic twist angle. Based on the mathematical and experimental model, it was found that the deformation of chiral structures is less sensitive to the loading direction. In nature, this could be beneficial for upright plants to cope with harsh winds coming from an arbitrary direction. Moreover, chirality is possibly advantageous for the light interception of plants through the day since the sunlight direction changes from sunrise to sunset. Self-buckling is a limiting factor for the growth of upright plants. It was shown that chirality increases the self-buckling strength of upright plants which reduces the risk of structural failure. This is possibly the reason why chiral plants, such as emergent aquatic macrophytes (Zhao *et al.*, 2015), are very long with respect to their small cross section. The mathematical model showed that chirality can prevent uprooting of rods with a circular or semi-circular section by decreasing the root bending moment. On the contrary, it was found that chiral ribbons have a larger root bending moment compared with straight ribbons, specially around $\tau_0 = 150°$. Despite that, chirality provides benefits for plants including higher buckling strength and weaker dependency on the loading direction. Measurements were performed on a cattail species which showed that on average, their chiral angle is approximately two times greater than $\tau_0 = 150°$, meaning that they bypass the large root bending moment. Measurements on a different cattail species showed that their average chiral angle is 670° (Zhao *et al.*, 2015).

In the studies on the reconfiguration of plants, researchers usually use the Cauchy number or its equivalents to characterize the problem. In this study, a modified definition of the Cauchy number was provided based on the incidence angle and the directional rigidity, termed the *equivalent Cauchy number*. This dimensionless number let us include the effect of torsion in reconfiguration. Using this number and the reconfiguration number, it was possible characterize the three-dimensional reconfiguration of rods as a simple bending beam. It was shown that all experimental drag measurements of anisotropic rods, regardless of their material and structural properties collapse on a single curve representing a two-dimensional reconfiguration. Consequently, the Vogel exponent of the three-dimensional reconfiguration in the asymptotic regime of large deformations, was found to be similar to that of a bending beam $\vartheta = 0.67$. Therefore, it was shown that torsion does not alter the Vogel exponent. The reason is that in large deformations, rods twist in such a way to bend in their less rigid direction. As a result, a three-dimensional deformation becomes essentially two-dimensional

in the asymptotic regime.

7.2 Limitations and Future Work

To support our theoretical study on chirality, measurements were performed on a cattail species. These measurements included the length, sectional area, chirality and the bending rigidity. It was shown that this chiral plant bypasses small chirality angles which according to the mathematical model, leads to a high buckling strength and low root bending moment. However, it is necessary to obtain more experimental data for different chiral plants to verify the effect of chirality on their buckling strength and root bending moment. There are not many studies covering the chirality in plants therefore few experimental results are available in the literature. It seems that the chirality of plants has not been detailed enough as an important and distinctive characteristic. Therefore, it is of great interest to identify more chiral species and measure their structural and material properties. Moreover, in the mathematical model, the sectional area and the rigidity of rods and ribbons are assumed constant along the length. However, the cross section of plants usually become smaller from root to tip which alters their sectional rigidity. As a result, it is recommended to modify the existing mathematical model to account for the variation of the sectional area and rigidity along the length. This could lead to a more accurate model especially for the buckling strength of upright plants. Furthermore, it is interesting to verify the possibility of applying the existing mathematical model to other types of chiral structures, such as DNA, chiral polymers and nano-materials.

The deformation of slender ribbons was evaluated by coupling the blade element theory to the existing model. This method proved to be effective for slender ribbons with a large sectional aspect ratio. It is of great interest to apply this model to slender wings, rotors and turbine blades undergoing a large three-dimensional deformation. To do this, it is necessary to measure the variation of the sectional lift, drag and pitching moment coefficients with the incidence angle and introduce it to the model. In this case, the model can provide an accurate simulation for the primary stages of design and optimization since it requires a very small computation power compared with a conventional FSI analysis. This approach can be used to design and analyze the large deflection of modern wind turbine blades with a bending-torsion coupling (Larsen *et al.*, 2004). Similarly, the simulation of very flexible helicopter rotors used in MAVs (Sicard and Sirohi, 2012) and Formula 1 rear wings (Thuwis *et al.*, 2009) is within the range of the existing model. From the experimental perspective, it is recommended to fabricate very flexible slender wings using foam reinforced with fibers. If the reinforcement fibers are not located on the shear center of the wing section, a bending deformation can

induce a torsional deformation. Therefore, it is possible to design a wing which reduces its angle of attack and consequently its drag passively. The existing mathematical model is capable of simulating this type of wing.

The existing mathematical model simulates the static reconfiguration of rods and ribbons subjected to wind and gravity. Therefore, the outcome of the model represents the equilibrium state. As a future work, it is strongly recommended to perform a linear stability analysis on the dynamic Kirchhoff rod model. This is done by introducing a small time-dependent perturbation to the equilibrium solution and solve the governing equations using an optimization approach or a finite difference scheme. This can largely extend the application of the existing model to study the static and dynamic stability of slender structures at the same time. For instance, the dynamic model will be capable of simulating the divergence and the flutter instability of aeroelastically tailored wings and turbine blades undergoing a large three-dimensional deformation.

REFERENCES

Abdelrhman, Mohamed A. (2007). Modeling coupling between eelgrass Zostera marina and water flow. *Marine Ecology Progress Series*, *338*, 81–96.

Alben, Silas and Shelley, Michael and Zhang, Jun (2002). Drag reduction through self-similar bending of a flexible body. *Nature*, *420*(6915), 479–481.

Alben, Silas and Shelley, Michael and Zhang, Jun (2004). How flexibility induces streamlining in a two-dimensional flow. *Physics of Fluids*, *16*(5), 1694.

Ang, MH and Tourassis, Vassilios D (1987). Singularities of euler and roll-pitch-yaw representations. *Aerospace and Electronic Systems, IEEE Transactions on*, (3), 317–324.

Arbona, Jean Michel and Aimé, Jean-Pierre and Elezgaray, Juan (2012). Modeling the mechanical properties of DNA nanostructures. *Physical Review E*, *86*(5).

Audoly, Basile and Pomeau, Yves (2010). *Elasticity and geometry : from hair curls to the non-linear response of shells*. Oxford University Press Oxford.

Baker, CJ and Berry, PM and Spink, JH and Sylvester-Bradley, R and Griffin, JM and Scott, RK and Clare, RW (1998). A method for the assessment of the risk of wheat lodging. *J Theor Biol*, *194*(4), 587–603.

Berry, PM and Sterling, M and Mooney, SJ (2006). Development of a model of lodging for barley. *Journal of Agronomy and Crop Science*, *192*(2), 151–158.

Berry, P. M. and Sterling, M. and Baker, C. J. and Spink, J. and Sparkes, D. L. (2003). A calibrated model of wheat lodging compared with field measurements. *Agricultural and Forest Meteorology*, *119*(3-4), 167–180.

Berry, P. M. and Sterling, M. and Spink, J. H. and Baker, C. J. and Sylvester-Bradley, R. and Mooney, S. J. and Tams, A. R. and Ennos, A. R. (2004). Understanding and reducing lodging in cereals. *Advances in Agronomy*, *84*, 217–271.

Brulé, Veronique and Rafsanjani, Ahmad and Pasini, Damiano and Western, Tamara L (2016). Hierarchies of plant stiffness. *Plant Science*, *250*, 79–96.

Brüchert, Franka and Speck, Olga and Spatz, Hanns–Christof (2003). Oscillations of plants' stems and their damping : theory and experimentation. *Philosophical Transactions of the Royal Society of London. Series B : Biological Sciences*, *358*(1437), 1487–1492.

Buckingham, E. (1914). On physically similar systems ; illustrations of the use of dimensional equations. *Phys. Rev.*, *4*, 345–376.

Burgess, SC and Pasini, D (2004). Analysis of the structural efficiency of trees. *Journal of Engineering Design*, *15*(2), 177–193.

Chakrabarti, Subrata Kumar (2002). *The theory and practice of hydrodynamics and vibration*, vol. 20. World scientific.

Chen, W.R. and Hsin, S.W. and Chu, T.H. (2013). Vibration Analysis of Twisted Timoshenko Beams with Internal Kelvin-Voigt Damping. *Procedia Engineering*, *67*, 525–532.

Chen, Xiuqin and Yang, Shaoming and Motojima, Seiji and Ichihara, Masaki (2005). Morphology and microstructure of twisting nano-ribbons prepared using sputter-coated Fe-base alloy catalysts on glass substrates. *Materials Letters*, *59*(7), 854–858.

Cucuel, Bastien (2016). *Mise en évidence des paramètres influant sur les forces fluides et établissement de modèles empiriques de la trainée d'objets à géométrie variable.* Master's thesis, École Polytechnique de Montréal.

Curran, H. and Platts, J. (2006). Updating and optimization of a coning rotor concept.

da Fonseca, Alexandre F. and Galvão, Douglas S. (2004). Mechanical Properties of Nanosprings. *Physical Review Letters*, *92*(17).

De Goeij, WC and Van Tooren, MJL and Beukers, Adriaan (1999). Implementation of bending-torsion coupling in the design of a wind-turbine rotor-blade. *Applied Energy*, *63*(3), 191–207.

de Langre, Emmanuel (2008). Effects of wind on plants. *Annual Review of Fluid Mechanics*, *40*(1), 141–168.

de Langre, Emmanuel and Gutierrez, Alvaro and Cossé, Julia (2012). On the scaling of drag reduction by reconfiguration in plants. *Comptes Rendus Mécanique*, *340*(1-2), 35–40.

Dill, Ellis Harold (1992). Kirchhoff's theory of rods. *Archive for History of Exact Sciences*, *44*(1), 1–23.

Doedel, Eusebius and Kernevez, Jean Pierre (1986). *AUTO, software for continuation and bifurcation problems in ordinary differential equations.* California Institute of Technology.

Eloy, Christophe (2011). Leonardo's rule, self-similarity, and wind-induced stresses in trees. *Physical review letters*, *107*(25), 258101.

Ennos, AR (1993). The mechanics of the flower stem of the sedge carex acutiformis. *Annals of Botany*, *72*(2), 123–127.

Ennos, AR and Spatz, H-Ch and Speck, T (2000). The functional morphology of the petioles of the banana, musa textilis. *Journal of Experimental Botany*, *51*(353), 2085–2093.

Etnier, S.A. (2003). Twisting and bending of biological beams : distribution of biological beams in a stiffness mechanospace. *The Biological Bulletin*, *205*(1), 36–46.

Etnier, S.A. and Vogel, S. (2000). Reorientation of daffodil (narcissus : Amaryllidaceae) flowers inwind : drag reduction andtorsional flexibility. *American Journal of Botany*, *87*(1), 29–32.

Faisal, Tanvir R and Hristozov, Nicolay and Western, Tamara L and Rey, Alejandro and Pasini, Damiano (2016). The twist-to-bend compliance of the rheum rhabarbarum petiole : integrated computations and experiments. *Computer Methods in Biomechanics and Biomedical Engineering*, 1–12.

Gardiner, Barry and Peltola, Heli and Kellomäki, Seppo (2000). Comparison of two models for predicting the critical wind speeds required to damage coniferous trees. *Ecological modelling*, *129*(1), 1–23.

Gaylord, Brian and Blanchette, Carol A and Denny, Mark W (1994). Mechanical consequences of size in wave-swept algae. *Ecological Monographs*, 287–313.

Geoff, G. (2009). 2009 expedition archives. *Students on Ice*, *1*.

Glass, Samuel V. and Zelinka, Samuel L. (1999). *Wood Handbook,*, Forest Products Laboratory, chapitre Moisture Relations and Physical Properties of Wood.

Goriely, Alain and Shipman, Patrick (2000). Dynamics of helical strips. *Physical Review E*, *61*(4), 4508.

Goriely, Alain and Tabor, Michael (1998). Spontaneous helix hand reversal and tendril perversion in climbing plants. *Physical Review Letters*, *80*(7), 1564.

Gosselin, Frédérick P. and de Langre, Emmanuel (2011). Drag reduction by reconfiguration of a poroelastic system. *Journal of Fluids and Structures*, *27*(7), 1111–1123.

Gosselin, Frederick P. and de Langre, Emmanuel and Machado-Almeida, Bruno A. (2010). Drag reduction of flexible plates by reconfiguration. *Journal of Fluid Mechanics*, *650*, 319.

Hamilton, William Rowan (1853). *Lectures on quaternions*.

Hassani, Masoud and Mureithi, Njuki W and Gosselin, Frédérick P (2016). Large coupled bending and torsional deformation of an elastic rod subjected to fluid flow. *Journal of Fluids and Structures*, *62*, 367–383.

Huang, Wei-Xi and Shin, Soo Jai and Sung, Hyung Jin (2007). Simulation of flexible filaments in a uniform flow by the immersed boundary method. *Journal of Computational Physics*, *226*(2), 2206–2228.

Ifju, Peter G and Jenkins, David A and Ettinger, Scott and Lian, Yongsheng and Shyy, Wei and Waszak, Martin R (2002). Flexible-wing-based micro air vehicles. *AIAA paper*, *705*(2001-3290), 1–11.

Inayat-Hussain, JI and Kanki, H and Mureithi, NW (2003). On the bifurcations of a rigid rotor response in squeeze-film dampers. *Journal of fluids and structures*, *17*(3), 433–459.

Jamieson, Peter (2011). *Innovation in wind turbine design*. Wiley.

Ji, Xiang-Ying and Zhao, Meng-Qiang and Wei, Fei and Feng, Xi-Qiao (2012). Spontaneous formation of double helical structure due to interfacial adhesion. *Applied Physics Letters*, *100*(26).

Johnson, A and Koehl, M (1994). Maintenance of dynamic strain similarity and environmental stress factor in different flow habitats : thallus allometry and material properties of a giant kelp. *Journal of Experimental Biology*, *195*(1), 381–410.

Koehl, MAR (1977). Effects of sea anemones on the flow forces they encounter. *J Exp Biol*, *69*(1), 87–105.

Koehl, M. A.R. and Alberte, RS (1988). Flow, flapping, and photosynthesis of nereocystis luetkeana : a functional comparison of undulate and flat blade morphologies. *Marine Biology*, *99*(3), 435–444.

Lago, Lucas I. and Ponta, Fernando L. and Otero, Alejandro D. (2013). Analysis of alternative adaptive geometrical configurations for the nrel-5 mw wind turbine blade. *Renewable Energy*, *59*, 13–22.

Larsen, Torben J and Hansen, Anders M and Buhl, Thomas (2004). Aeroelastic effects of large blade deflections for wind turbines. *Special topic conference : The science of making torque from wind*. 238–246.

Lazarus, A and Miller, JT and Reis, PM (2013). Continuation of equilibria and stability of slender elastic rods using an asymptotic numerical method. *Journal of the Mechanics and Physics of Solids*, *61*(8), 1712–1736.

Lighthill, MJ (1960). Note on the swimming of slender fish. *J. Fluid Mech*, *9*(2), 305–317.

Liu, Zhanke and Young, Yin L. (2009). Utilization of bend–twist coupling for performance enhancement of composite marine propellers. *Journal of Fluids and Structures*, *25*(6), 1102–1116.

Lopez, Diego and Eloy, Christophe and Michelin, Sébastien and de Langre, Emmanuel (2013). Drag reduction, from bending to pruning. *arXiv preprint arXiv :1305.4995*.

Lopez, D. and Michelin, S. and de Langre, E. (2011). Flow-induced pruning of branched systems and brittle reconfiguration. *Journal of Theoretical Biology*, *284*(1), 117–24.

Love, A. E. H. (1944). *A Treatise on the Mathematical Theory of Elasticity*. Dover Publications, New York, quatrième édition.

Luhar, M. and Nepf, H.M. (2016). Wave-induced dynamics of flexible blades. *Journal of Fluids and Structures*, *61*, 20–41.

Luhar, Mitul and Nepf, Heidi M. (2011). Flow-induced reconfiguration of buoyant and flexible aquatic vegetation. *Limnology and Oceanography*, *56*(6), 2003–2017.

Lunine, J. I. and Beauchamp, J. and Smith, M. A. and Nikolaev, E. (1999). The Abiotic Generation of Homochirality on Saturn's Moon Titan. *Advances in BioChirality*, vol. 257.

Mattheck, C. (2006). Teacher tree : The evolution of notch shape optimization from complex to simple. *Engineering Fracture Mechanics*, *73*(12), 1732–1742.

Mattheck, C and Bethge, K (1998). The structural optimization of trees. *Naturwissenschaften*, *85*(1), 1–10.

Mattheck, C and Bethge, K and Kappel, R and MüLLER, P and Tesari, I (2003). Failure modes for trees and related criteria. *Wind Effects on Trees*. 219–230.

Moe, H. and Fredheim, A. and Hopperstad, O. S. (2010). Structural analysis of aquaculture net cages in current. *Journal of Fluids and Structures*, *26*(3), 503–516.

Niklas, Karl J (1996). Differences between acer saccharum leaves from open and wind-protected sites. *Annals of Botany*, *78*(1), 61–66.

Niklas, Karl J (1998). The influence of gravity and wind on land plant evolution. *Review of Palaeobotany and Palynology*, *102*(1), 1–14.

Pasini, D. and Mirjalili, V. (2006). The optimized shape of a leaf petiole. *Third International Conference on Design and Nature*. 35–45.

Peltola, H and Kellomäki, S and Väisänen, H and Ikonen, V-P (1999). A mechanistic model for assessing the risk of wind and snow damage to single trees and stands of scots pine, norway spruce, and birch. *Canadian Journal of Forest Research*, *29*(6), 647–661.

Rodriguez, M. and Ploquin, S. and Moulia, B. and de Langre, E. (2012). The multimodal dynamics of a walnut tree : Experiments and models. *Journal of Applied Mechanics*, *79*(4), 044505.

Rowlatt, Ursula and Morshead, Henry (1992). Architecture of the leaf of the greater reed mace, typha latifolia l. *Botanical journal of the Linnean Society*, *110*(2), 161–170.

Rudnicki, Mark and Mitchell, Stephen J. and Novak, Michael D. (2004). Wind tunnel measurements of crown streamlining and drag relationships for three conifer species. *Canadian Journal of Forest Research*, *34*(3), 666–676.

Saunderson, SET and England, AH and Baker, CJ (1999). A dynamic model of the behaviour of sitka spruce in high winds. *J Theor Biol*, *200*(3), 249–259.

Schouveiler, Lionel and Boudaoud, Arezki (2006). The rolling up of sheets in a steady flow. *Journal of Fluid Mechanics*, *563*, 71.

Schouveiler, Lionel and Eloy, Christophe and Le Gal, Patrice (2005). Flow-induced vibrations of high mass ratio flexible filaments freely hanging in a flow. *Physics of Fluids*, *17*(4), 047104.

Schulgasser, Kalman and Witztum, Allan (2004). Spiralling upward. *Journal of theoretical biology*, *230*(2), 275–280.

Shao, Chuan-Ping and Chen, Ye-Jun and Lin, Jian-Zhong (2012). Wind induced deformation and vibration of a platanus acerifolia leaf. *Acta Mechanica Sinica*, *28*(3), 583–594.

Shim, Jae-Eul and Quan, Ying-Jun and Wang, Wei and Rodrigue, Hugo and Song, Sung-Hyuk and Ahn, Sung-Hoon (2015). A smart soft actuator using a single shape memory alloy for twisting actuation. *Smart Materials and Structures*, *24*(12), 125033.

Shirk, Michael H and Hertz, Terrence J and Weisshaar, Terrence A (1986). Aeroelastic tailoring-theory, practice, and promise. *Journal of Aircraft*, *23*(1), 6–18.

Sicard, Jérôme and Sirohi, Jayant (2012). Experimental study of an extremely flexible rotor for microhelicopters. *Journal of Aircraft*, *49*(5), 1306–1314.

Sicard, Jérôme and Sirohi, Jayant (2014). Modeling of the large torsional deformation of an extremely flexible rotor in hover. *AIAA Journal*, *52*(8), 1604–1615.

Sicard, Jerome and Sirohi, Jayant (2016). Aeroelastic stability of a flexible ribbon rotor blade. *Journal of Fluids and Structures*, *67*, 106–123.

Skatter, Sondre and Kučera, B (1997). Spiral grain—an adaptation of trees to withstand stem breakage caused by wind-induced torsion. *Holz als Roh-und Werkstoff*, *55*(2-4), 207–213.

Sobey, Ian John (2000). *Introduction to interactive boundary layer theory*, vol. 3. Oxford University Press.

Spatz, H and Speck, Th and Vogellehner, D and others (1990). Contributions to the Biomechanics of Plants. ; II. Stability Against Local Buckling in Hollow Plant Stems. *Botanica Acta*, *103*(1), 123–130.

Spatz, Hanns-Christof and Brüchert, Franka and Pfisterer, Jochen (2007). Multiple resonance damping or how do trees escape dangerously large oscillations ? *American Journal of Botany*, *94*(10), 1603–1611.

Speck, Olga (2003). Field measurements of wind speed and reconfiguration in arundo donax (poaceae) with estimates of drag forces. *American Journal of Botany*, *90*(8), 1253–1256.

Speck, Olga and Spatz, Hanns-Christof (2004). Damped oscillations of the giant reed arundo donax (poaceae). *American Journal of Botany*, *91*(6), 789–796.

Speck, TH and Spatz, H and Vogellehner, D and others (1990). Contributions to the biomechanics of plants. I. Stabilities of plant stems with strengthening elements of different cross-sections against weight and wind forces. *Botanica Acta*, *103*(1), 111–122.

Stanford, Bret and Ifju, Peter and Albertani, Roberto and Shyy, Wei (2008). Fixed membrane wings for micro air vehicles : Experimental characterization, numerical modeling, and tailoring. *Progress in Aerospace Sciences*, *44*(4), 258–294.

Sterling, M and Baker, CJ and Berry, PM and Wade, A (2003). An experimental investigation of the lodging of wheat. *Agricultural and Forest Meteorology*, *119*(3), 149–165.

Taylor, G. (1952). Analysis of the swimming of long and narrow animals. *Proceedings of the Royal Society A : Mathematical, Physical and Engineering Sciences*, *214*(1117), 158–183.

Telewski, Frank W and Jaffe, MJ (1981). Thigmomorphogenesis : changes in the morphology and chemical composition induced by mechanical perturbation in 6-month-old pinus taeda seedlings. *Canadian Journal of Forest Research*, *11*(2), 381–388.

Telewski, Frank W and Jaffe, Mordecai J (1986a). Thigmomorphogenesis : anatomical, morphological and mechanical analysis of genetically different sibs of pinus taeda in response to mechanical perturbation. *Physiologia Plantarum*, *66*(2), 219–226.

Telewski, Frank W and Jaffe, Mordecai J (1986b). Thigmomorphogenesis : the role of ethylene in the response of pinus taeda and abies fraseri to mechanical perturbation. *Physiologia Plantarum*, *66*(2), 227–233.

Thomison, P. (2011). Effects of wind lodging on corn performance. *Agronomic Crops Network*, *1*.

Thuwis, Glenn A. A. and Breuker, Roeland and Abdalla, Mostafa M. and Gürdal, Zafer (2009). Aeroelastic tailoring using lamination parameters. *Structural and Multidisciplinary Optimization*, *41*(4), 637–646.

Ulanova, Nina G (2000). The effects of windthrow on forests at different spatial scales : a review. *Forest Ecology and Management*, *135*(1), 155–167.

Verdier, Patrick (2003). Palmier sur une plage de martinique, antilles. *Free Online Photos*, *1*.

Vogel, Steven (1984). Drag and flexibility in sessile organisms. *American Zoologist*, *24*(1), 37–44.

Vogel, Steven (1989). Drag and reconfiguration of broad leaves in high winds. *Journal of Experimental Botany*, *40*(8), 8.

Vogel, Steven (1992). Twist-to-bend ratios and cross-sectional shapes of petioles and stems. *Journal of Experimental Botany*, *43*(11), 1527–1532.

Vogel, Steven (2007). Living in a physical world xi. to twist or bend when stressed. *Journal of Biosciences*, *32*(4), 643–655.

Vollsinger, Stephan and Mitchell, Stephen J. and Byrne, Kenneth E. and Novak, Michael D. and Rudnicki, Mark (2005). Wind tunnel measurements of crown streamlining and drag relationships for several hardwood species. *Canadian Journal of Forest Research*, *35*(5), 1238–1249.

Wang, Jian-Shan and Cui, Yu-Hong and Shimada, Takahiro and Wu, Hua-Ping and Kitamura, Takayuki (2014). Unusual winding of helices under tension. *Applied Physics Letters*, *105*(4), 043702.

Wang, J.-S. and Ye, H.-M. and Qin, Q.-H. and Xu, J. and Feng, X.-Q. (2012). Anisotropic surface effects on the formation of chiral morphologies of nanomaterials. *Proceedings of the Royal Society A : Mathematical, Physical and Engineering Sciences*, *468*(2139), 609–633.

Weisshaar, T and Nam, Changho and Batista-Rodriguez, Alicia (1998). Aeroelastic tailoring for improved UAV performance. *AIAA Structures, Structural Dynamics, and Materials Conference*. 20–23.

Ye, Hai-Mu and Wang, Jian-Shan and Tang, Shuo and Xu, Jun and Feng, Xi-Qiao and Guo, Bao-Hua and Xie, Xu-Ming and Zhou, Jian-Jun and Li, Lin and Wu, Qiong and Chen, Guo-Qiang (2010). Surface Stress Effects on the Bending Direction and Twisting Chirality of Lamellar Crystals of Chiral Polymer. *Macromolecules*, *43*(13), 5762–5770.

Zhang, Xin and Toet, Willem and Zerihan, Jonathan (2006). Ground effect aerodynamics of racing cars. *Applied Mechanics Review*, *59*(1), 33–49.

Zhao, Zi-Long and Zhao, Hong-Ping and Li, Bing-Wei and Nie, Ben-Dian and Feng, Xi-Qiao and Gao, Huajian (2015). Biomechanical tactics of chiral growth in emergent aquatic macrophytes. *Scientific Reports*, *5*, 12610.

Zhao, Zi-Long and Zhao, Hong-Ping and Wang, Jian-Shan and Zhang, Zhong and Feng, Xi-Qiao (2014). Mechanical properties of carbon nanotube ropes with hierarchical helical structures. *Journal of the Mechanics and Physics of Solids*, *71*, 64–83.

Zhu, Luoding and Peskin, Charles S. (2002). Simulation of a flapping flexible filament in a flowing soap film by the immersed boundary method. *Journal of Computational Physics*, *179*(2), 452–468.

Zhu, Z. H. and Meguid, S. A. (2007). Modeling and simulation of aerial refueling by finite element method. *International Journal of Solids and Structures*, *44*(24), 8057–8073.

APPENDIX A DIRECTION COSINES

The direction cosines are a representation of the material frame's rotation. They are the cosines of the angles between a vector and the three directions forming the fixed coordinate system. Since the material frame and the fixed frame have three directions each, nine direction cosines are needed to define the material frame. As detailed by Audoly and Pomeau (2010), the spatial derivative of $\mathbf{e}_i(s)$ with respect to s is defined by :

$$\mathbf{e'}_i(s) = \Omega(s) \times \mathbf{e}_i(s) \ , \tag{A.1}$$

where $i = x$, y and z. The parameter $\mathbf{\Omega}(s)$ is the rotation velocity or the *Darboux vector* defined by :

$$\mathbf{\Omega}(s) = \kappa_x(s)\mathbf{e}_x(s) + \kappa_y(s)\mathbf{e}_y(s) + \tau(s)\mathbf{e}_z(s) \ . \tag{A.2}$$

By introducing Eq. (A.2) in Eq. (A.1), spatial derivatives of the directions of the material frame are calculated as Eq. (3.6). Each direction of the material frame is defined by the vector contained in a row of the matrix $[c]$ (Eq. (3.6)), e.g. $\mathbf{e}_x = (c_{11}, c_{12}, c_{13})$. Therefore, by expanding Eq. (3.6), we have :

$$\frac{dc_{11}}{ds} = \tau c_{21} - \kappa_y c_{31} \qquad \frac{dc_{12}}{ds} = \tau c_{22} - \kappa_y c_{32} \qquad \frac{dc_{13}}{ds} = \tau c_{23} - \kappa_y c_{33} \ , \tag{A.3}$$

$$\frac{dc_{21}}{ds} = -\tau c_{11} + \kappa_x c_{31} \qquad \frac{dc_{22}}{ds} = -\tau c_{12} + \kappa_x c_{32} \qquad \frac{dc_{23}}{ds} = -\tau c_{13} + \kappa_x c_{33} \ , \tag{A.4}$$

$$\frac{dc_{31}}{ds} = \kappa_y c_{11} - \kappa_x c_{21} \qquad \frac{dc_{32}}{ds} = \kappa_y c_{12} - \kappa_x c_{22} \qquad \frac{dc_{33}}{ds} = \kappa_y c_{13} - \kappa_x c_{23} \ . \tag{A.5}$$